2014-04-24

Characterization and Compensation of Hysteretic Cardiac Respiratory Motion in Myocardial Perfusion Studies Through MRI Investigations

Paul Krupaker Reddy Dasari
Worcester Polytechnic Institute

Repository Citation
Dasari, P. K. (2014). *Characterization and Compensation of Hysteretic Cardiac Respiratory Motion in Myocardial Perfusion Studies Through MRI Investigations*. Retrieved from https://digitalcommons.wpi.edu/etd-dissertations/159

Characterization and Compensation of Hysteretic Cardiac Respiratory Motion in Myocardial Perfusion Studies through MRI Investigations

A dissertation submitted to the faculty of the
WORCESTER POLYTECHNIC INSTITUTE
in partial fulfillment of the requirements for the degree of
Doctor of Philosophy in Biomedical Engineering

By

Paul Krupaker Reddy Dasari

April 2014

Approved:

Michael King

Michael A. King, Ph.D., DABR
Professor And Vice-Chair For Research, Major Advisor
Department of Radiology
University of Massachusetts Medical School

Y. Mendelson

Yitzhak Mendelson, Ph.D.
Associate Professor
Department of Biomedical Engineering
Worcester Polytechnic Institute

Stephen C Moore

Stephen C. Moore, Ph. D.
Director and Associate Professor
Department of Radiology
Brigham and Women's Hospital/
Harvard Medical School

Stephen Glick

Stephen Glick, Ph.D.
Professor
Department of Radiology
University Of Massachusetts Medical
School

John Sullivan

John M. Sullivan, Jr, Ph. D.
Professor
Department of Mechanical Engineering
Worcester Polytechnic Institute

Abstract

Respiratory motion causes artifacts and blurring of cardiac structures in reconstructed images of SPECT and PET cardiac studies. Hysteresis in respiratory motion causes the organs to move in distinct paths during inspiration and expiration. Current respiratory motion correction methods use a signal generated by tracking the motion of the abdomen during respiration to bin list-mode data as a function of the magnitude of this respiratory signal. They thereby fail to account for hysteretic motion. The goal of this research was to demonstrate the effects of hysteretic respiratory motion and the importance of its correction for different medical imaging techniques particularly SPECT and PET. This study describes a novel approach for detecting and correcting hysteresis in clinical SPECT and PET studies. From the combined use of MRI and a synchronized Visual Tracking System (VTS) in volunteers we developed hysteretic modeling using the Bouc-Wen model with inputs from measurements of both chest and abdomen respiratory motion. With the MRI determined heart motion as the truth in the volunteer studies we determined the Bouc Wen model could match the behavior over a range of hysteretic cycles. The proposed approach was validated through phantom simulations and applied to clinical SPECT studies.

Table of Contents

List of Figures

List of Tables

Acknowledgements

King Solomon got it right when he noted, “Of making many books there is no end, and much study is a weariness of the flesh” (Ecclesiastes 12:12). And I would not have been able to successfully finish my dissertation without the guidance of my committee members, help from friends, and support from my family.

I would first like to thank my committee members for their time and their help on various aspects of this research project. Without whose participation, this research would not have been successful. They are:

- Dr. Michael King, my research advisor, who has given me the opportunity to grow and expand as a researcher within the field of Nuclear Medicine and MR, and for his continual support and guidance. Dr. King has served not only as a mentor, but also as a colleague and a friend.
- Dr. Yitzhak Mendelson, my academic advisor, is a great teacher and helped me tremendously on various aspects of this project and kept me motivated during my time here.
- Dr. Stephen Moore, who helped me in many aspects of the project especially with refining the methods in simulation studies and who painstakingly went over my work and made it much better.
- Dr. Stephen Glick, who helped me understand more of the computer optimization portion of this project through our conversations.
- Dr. John M. Sullivan, Jr, who helped me in many aspects of the project understand especially during the model development and its application.

I would also like to thank everyone else who contributed significantly to this project. They are:

- Dr. Arda Konik, for his help in many aspects of this project especially enabling me to understand the physics and image reconstruction associated with emission tomography. Dr. Konik helped in setting up simulation studies and also provided valuable inputs for data analysis.
- Dr. Hendrik Pretorious, for his help in understanding the aspects of emission tomography, the physiology of the heart and his help with the NCAT phantom stimulations and clinical studies.
- Dr. Shaokuan Zheng, for his help in MRI experiments.
- Karen Johnson, for her help in recruiting volunteers and patients and also her help in setting up Visual Tracking System and performing acquisitions.
- Dr. M. Salman Shazeeb for his valuable help in data analysis and inputs through his discussions during model development.
- Dr. Clifford Lindsay for his valuable inputs and discussion in optimization process and various other aspects of the project
- Dr. Joyoni Dey and Dr. Joyeeta Mitra, for their reconstruction algorithm and help in preliminary set up of experiments and data analysis.
- Dr. William Paul Segars for providing us with modified NCAT phantom for us to be able to simulate hysteretic patterns.
- Dr. Kai-Rong Qin and Dr. Cheng Xiang for their valuable assistance in modeling by sharing their optimization code.

I would like to thank Late Dr. Christopher Sotak, my former advisor and mentor, for giving me the opportunity to grow and expand as a researcher within the field of MRI. A great teacher and helped me tremendously on MR projects during my lab-rotations as well as many other things. He showed me how to write research articles as well as how to prepare a presentation. Dr. Sotak also explained many things for which I had very little or no knowledge.

I would like to thank President Dennis D. Berkey for making this dissertation successful by providing for tuition through the President's Fund.

I would like to thank Dr. Arda Konik, Dr. M. Salman Shazeeb, Dr. Kesava Kalluri, Dr. Clifford Lindsay, Dr. Andrey Makeev, Dr. Michael O'Connor, Dr. Ali Bourisly, Dr. Guoen Jin, Dr. Li, Dr. Chet Ford and Dr. Ronn Walvick for extending their valuable support and friendship during my time here.

I would like to thank my parents, my brother, my wife, my friends and extended family for their continued love and support.

Above all, I'm grateful to my God and my Heavenly Father for His ever-wise working in my life to bring about His best.

Thesis Overview

The presence of patient motion, respiration and myocardial contraction during myocardial perfusion imaging (MPI) with Emission Tomography (ET) systems -- i.e., Single Photon Emission Computed Tomography (SPECT) or Positron Emission Tomography (PET) can cause degradation in image quality, primarily due to blurring in the sub-diaphragmatic sites with significant uptake, worse resolution in the direction of the motion, and mismatches between the emission (nuclear medicine) and transmission computed tomography (CT) datasets. Each of these motion sources needs to be addressed independently based on its features. Successful compensation of motion would improve the diagnostic accuracy of these clinical studies to the extent motion is present in a given study.

The effects of patient motion, respiratory motion and cardiac motion on Myocardial Perfusion Imaging (MPI) studies are well documented and many methods for overcoming them have been previously investigated. However, in this work the primary focus has been on cardiac respiratory motion and its correction. Respiratory motion of the heart can result in up to 1–2 cm displacement of the heart during imaging and thereby impacting image clarity and potentially the diagnostic accuracy of cardiac perfusion images. An effective method of respiratory motion correction is to perform gating using a surrogate signal from the patient related to respiration. Gating splits emission data into motion-limited frames. These frames subsequently are realigned and combined to reduce blurring with no loss in the counts.

The use of external surrogates to infer internal heart motion assumes that there exists a consistent relationship between the external and internal motions. However the internal movements can take different paths relative to the surrogate signal during inspiration and expiration phases of the respiratory cycle, a phenomenon called hysteresis. The effects of respiratory hysteresis however have previously received less attention, due to the fact that the system spatial resolution of MPI scans and the magnitude of cardiac respiratory motion are of the same order. With the increasing use of higher resolution imaging modalities (PET and PET/CT) and the advancements in algorithms to compensate for system spatial resolution resulting in improved MPI-SPECT image resolution, it is hypothesized that the effect of respiratory related cardiac motion on MPI image quality is more pronounced. In addition, the image artifacts resulting from motion of larger than typical magnitude during respiration can have the appearance of a perfusion defect due to emission-transmission mismatch and/or excessive blurring in the direction of the motion.

Organization

This dissertation is broadly divided into three parts following the outline of each specific aim described in Chapter 1; the detection and characterization of respiratory motion patterns (aim 1), development of a method to correct for respiratory motion patterns (aim 2), and the implementation of the developed method to overcome the problems caused by respiratory motion through simulation and clinical studies (aims 3a and 3b).

Chapter 2 begins by providing background information on the imaging modalities used in this work and the physics behind them. It outlines the issues related to the problem of motion-correction in cardiac emission studies and the existing methods of correction. Chapter 2 concludes by introducing the Bouc-Wen model used in correcting hysteresis and the software phantom (the NCAT phantom) implemented in simulation studies

Chapter 3 focuses on investigating the behavior of respiratory motion of the heart and how it correlates with external surrogates on the subject’s thoracic and abdomen regions in the presence of hysteresis. A visual tracking system (VTS) synchronized with magnetic resonance imaging (MRI) navigator was used to track the motion of external surrogates and internal organs respectively. The motion information gathered from each of these sources was correlated to characterize the respiratory patterns. This section is based on a paper, “MRI Investigation of the Linkage Between

Respiratory Motion of the Heart and Markers on Patient's Abdomen and Chest: Implications for Respiratory Amplitude Binning List-Mode PET and SPECT Studies" published in IEEE Transactions on Nuclear Science, vol. 61, pp. 192-201, 2014

Chapter 4 discusses the development and testing of the proposed method using the Bouc-Wen model to address the issue of respiratory hysteresis. The model accounts for hysteresis by exploiting the amount of variation in the respiratory motions between the external surrogates placed on the thoracic and abdomen regions to estimate the internal heart motion. The motion information obtained from subjects in the previous stage (chapter 3) was divided into training and testing data sets to optimize and evaluate the performance of the proposed model in accounting for various types of respiratory patterns.

Chapter 5 compares the performance of the proposed method and the current existing method in simulation and clinical studies. In the use of simulated SPECT studies based on the software phantom (the NCAT phantom), three different types of respiratory patterns (observed in Chapter 3) each with various extents of hysteresis were selected to simulate respiratory hysteresis and demonstrate the problem caused by its presence even after conventional respiratory motion correction. The utility of the proposed method in diminishing the errors caused by respiratory hysteresis is investigated individually on the polar maps of the NCAT phantoms with and without perfusion defects simulated in different regions of the left ventricular wall. By performing simulations on the three types of respiratory patterns, it was possible to ascertain which types of respiratory patterns generate artifacts that specifically impact cardiac studies.

The proposed and current methods were applied on MPI-SPECT acquisitions of ten patients to evaluate the effectiveness of one method over the other in detecting and correcting for hysteresis. Chapter 5 concludes with description of the visual and quantitative assessment of the slices and polar maps of patient studies with the proposed and the current methods.

Finally, Chapter 6 summarizes the results and findings of the previous chapters and discusses future work for the continued development and use of the proposed method.

Chapter 1 - Objectives

For the aforementioned effects of motion, the primary objectives of this thesis were to investigate the effects of respiratory hysteresis, and develop a technique of motion-correction that accounts for respiratory hysteresis and results in quantitatively accurate motion-compensated scans of the myocardium. For this to be achieved it was important to ascertain the means to detect hysteresis and then correct for it. To be practical the technique should be based on acquiring motion information only from external observations. A transformation should then be able to be applied to these observations using a suitable model to obtain an estimated signal that matches the heart motion. Using the estimated heart motion for gating the emission scans could thus mitigate the problems of residual blur and mismatches in the reconstructions.

The following specific aims were thus established for this investigation:

Aim 1: To develop a method of detecting hysteresis of the cardiac respiratory motion using external surrogates. This helps us understand the nature of hysteresis by evaluating internal and external motion, and to identify the signs of its manifestation.

Aim 2: To develop a method to account for cardiac respiratory hysteresis using the information obtained from the external surrogates. This aids in converting the external surrogate position directly to the internal heart motion by accounting for hysteresis.

Aim 3a: To investigate the ability of the developed method to account for respiratory hysteresis through realistic phantom simulations of respiratory hysteresis in

myocardial SPECT. By performing this investigation with phantom simulations based on measured external signals using a visual-tracking-system (VTS) and internal heart motions using MRI, the magnitude of the motion caused by hysteresis and the ability of the proposed correction strategy can be studied in a controlled situation where truth in terms of motion is known.

Aim 3b: To apply the developed method to clinical MPI SPECT images to evaluate the effect of its correction by comparing to the already existing respiratory motion correction methods and baseline images with no motion correction. This provides a comparison of clinical images corrected with the proposed and the current method both visually and quantitatively.

Chapter 2 - Background

This chapter provides a synopsis of the background areas dealt with in this dissertation. An introduction to the imaging modalities used in studying the behavior of the heart during respiration is given in sections 2.2 and 2.3. The fundamental aspect of this project is in dealing with the problems of respiratory motion in cardiac emission studies, which are discussed in section 2.4, and a general overview on respiratory gating and correction methods is given.

2.1 The heart

The primary function of the heart is to pump blood continually to various organs of the body, allowing the transportation of oxygen and nutrients. It consists of four chambers as shown in Figure 2.1; the right atrium receives the deoxygenated blood from various organs and channels it to right ventricle. The right ventricle pumps blood to the lungs for oxygenation. On the other hand, the left atrium receives the oxygenated blood from the lungs and passes the blood on to the left ventricle. The blood from the left ventricle pumps the blood to rest of the body through the vascular system.

The walls of the heart are comprised of three layers: the outer epicardium, the middle myocardium and the inner endocardium. The middle layer, myocardium, is made up of cardiac muscle which contracts. The myocardium of the left ventricle is thicker compared to the right ventricle, allowing it to contract with a greater force sufficient to pump the oxygenated blood to the distal parts of the body. This cycle of ventricles filling and emptying is estimated to be every second under normal conditions.

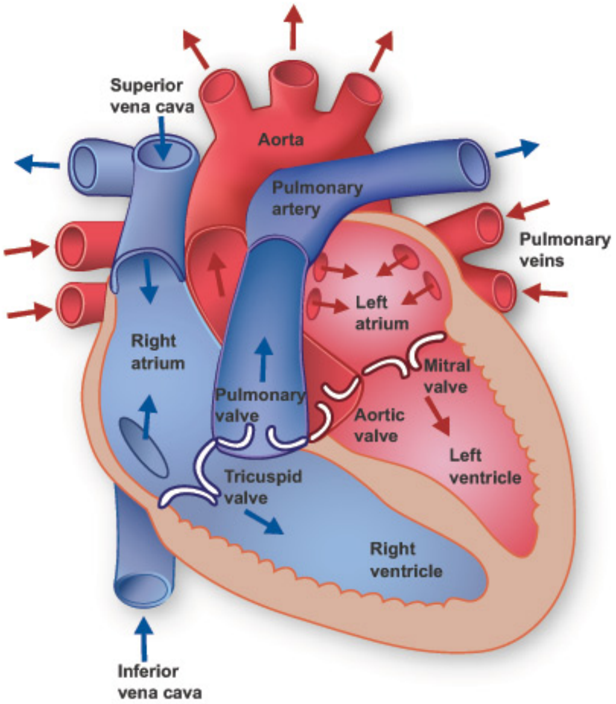

Figure 2.1 The anatomy of the heart. Figure from www.texasheart.org/HIC/Anatomy/anatomy2.cfm

A good supply of blood to the myocardium itself is necessary in order to sustain the cycle of contraction and relaxation. A decreased blood supply to the heart due to the constriction of the arteries supplying the myocardium indicates the presence of coronary artery disease (CAD). Under stress (exercise) conditions, the oxygen requirements of the myocardium are increased and the constricted arteries prevent the blood flow reaching the required level. Severe obstruction of the blood supply results in myocardial infarction (heart attack), which is irrevocable and can cause improper functioning of the left-ventricular myocardium [1].

CAD is one of the leading causes of death across the world especially in developed countries, for both sexes [2]. It is crucial in determining the most favorable course of treatment for a patient with CAD based on the presence of ischemia and viability of the myocardial muscle. In order to assess these factors, functional imaging methods such as myocardial perfusion imaging play a special role in yielding important diagnostic information regarding the functionality of the left ventricle.

2.2 Cardiac Imaging

Here, we review imaging considerations with regard to the two modalities considered in this work: SPECT and MRI.

2.2.1 Emission Tomography

Emission tomography is a type of medical imaging comprised of two main techniques: 1) Positron Emission Tomography (PET) and 2) Single Photon Emission Computed Tomography (SPECT). Emission tomography uses radioactive materials to image the physiological properties of the body such as glucose metabolism, blood flow, and receptor concentrations. Therefore, emission tomography is used to detect tumors, locate the perfusion deficit areas of the heart, and also identify various regions of the brain that are influenced by drugs, as well as image several other types of organ functions.

Emission tomography is comprised of two basic principles: 1) imaging by means of gamma-ray emission, called the tracer principle, and 2) volumetric imaging of the internal organs, called tomography.

2.2.2 The Tracer Principle

George de Hevesy developed the tracer principle in early 1900s. He demonstrated that radioactive materials engage in physiological processes as non-radioactive materials. Based on the fact that the radioactive materials can be detected by the way of their emission of gamma-rays, these materials can be used to track the flow of distribution of important materials in the body.

Present-day PET and SPECT use a radioactive material as a representative tracer of natural nonradioactive materials as imaging agents. Imaging agents, known as radiopharmaceuticals or radiotracers, can be designed to act as markers for a variety of physiological substances that engage in the body's natural processes thereby yielding useful diagnostic information.

2.2.3 Tomography

There are two means of visualizing the radiotracer distribution: 1) projection imaging and 2) tomography. Projection image is one in which the three-dimensional structure is projected on a planar surface and represented in two-dimensional format. A tomographic image is a cross-sectional slice. The emission data recorded by the imaging hardware are in the form of projections. The projection measurements are acquired from many angles about the body. Image reconstruction is performed on the projection data to observe tomographic images.

2.2.4 Single Photon Emission Computed Tomography (SPECT)

Although this study focuses on emission tomography, which involves both PET and SPECT, the emphasis has been mainly on myocardial perfusion imaging (MPI) using SPECT. SPECT studies employ radiopharmaceuticals marked with a single-photon emitter, a radioactive isotope that emits one gamma-ray photon for every radioactive decay event. A SPECT study begins with the administration of the radiotracer/radiopharmaceutical followed by the detection and recording of gamma-rays emitted by the radiopharmaceutical. The rate of gamma-ray emissions is relatively low (~10^4 counts/s/ml of a tissue of interest) due to the safety limitations on the amount of a radiopharmaceutical that can be administered to the patient.

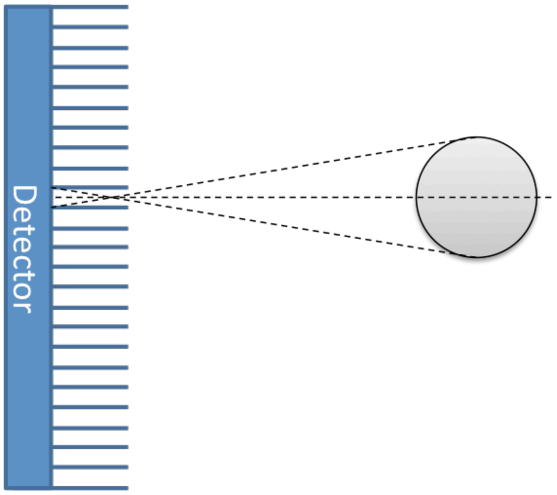

Figure 2.2 Pictorial view of collimation, illustrating parallel-hole collimator.

A thick sheet of a heavy metal (such as lead) perforated by long thin channels act as a collimator (Figure 2.2). The primary function of this collimator is to select the gamma rays that form an image of the activity distribution. On the opposite side of the collimator from the object is the detection hardware system. The gamma rays that traverse the collimator impact with a crystal material called a scintillator. The scintillator translates the high-energy gamma ray into many optical-wavelength photons. These photons are detected by a two-dimensional (2D) array of photomultiplier tubes (PMTs), which produces a cascade of electrons, yielding a measurable electric current. This current is sensed and registered as the occurrence of an event. The events are registered in a histogram based on their position. The resulting histogram at the end of the imaging period represents a projection image of the object. The projection images acquired repeatedly by imaging the patient from many angles are used for image reconstruction.

Different types of SPECT systems characterized by different camera configurations have emerged due to rapid advances in camera and computer performance. A clear benefit of adding more detectors to the SPECT system is the increase in sensitivity, and it is preferred for cardiac imaging. The different types of SPECT camera configurations are illustrated in Figure 2.3. More theoretical material on SPECT systems and a detailed survey of the use of multi-detector camera systems and processing techniques and its benefits can be found in [3, 4].

Four main factors, namely: attenuation, scatter, depth dependent blur and motion, influence the SPECT image reconstruction; thus, these factors must be accounted for in an accurate description of the SPECT image acquisition. Attenuation results from the loss of gamma rays either because of absorption within the object or scatter outside the field of view. The reconstructed images that do not account for attenuation appear dark in the interior of the object. Scattering deals with the interactions that take place between the gamma rays and the matter that constitutes the patient body, causing misleading information on the origin and the direction of the gamma-ray. This results in a nonlinear blurring effect of the image. Depth-dependent blur appears in the image as a blurring of the image: the blurring is more for portions of the object that are more distant from the collimator. Motion due to patient body movement or respiratory motion leads to nonlinear blurring or elongation of the objects in the reconstructed image.

In addition to the above-mentioned factors, all emission tomographic data are corrupted by noise, which is the primary factor that limits the quality obtainable. The noise in emission tomography images is called photon noise or Poisson noise, due to the Poisson probability distribution of the number of events recorded during any given interval of time.

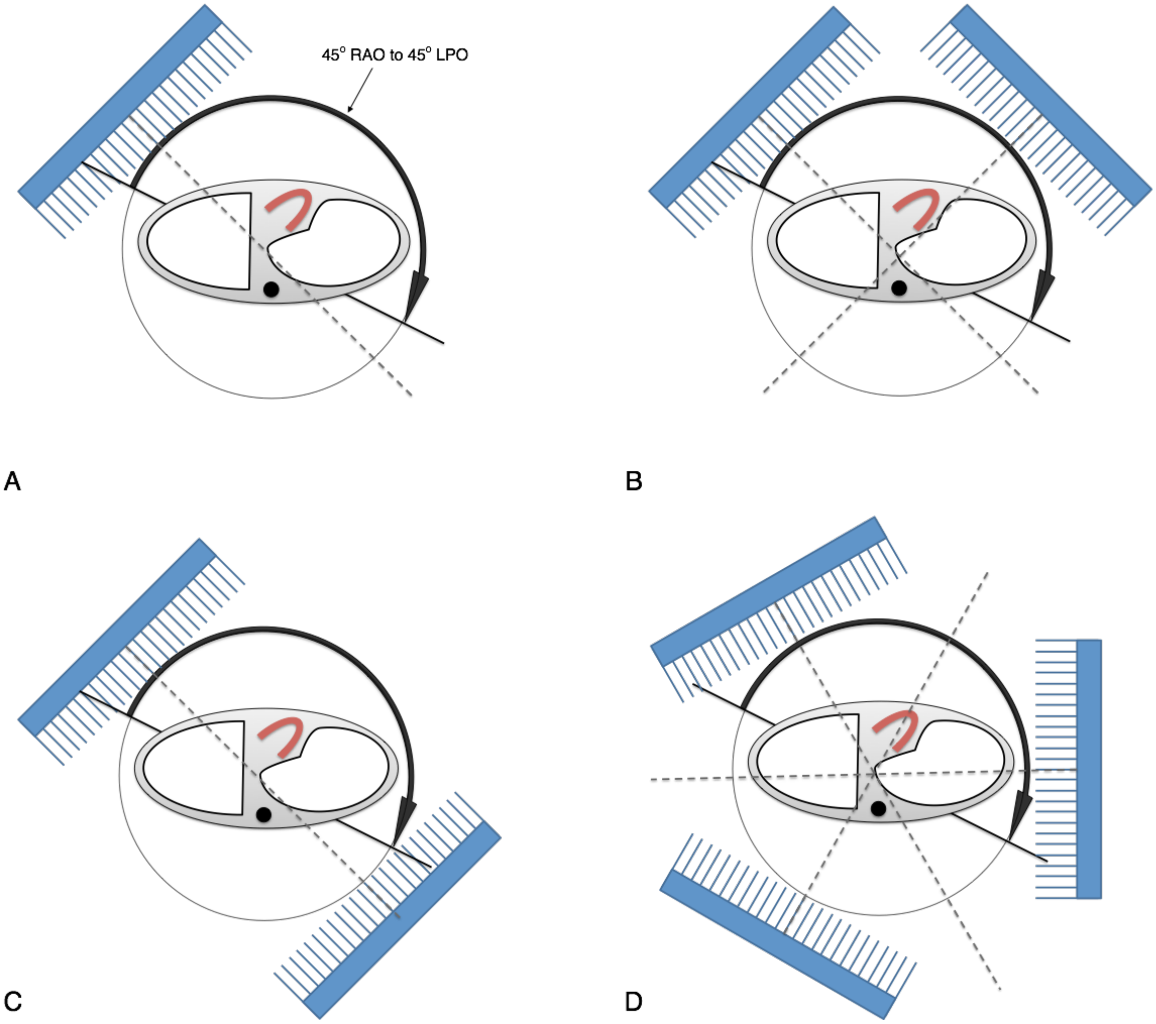

Figure 2.3 SPECT camera configurations. A: Single detector camera. B-D: Multi detector cameras with different camera configurations. LPO left posterior oblique, RAO right anterior oblique.

Myocardial perfusion imaging (MPI) is a routinely performed clinical study in nuclear medicine. A MPI study involves the administration of a radiopharmaceutical that perfuses into the myocardium. The two most frequently used isotopes in SPECT MPI are Thallium-201 (Tl-201) and technetium-99m (Tc-99m) sestamibi. Tl-201 has a half-life of 73 hours, and emits photons that have energy of about 80 keV, which is a low energy. On the other hand, Tc-99m has a half-life of 6 hours emitting photons with 140 keV energy. This energy is much lower than the 511 keV emissions of PET radiopharmaceuticals. Regardless of the radiopharmaceutical used, SPECT imaging of the heart is performed under rest and stress conditions to produce images of myocardial uptake that indicate relative regional blood flow. During maximal stress, the blood flow to the myocardial tissue is increased three to five fold compared to the rest state. In the presence of CAD, myocardial perfusion will not increase in the area supplied by the artery with the defect.

Tl-201 acts as a potassium analogue that is taken up by viable myocardial cells in proportion to coronary blood flow – its retention implies the functionality of the myocardium. The areas of infarction will have reduced uptake that does not change over time. The Tc-99m-labeled agent, sestamibi, is the most studied agent due to its sufficiently long retention time. Its uptake requires viable myocardial cells and it has far less redistribution than Tl-201, as Tc-99m is bound within the myocardial cell in a close to permanent fashion. Therefore, it must be injected twice, once at rest, and then during stress. A perfusion deficit observed only in stress images indicates a reversible defect caused by CAD, indicating that the myocardial tissue is still viable. On the other hand, a matched defect in both the stress and rest images indicates an infarct and the presence of non-viable myocardial tissue. This contrast offers critical impact on the optimal treatment for the patient, thus making the stress-rest protocol a standard practice in myocardial perfusion imaging.

The advantages of the Tc-99m such as better image quality, better ventricular function assessment, better quantification and faster imaging protocols are the most important considerations and account for increased use of this agent in most nuclear cardiology centers.

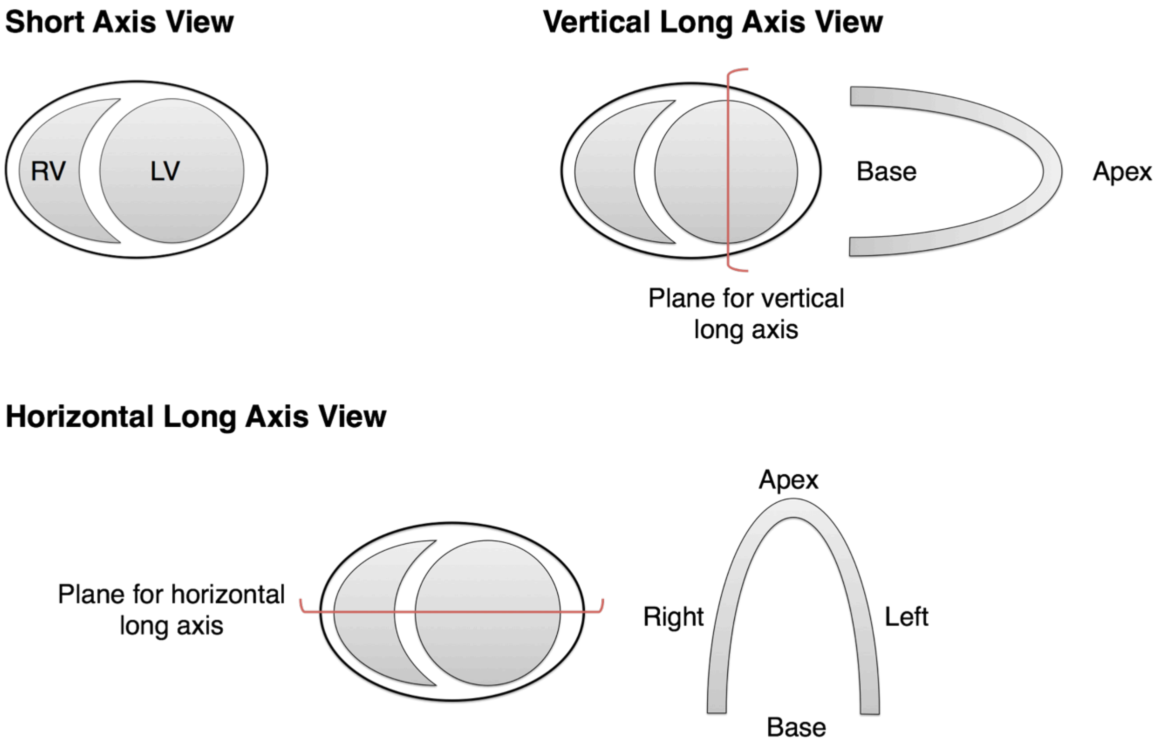

Short Axis View

Vertical Long Axis View

Horizontal Long Axis View

Figure 2.4 Schematics illustrating the standardized display of reconstructed cardiac SPECT slices.

The assessment of the reconstructed images usually involves a visual inspection using the short- and long-axis slices through the left ventricle as shown in Figure 2.4. In normally perfused myocardial tissue, the tracer distribution should be uniform throughout each of these slices without any regions of reduced uptake or deficits. Assessing the results in a quantitative manner can be done with use of a polar map, in which the entire left ventricle is displayed as a circular area, with the apex of the ventricle at the center and the base at the edge. This polar map is divided into 17 segments to compare the uptake in different regions of the myocardium as illustrated in Figure 2.5, an arrangement recommended by the American Heart Association [5].

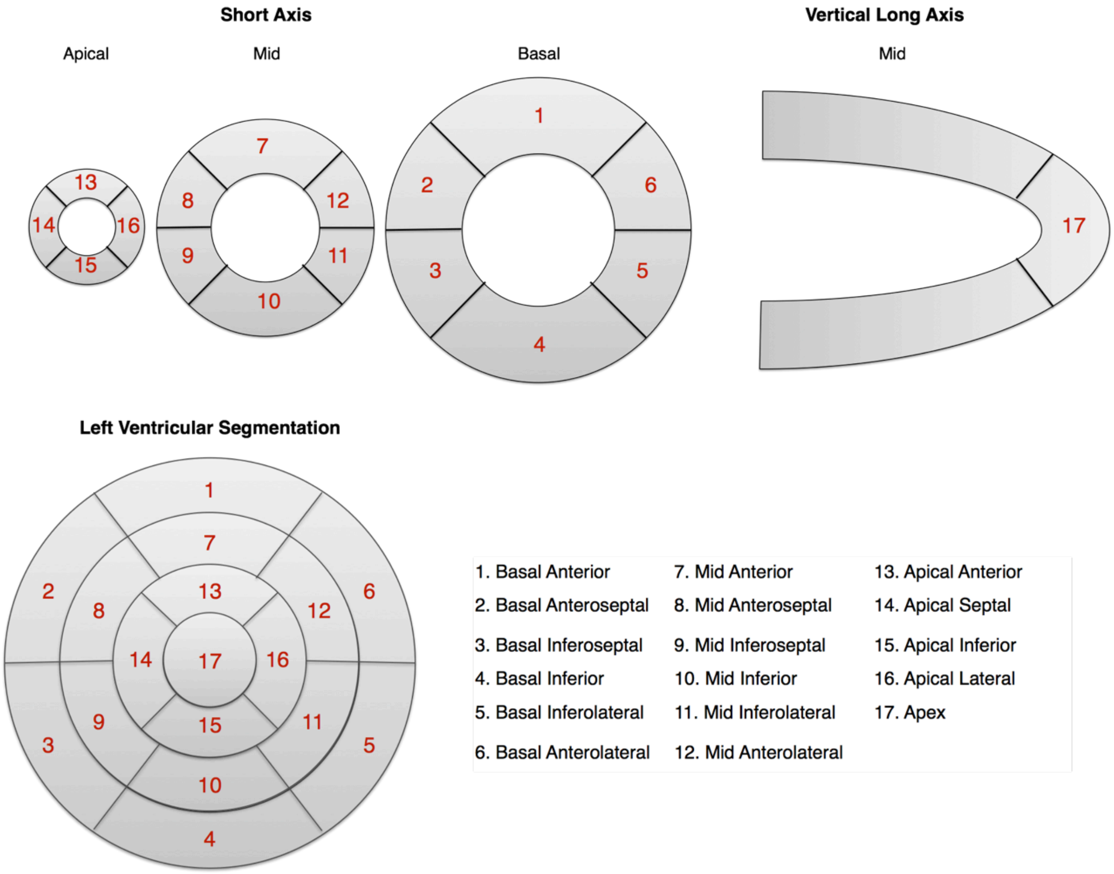

1. Basal Anterior
2. Basal Anteroseptal
3. Basal Inferoseptal
4. Basal Inferior
5. Basal Inferolateral
6. Basal Anterolateral
7. Mid Anterior
8. Mid Anteroseptal
9. Mid Inferoseptal
10. Mid Inferior
11. Mid Inferolateral
12. Mid Anterolateral
13. Apical Anterior
14. Apical Septal
15. Apical Inferior
16. Apical Lateral
17. Apex

Figure 2.5 The standard 17 segment model polar map is shown with the segmentation and number assignment.

The tracer distribution in an MPI study can be corrupted by factors such as attenuation and the effects of motion occurring during the acquisition. In SPECT cardiac imaging, body motion has been determined to occur in ~25% of studies and is significant enough to cause artifacts leading to misdiagnosis ~5% of the time [6, 7]. Respiratory motion is present in all SPECT MPI studies. A study showed that the largest extent of motion of the heart was found to be in the superior-inferior (SI) direction with a mean translation of 8.25 mm, with the next largest motion in the anterior-posterior (AP) direction, but less than half of the SI motion [8]. These motions caused by the diaphragm and the ribcage increase the cross-sectional area of the thorax [9] resulting in the blurring of the heart structures producing apparent decreased activity in the inferior and anterior walls usually mistaken for perfusion deficits [10-14]. Multi-modality imaging studies, such as SPECT/CT and PET/CT, have reported moderate to severe mismatches between the emission and anatomical transmission images in 40% of the patient studies due to patient motion and changes in respiratory pattern [15, 16].

Images from typical cardiac SPECT studies suffer from high noise levels due to the reduced number of counts in each frame resulting in the lack of anatomical detail. This not only impacts the ability to determine the motion from such images but also makes it challenging to understand the internal motion in order to correct for it. Alternative methods for observing and understanding motion would be 3-D X-ray stereophotogrammetry [17] and computerized tomography (CT), but cannot be used as a routine tool as the X-ray dose becomes critical when multiple datasets are needed.

MRI on the other hand has many advantages, as it provides excellent contrast between the soft tissues, and images can be acquired without the use of ionizing radiations at any orientation. In the following section a brief introduction to MRI is given. The aim is to introduce the basics of MRI that is needed to understand the main principle behind the imaging technique used in this dissertation.

2.3 An Introduction to Magnetic Resonance Imaging (MRI)

The spectroscopic study of the magnetic properties of the nucleus of the atom is Nuclear magnetic resonance (NMR), a solid method for the investigations of the chemical and physical properties at the molecular level. NMR was primarily used by chemists to determine the structure and configuration of molecules. In 1973, Paul Lauterbur proposed the use of magnetic field gradients to differentiate NMR signals originating from different locations integrating this with a reconstruction from projections to form the first two-dimensional NMR image [18]. The efforts of Kumar et al. [19] and Mansfield [20] in the imaging techniques and the required hardware, changed magnetic resonance imaging (MRI) into a non-invasive method of choice to examine anatomic and physiologic properties of the soft tissues with superior contrast to computed tomography (CT) without the use of nonionizing radiation.

2.3.1 Basic Physical Principles

To better understand the phenomenon of NMR, the basic physical principle of electromagnetic (EM) theory is required.

2.3.1.A Electromagnetic Theory

Wave concept of EM Radiation

EM radiation is a form of energy, which exhibits wave-like behavior as it travels through space. It has both electric and magnetic field components which oscillate in phase perpendicular to each other and perpendicular to the direction of energy and wave propagation. EM wave propagates at the speed of light (Figure 2.6) as characterized by the classical wave equation:

$$v = c/\lambda \tag{2.1}$$

where c is the speed of light (3.0×10^8 m/s), λ is the wavelength (m) and v is the frequency (s^{-1}).

Particle Concept of EM Radiation

EM radiation exhibits particle nature as if it were particles rather than waves. These particles were discrete packets of energy called quanta, characterized by a specific radiation frequency. The actual energy of these packets may be calculated, using the particle frequency and Planck's constant.

$$E = hv \tag{2.2}$$

where h is Planck's constant (4.13×10^{-18} keV.s), v is the frequency (s^{-1}), and E is the energy (keV).

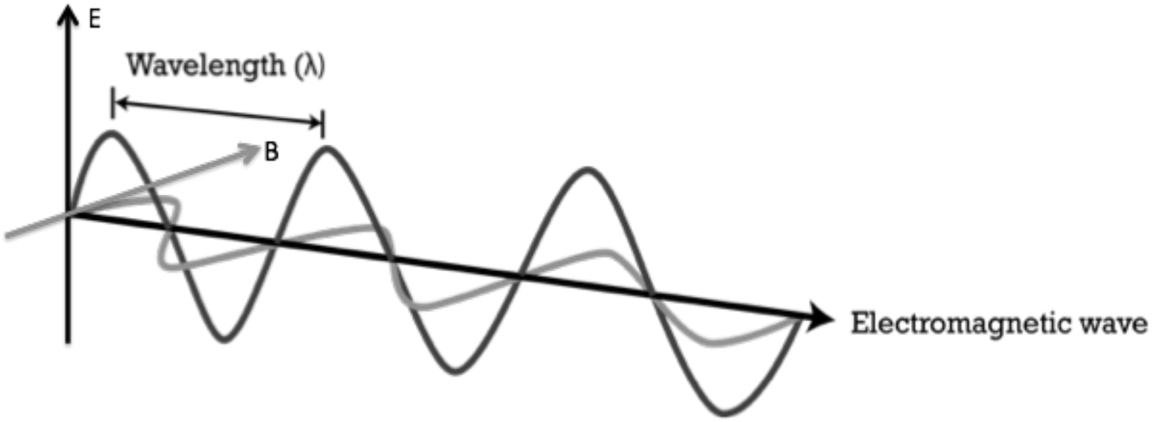

Figure 2.6 Components of the electromagnetic (EM) wave. E is the electric component and B is the magnetic component. These two components are perpendicular, have the same frequency, and travel at the speed of light, C.

2.3.2 MRI and the EM spectrum

Magnetic resonance is associated with the interaction of the frequency components of the EM spectrum in the radio frequency range, which typically ranges from 5-200MHz (Figure 2.7).

Spin Angular Momentum in a Magnetic field

Most nuclei possess a property called spin angular momentum, which forms the basis of nuclear magnetism. Figure 2.8 depicts a nucleus spinning about its own axis. Since atomic nuclei are charged, the spinning motion causes a magnetic moment which is linear with the direction of the spin axis. The magnetic moment behaves similar to a bar magnet with north and south poles. The strength of this magnetic moment is a property of the type of nucleus and determines the detection sensitivity of MR as in Table 2.1. ^{1}H nuclei (protons) have the strongest magnetic moment, which, together with the high biological abundance of hydrogen, makes it the nucleus of choice for MR imaging.

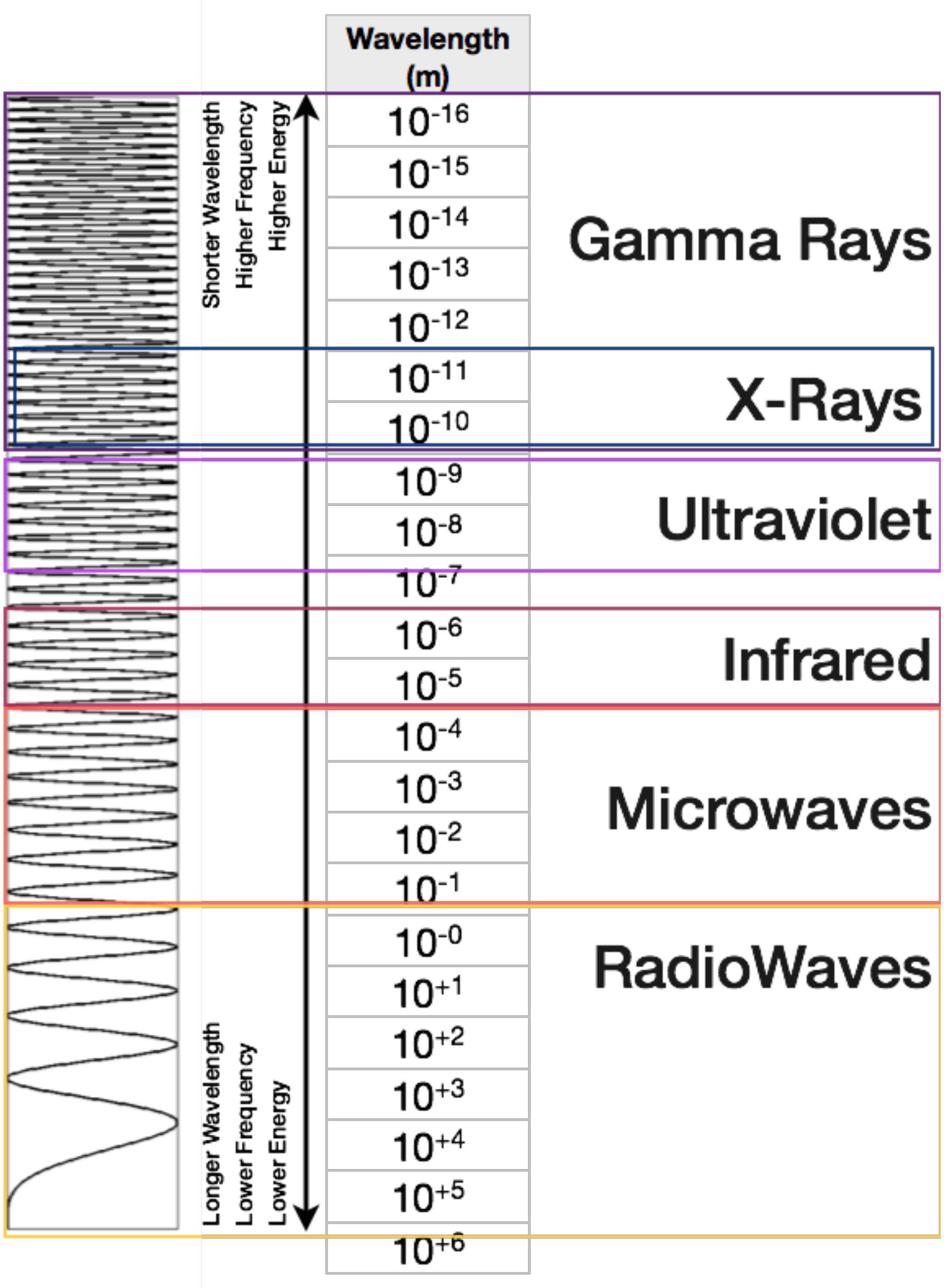

Figure 2.7 The electromagnetic (EM) spectrum. The various types of EM waves are noted on the right, starting with high-energy gamma rays and x-rays at the top, and ending with the low-energy radiowaves at the bottom.

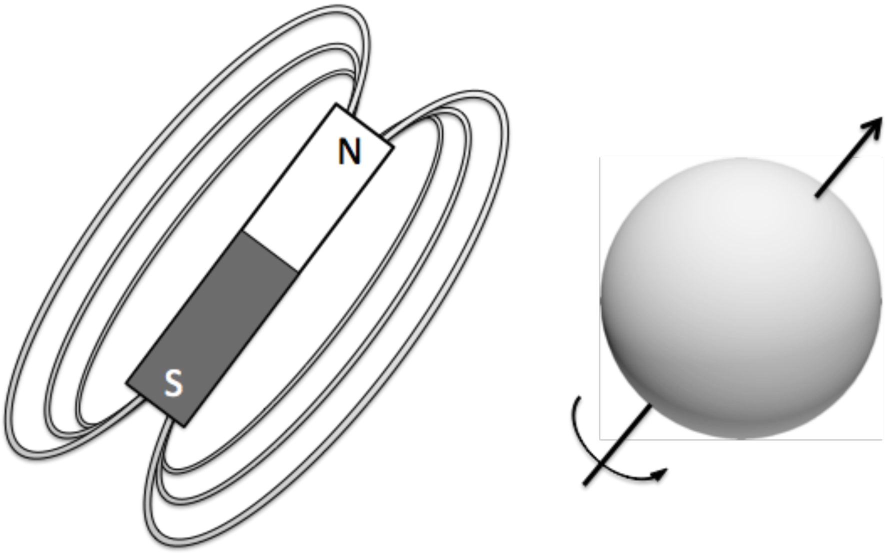

Figure 2.8 The magnetic dipole and associated spin of nuclei can be compared to a bar magnet with rotation about the dipole axis.

Table 2.1 Table of Nuclear Properties

Nucleus	# Protons	# Neutrons	Spin Quantum Number (I)	% Natural Abundance	Gyromagnetic Ratio* (MHz/T)
^{1}H	1	0	1/2	99.98	42.58
^{13}C	6	7	1/2	1.1	10.71
^{17}O	8	9	5/2	0.04	5.77
^{19}F	9	10	1/2	100	40.08
^{23}Na	11	12	3/2	100	11.27
^{31}P	15	16	1/2	100	17.25

*Note that the gyromagnetic ratios reported here are expressed in terms of $\gamma/2\pi$.

Consider a group of protons as shown in Figure 2.9. In the absence of an external magnetic field, the individual magnetic moments are randomly oriented. However, in the presence of an externally supplied magnetic field (B_0), there is a tendency for the

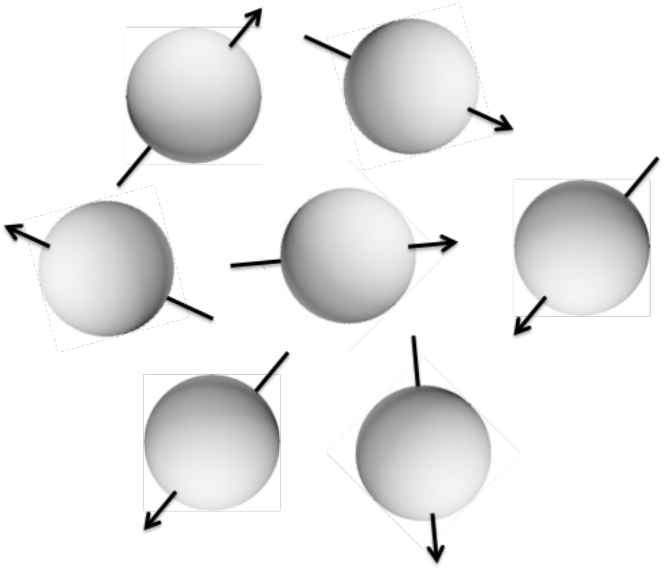

Figure 2.9 In the absence of an externally applied magnetic field, the nuclear magnetic moments have random orientations.

magnetic moment to align with the external field, similar to bar magnets' behavior. Nuclear magnetic moments in this situation take on one of two possible orientations: alignment parallel or anti-parallel to B_0 Figure 2.10. Thus, depending on their orientation, we can define two populations of spins. Alignment parallel to B_0 is the lower energy orientation and is thus preferred, while the anti-parallel alignment is the higher energy state Figure 2.11. This situation of only two allowed states is true only for nuclei whose magnetic spin quantum number is equal to ½. This includes ^{1}H, ^{13}C, ^{19}F, ^{31}P and others.

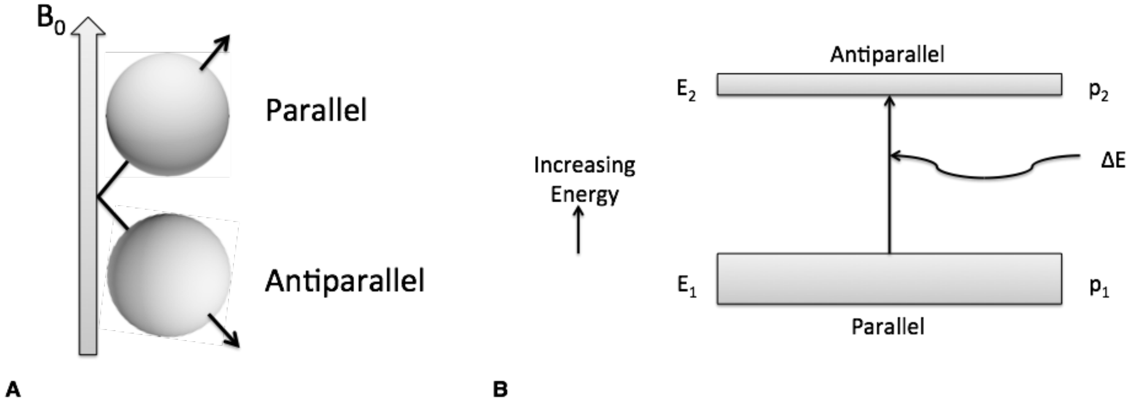

Figure 2.10 A: In the presence of an externally applied magnetic field (B_0), spins are constrained to adopt one of two orientations with respect to B_0. These orientations are represented as parallel and anti-parallel. B: The parallel spin orientation is a lower energy state than anti-parallel. Since spins must adopt one of the two orientations, there are two populations (P_1, P_2) of spins corresponding to the two energy levels (E_1,E_2). $E_2 > E_1$, causing $P_1 > P_2$. $\Delta E = E_2 - E_1$, is the amount of energy supplied to the system to move some spins of P_1 to P_2.

One may question that all of the spins would occupy the lower energy state. This would be true at a temperature of absolute zero, but we are interested in the situation under normal room temperature conditions. Since the energy difference (ΔE) between the two states is very small, thermal energy alone causes the two states to be almost equally populated (the population ratio is approximately 100,000 to 100,006). The remaining population difference results in a net bulk magnetization aligned parallel to B_0. It is only this net magnetization arising from a small population difference that is detectable by MR methods.

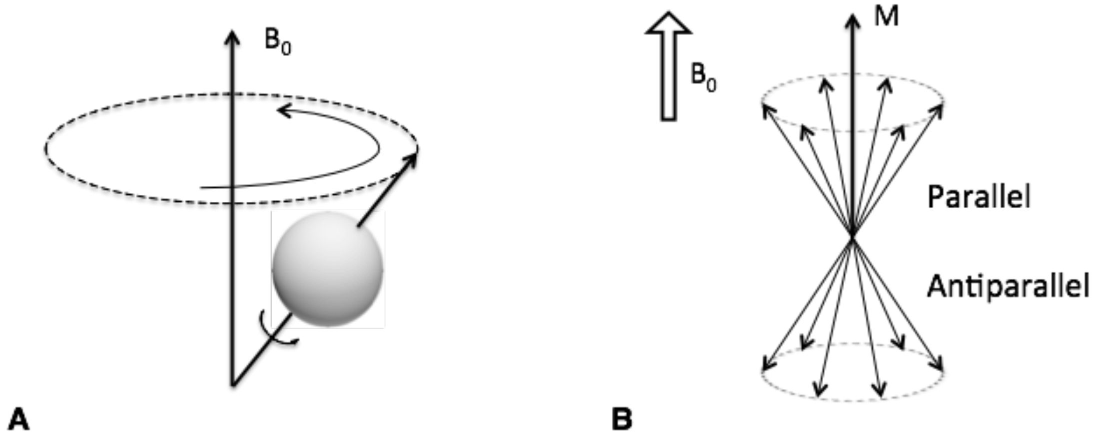

Figure 2.11 A: The spin axes do not act align parallel or anti-parallel to B_0. This orientation forces spin axis to precess likes a top around B_0. B: Representation of a collection of spins at any given instant. The vector M represents the net magnetization which results from the sum of the contributions of the spins.

On closely examining this net magnetization, the individual spins do not align exactly parallel to B_0, but at an angle to B_0 Figure 2.11. A. The spin associated with the magnetic moment causes the moment to precess around the axis of B_0, analogous to the scenario of a spinning top, this precession then defines the surface of a cone. A large collection of spins yields a net bulk magnetization. Figure 2.11.B shows an illustration of the situation at any given time. Here, each of the arrows represents an individual spin. Since we already know that there are more spins aligned with B_0 than against B_0, the contribution of the bottom cone cancels out, leaving only the excess spins of the top cone to consider. Any given vector on the top cone could be described by its component perpendicular to and parallel to B_0. Clearly, for a large enough collection of spins randomly distributed on the surface of the cone, individual components perpendicular to B_0 will cancel each other, leaving only the contributions parallel to B_0, explain the reason for the net magnetization to be parallel to B_0.

The frequency at which these individual spins precess on the cone is called Larmor frequency which is given by a simple relation ship called L armor equation

$$\gamma B_0 \ = F \tag{2.3}$$

where F is the precessional frequency, B_0 is the strength of the magnetic field, and gamma (γ) is related to the strength of the magnetic moment for the type of the nucleus considered.

The effect of Radiofrequency (RF) Pulses

In order to detect a signal, resonance needs to be established. The term ”resonance” means alternations absorption and dissipation of energy. Energy absorption is caused by RF excitation, and the energy dissipation is mediated by the relaxation processes.

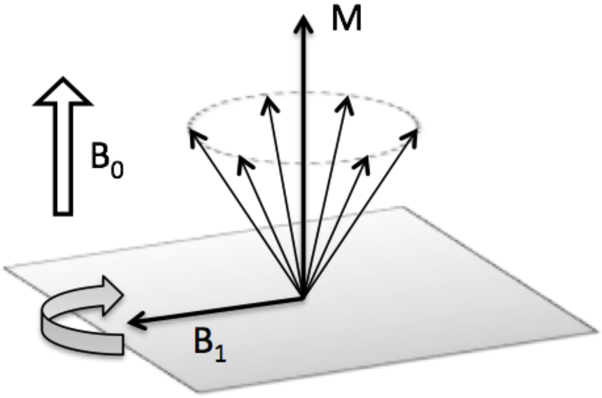

Figure 2.12 A RF energy at the Larmor frequency acts as a secondary magnetic field (B_1) and is perpendicular to B_0. When RF is turned on, the magnetization vector M rotates about B_1. As shown here, originally M is longitudinal and when B_1 is turned on long enough to rotate M by 90°, into the transverse plane.

RF radiation possesses both electric and magnetic field components. Considering RF as another magnetic field B_1, perpendicular to B_0, as shown in Figure 2.12. When the RF is turned on, the magnetization vector (M) precesses about the B_1 axis. This the net magnetization rotated from the longitudinal (Z) axis toward the transverse plane then toward the –Z axis, then to the other side of the transverse plane, and back to +Z and so on. If the RF is on for only a short period of time, the net magnetization is rotated by a certain angle away from the longitudinal axis; which is called the *flip angle*. Flip angle is proportional to the duration of an RF pulse and the amplitude if the RF pulse.

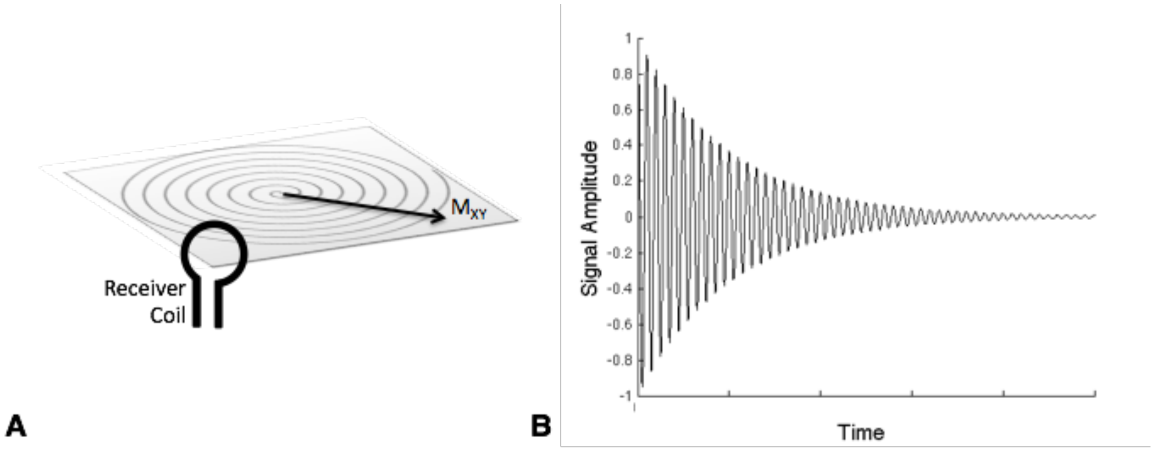

Figure 2.13 A: Once the B_1 is turned on, M lies in the transverse plane rotating about B_0 at Larmor frequency. This rotating magnetization induces and AC current in the receiver coil. The transverse magnetization (M_{XY} or $M_{Transverse}$) decays over time. B: A graph of the signal induced in the receiver coil versus time. This exponentially damped sine waveform is known as free induction decay (FID). The decay rate is characterized by the time constant T_2^*.

Consider, a time immediately after a 90^o pulse Figure 2.13. A. The net magnetization now lies in the transverse plane and begins to precess around the B_0 axis. This rotating magnetization over time, can induce and alternating current (AC) in a coil of wire and that current can be used to record the action of magnetization in the transverse plane as shown in Figure 2.13. B. It shows a sinusoidal oscillation at the Larmor frequency with decreasing amplitude over time, which is termed as free induction decay (FID). This signal decay is due to a process known as relaxation.

2.3.3 Relaxation Processes

The net magnetization arising from a group of spins in an external magnetic field, equilibrium is described by a vector of unit length parallel to B_0. There are two main relaxation mechanisms namely 1) Transverse Relaxation and 2) Longitudinal Relaxation.

Transverse Relaxation

At equilibrium the net magnetization is longitudinal, which implies that the equilibrium magnetization in the transverse plane is zero. As illustrated in Figure 2.12. B, the decay of the transverse magnetization to zero. This process is exponential. The relationship describing the decay is :

$$M_{Transverse} = M^0_{Transverse}(e^{-t/T_2^*}) \tag{2.4}$$

Where $M^0_{Transverse}$ is the initial amount of transverse magnetization, $M_{Transverse}$ is the amount of transverse magnetization at any given time (t) after a pulse, e is approximately 2.7 and T_2* characterizes the rate of decay. Hence, T_2* is the time it takes for the transverse magnetization to decay to 37% of the initial value. The mechanisms that cause the observed decay of transverse magnetization: as shown in Figure 2.14, different compliments of the magnetization may prescess at slightly different rates, a process known as “dephasing” in the transverse plane. Since the signal recorded is the sum of all the transverse components, sufficient dephasing will lead to complete cancellation of the signal. One of the major causes of this dephasing is B_0 inhomogeneity: Spins at different locations are not exposed to exactly the same B_0 field, which in turn use a range of Larmor frequencies. If one had a homogeneous B_0 field, dephasing would still occur but at a slower rate. This is because many nuclei and electrons are spins and possess magnetic moments; the microscopic local magnetic environment of a spin participating in the observed resonance is not precisely identical to those of the other observed spins. Moreover, these microscopic environments change very rapidly, this spatial and temporal variation of magnetic environments lead to the variation in Larmor frequencies causing slower dephasing.

Longitudinal Relaxation

After a 90^o pulse, the net magnetization vector is rotated into the transverse plane such that the amount of longitudinal magnetization is zero. If the amount of longitudinal magnetization is examined at various times after the 90^o pulse, one finds that it builds up exponentially from zero to approach the equilibrium value (M_0), which is a function of spins present, temperature and magnetic field strength (fig 2.13). This process is knows as spin-lattice relaxation or T_1 relaxation.

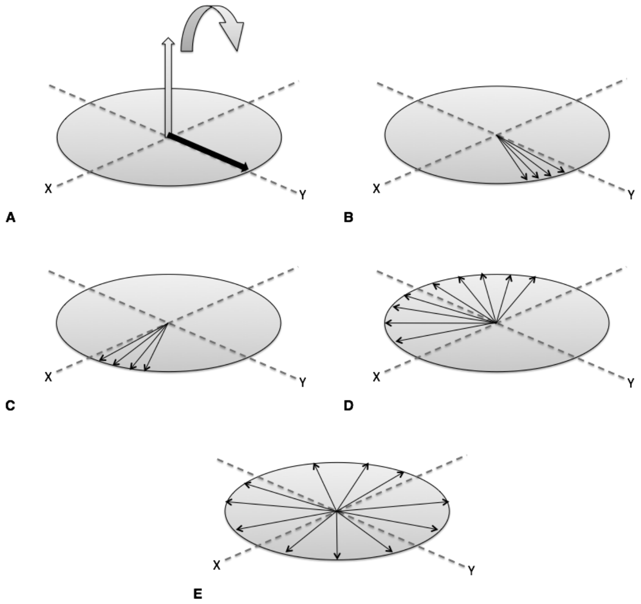

Figure 2.14 A: The B_1 of the RF rotates M into the transverse plane. (B-E) This rotating magnetization in the transverse plane is the sum of the contributions from all of the spins in the excited sample. Due to B_0 inhomogeneity, the spins at different points feel the same B field resulting in a range of precessional frequencies causing the spins to spread apart over time eventually leading to self-cancelation of the signal.

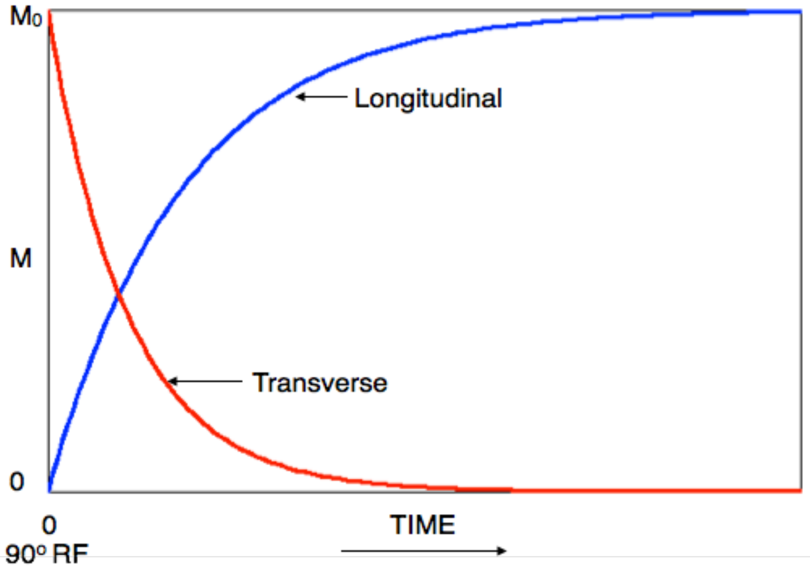

Figure 2.15 After a 90° RF pulse, all of the magnetization vectors lie on the transverse plane. T_2 processes and magnetic field (B_0) inhomogeneity lead to an exponential decay of the Transverse magnetization (M_{XY}) while the longitudinal magnetization (M_Z) increases exponentially with time.

Both the longitudinal relaxation and transverse relaxation processes are characterized by exponential evolution. The transverse magnetization decays from maximum to zero, while the longitudinal magnetization builds up from zero to maximum. The quantitative expression for T_1 relaxation can be described as:

$$M_{Longitudinal} = M^0_{Longitudinal}(1 - e^{-t/T_1}) \tag{2.5}$$

where $M^0_{Longitudinal}$ is the initial amount of longitudinal magnetization (M_0), $M_{Longitudinal}$ is the amount of longitudinal magnetization at any given time (t) after a pulse, and T_1 characterizes the rate of magnetization recovery. Different types of tissues (blood, fat, muscle, etc.) have different relaxation times resulting in contrast in MR images. In comparing T_1 and T_2 for any given system, T_1 is always greater than or equal to T_2. The MR signal decays with an even shorter rate constant of T_2^*; this decay constant primarily arises due to the dephasing effects of the magnetic field inhomogeneities (susceptibility differences between tissues) over the region of interest. In the presence of magnetic field inhomogeneities, the magnetization vectors diphase with respect to each other causing signal attenuation due to destructive interference. The effects of this inhomogeneous decay can be reversed using techniques that generate the so-called spin echoes [21], in which case the decay rate T_2 is revealed. Figure 2.16 depicts and RF pulse sequence for a spin-echo. Note that the echo-to-echo amplitudes decays as a function of T_2.

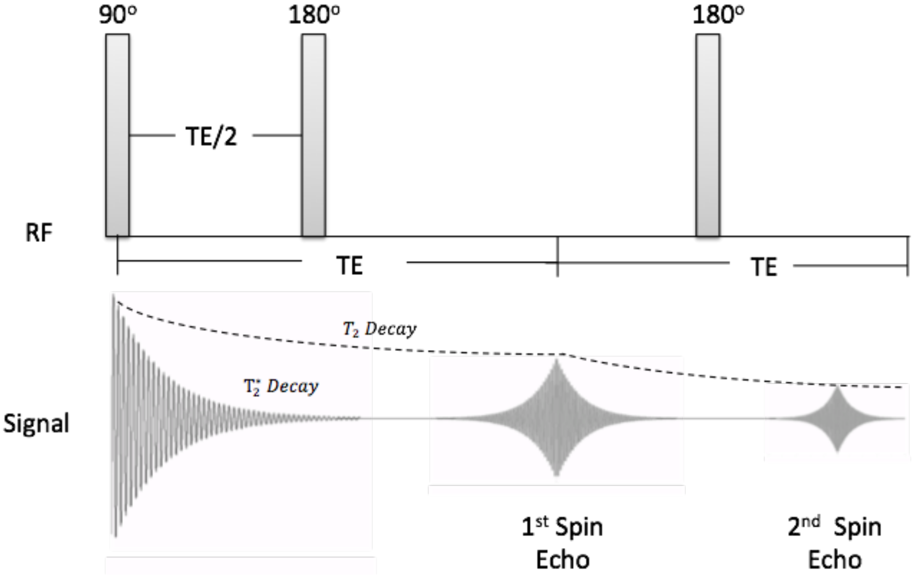

Figure 2.16 A spin-echo is generated by the application of a 90° RF pulse and after a delay (TE/2), a 180° RF pulse. The peak of the echo occurs at time TE after and initial 90° pulse. More echoes are obtained with an additional 180° pulses. The echo-echo decay rate is described by T_2.

For the formation of MR images encoding magnetic field gradients are of great importance. Magnetic field gradients refer to spatial variations of the strength of the magnetic field (B_0). Gradients provide the means for performing localized operations. The gradient field is a very small magnetic field with spatial variation which is superposed on the main magnetic field (B_0). Gradient fields in the directions of X, Y and Z are achieved by three sets of coils. In the presence of the gradients, the transverse magnetization precesses at a frequency proportional to the position along the gradient axis and is given as:

$$F = \gamma(B_0 + rG_r) \tag{2.6}$$

where r is the position along the axis of the gradient G_r. The presence of a gradient has very little effect on longitudinal magnetization.

Slice selection in MR imaging is achieved through simultaneous application of the B_1 field (RF pulse) and gradient field [22]. A modulated RF pulse excites the magnetization with a limited range of frequencies. The gradient field is varied linearly in the slice selection direction such that the magnetizations within the block are excited. Adjusting the amplitude and the direction of the slice selection gradient controls the thickness and orientation of the block while the slice profile is dictated by the duration and the modulation of the RF pulse.

The excitation through RF pulse and imposition of the gradient fields causes the magnetization in different regions of the slice to precess with a spectrum of frequencies as dictated by equation (1.6). This spectrum can be obtained by performing a Fourier transformation (FT) on the MR signal recorded by the receiver coil, thereby resulting in the one-dimensional (1D) spatial profile.

Through the combined use of the gradient fields, the spatial distribution of magnetization is mapped on to a k-space, a 2D Cartesian matrix where, one row of data matrix is acquired at a time and the process is repeated until the matrix is filled. Images are then reconstructed using the 2D FT on the k-space data.

A timing diagram for the gradient echo imaging pulse sequence is depicted in Figure 2.17. Gradient echo imaging is one of the major modes of MR imaging especially when imaging the heart. A sequence of short small-amplitude RF pulses is generated and the MR signal is acquired after each RF pulse. Spatial encoding is done through the use of gradients applied in the frequency encoding direction and in the orthogonal phase encoding direction, by repeating this several times in the phase encoding direction with increasing amplitudes of phase encoding gradient pulses. The length of this pulse sequence till it repeats next is defined as TR (repetition time) and the time from the center of the RF pulse to the center of the acquisition window is TE (echo time). The pulse sequence parameters (TR, TE and flip angle) along with the tissue specific magnetic relaxation properties T_1, $T_2$and T_2^*, give rise to contrast between the tissues.

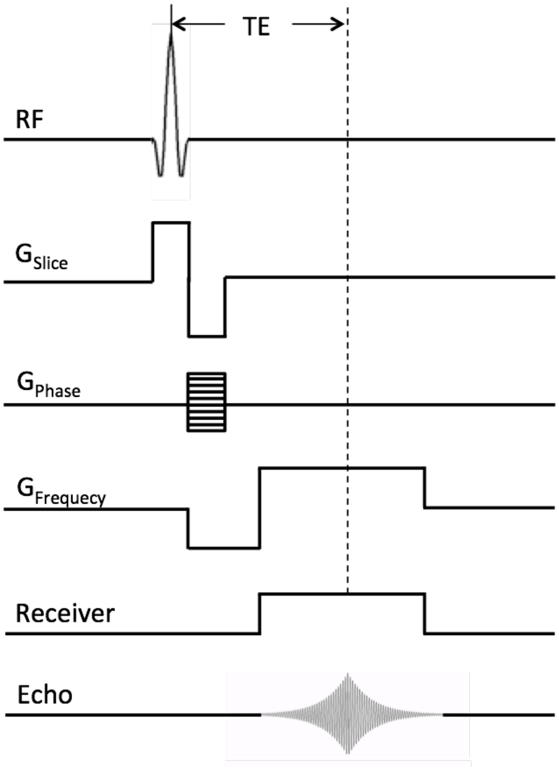

Figure 2.17 Timing diagram for gradient echo pulse sequence

The receiver coil detects the transverse magnetization, which has both magnitude and phase information used to perform spatial encoding. Thus, each pixel in the MR image is a complex number representing the magnitude and the phase of the transverse magnetization at time TE.

Cardiac imaging presents the challenge of cardiac motion during image acquisition along with respiratory motion. One approach to meet this challenge is to acquire images rapidly by using short TR in a single electrocardiogram-gated cardiac cycle along with navigator echoes.

2.3.4 MRI navigators

Navigators or navigator echoes (Figure 2.18) are a technique used to track and correct motion artifacts [23]. Navigator data can be used to correct for motion either prospectively or retrospectively. A navigator acquires a partial k-space data to track the motion (e.g. head translation or diaphragm position). The acquisition of the navigator echoes and image data is done in an alternating fashion by adding a pre-pulse before the image data readout pulse, with a key assumption that negligible motion takes place between the navigator and the subsequent imaging acquisition. The pre-pulse sequence images a small area that is moving. The high contrast interface between the tissues is pre-set to '0' value, and marks this out as a potential edge point permitting easy automatic edge detection (or zero-crossing).

The navigators employed in this study use 1D k-space trajectory and are primarily used in tracking the respiratory motion of different organs. The 1D navigator monitors the translation of the object in its readout direction. The navigator data is processed using the cross-correlation or least-squares fitting methods [24, 25] to determine the object translation.

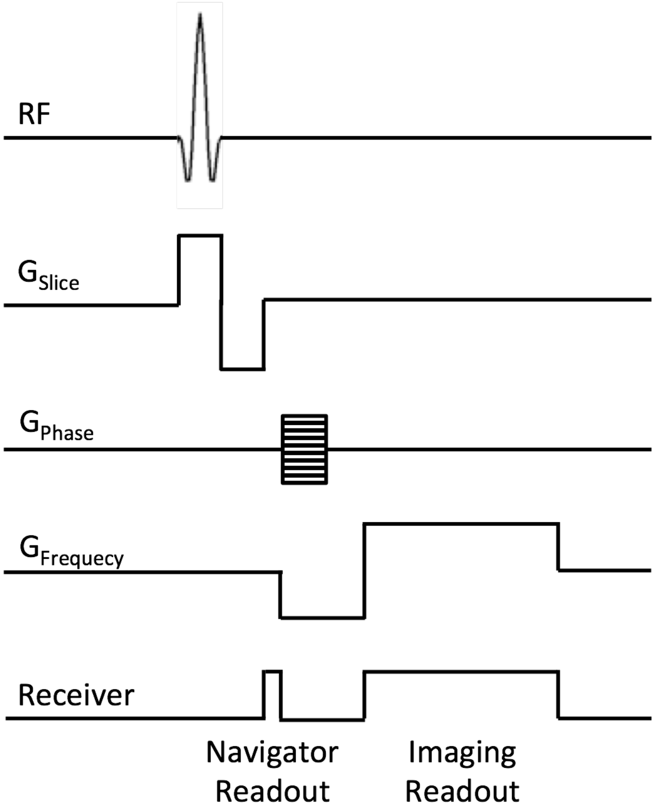

Figure 2.18 Timing diagram for gradient-echo pulse sequence using a single navigator point. The spatial encoding of the transverse magnetization is followed for imaging

The navigators employed in this study use 1D k-space trajectory and are primarily used in tracking the respiratory motion of different organs. The 1D navigator monitors the translation of the object in its readout direction. The navigator data is processed using the cross-correlation or least squares fitting methods [24, 25] to determine the object translation.

Navigator Placement

The navigator is usually positioned at the dome of the liver (right hemi-diaphragm) because the diaphragm is perpendicular to the SI direction at that location (Figure 2.19). Tracking of the diaphragm position using navigators not only allows for correcting the respiratory motion of the heart but also allows free breathing during the scan. Usually, a 1D navigator acquires a column of data in the SI (readout) direction through the right hemi-diaphragm.

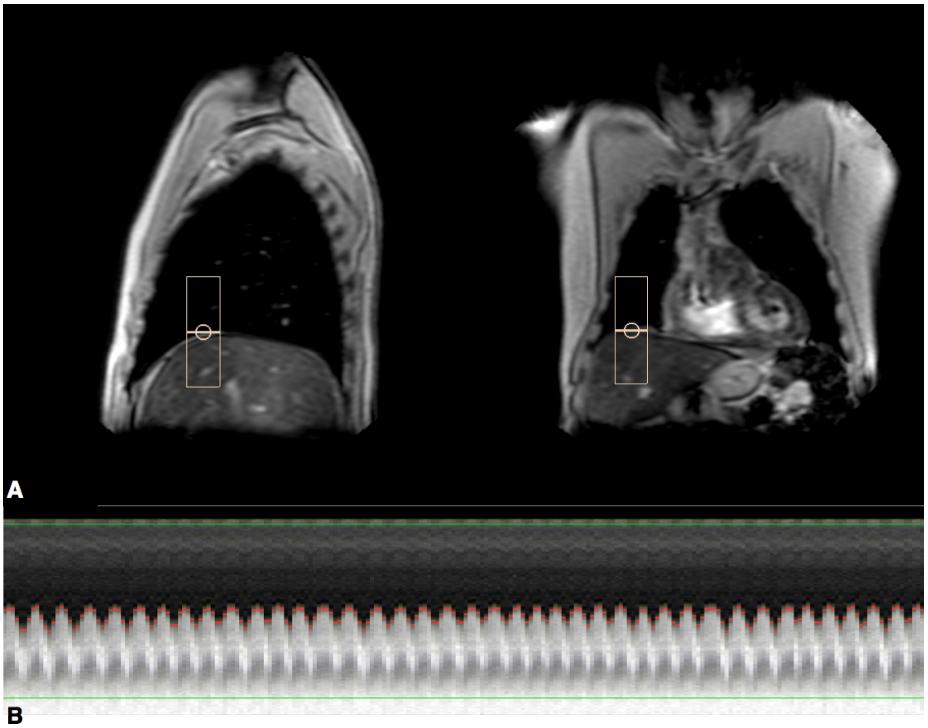

Figure 2.19 A: Placement of navigator on right hemi-diaphragm using sagittal and coronal survey scans. B: Navigator profile. The red points indicate the respiratory trace determined by cross-correlation in real-time.

Pulse sequence and Processing: a 1D navigator excites a 1-2 cm wide column of spins in the readout direction (along the column). Spatial resolution of the column is 1 mm. The 2D excitation can be achieved either through the use of spin-echo or gradient echo sequence. The navigator is played before the image acquisition within the same cardiac cycle for imaging in the quiescent phase of the cardiac cycle (Figure 2.20) or multiple cardiac phases. The settings chosen for using the 1D navigator technique to track and understand internal organ motion is discussed in more detail in Section 3.2.

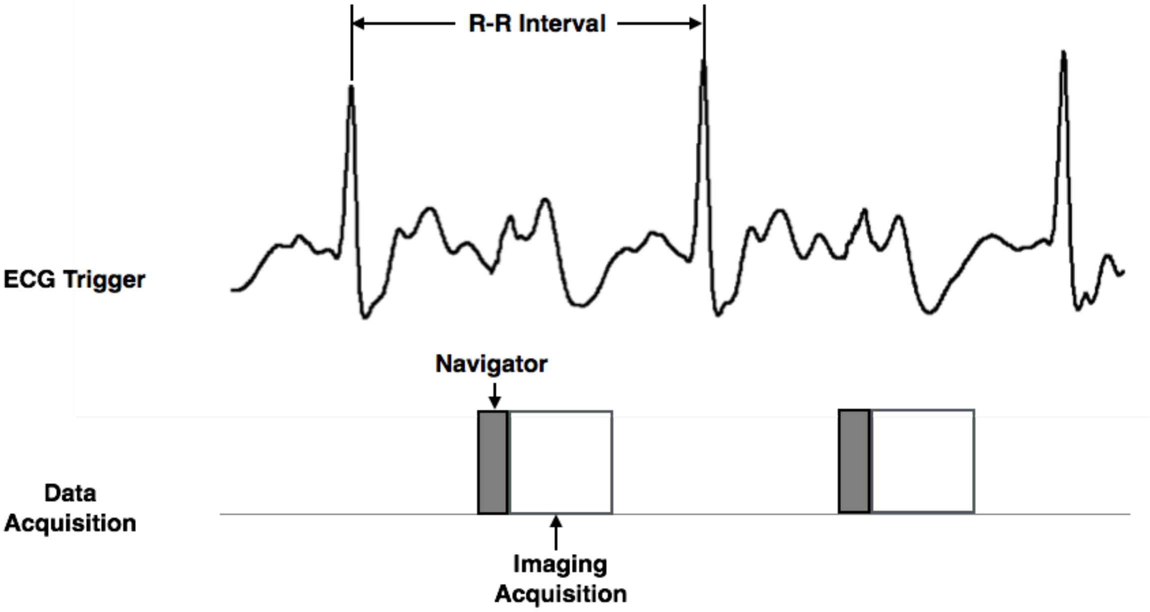

Figure 2.20 One navigator and acquisition per cardiac cycle. The shaded blocks represent the navigators. The plain blocks represent the imaging pulse sequence that acquires multiple phase encoding steps.

2.4 Respiratory Motion

The main mechanism of respiratory motion is through the contraction and relaxation of the diaphragm. Many of the organs in the thoracic and abdomen regions exhibit motions influenced by that of the diaphragm. The organs that are close to the diaphragm, such as the heart, the liver and the spleen are greatly affected. The motion in these organs has found to be dominated by SI motions with minimum displacements in the AP and lateral directions [8] indicating the influence of the diaphragmatic motion. The other process causing an increase in lung volume is the motion of the chest wall. The inter-coastal muscles contract during inhalation, tilting the rib-cage upwards and outwards, enabling the expansion of lungs [26]. The contribution of the chest wall motion to the overall increase in the lung volume is typically less than that from the diaphragm contraction [27]. The nature of motion observed is dependent on various factors, namely: posture (e.g. supine or sitting), breathing type (predominantly chest or abdomen) and depth of breathing (shallow breathing or deep breathing). These factors affect the extent of both the diaphragm and the chest wall and hence affect the motion of the internal organs.

The period of the typical respiratory cycle is around 5 seconds [28, 29], but is variable across the population and on the exercise levels. Changes in both the depth of respiration and the period of respiratory cycle are frequently observed [30]. These changes result in complex respiratory motions of organs such as the heart and liver, which are regularly changing in amplitude over time. The shape of the cycle approximates a sinusoidal wave with an inert phase observed at end-expiration [31].

The Respiratory Motion of the Heart

The motion of the heart is greatly influenced by the diaphragm motion due to the fact that it is situated immediately superior to the diaphragm [8]. The translational motion of the heart is consistently smaller than that of the liver; it has been reported that the mean heart to liver ratio is between ~0.45 to ~0.60 [8, 32]. The chest wall also influences the heart motion with small translations in the AP direction [33]. The SI translation is therefore the dominant motion component, with small translations in the AP and left-right directions as well as rotations [34]. The respiratory motion of the heart can be assumed to be rigid-body in nature [35] due to the fact that it experiences very little deformation due to translations and rotations.

In hysteresis, the motion traversed by an organ during exhalation is different to that during inhalation. Hysteresis has been investigated extensively for lung tumor motion [31, 36-38] and less for heart motion. Nehrke et al. [32] examined the correlation between the SI motion of the heart and the right hemi-diaphragm of 10 volunteers during free breathing using MRI [32]. Their study found 8 out of 10 volunteers to be hysteretic to some extent, with two volunteers having a linear/monotonic relationship between the heart and the diaphragm positions. The slope of the hysteresis behavior was in the same direction, representing a lag in the respiratory motion of the heart with respect to that of the diaphragm as shown in Figure 2.21.

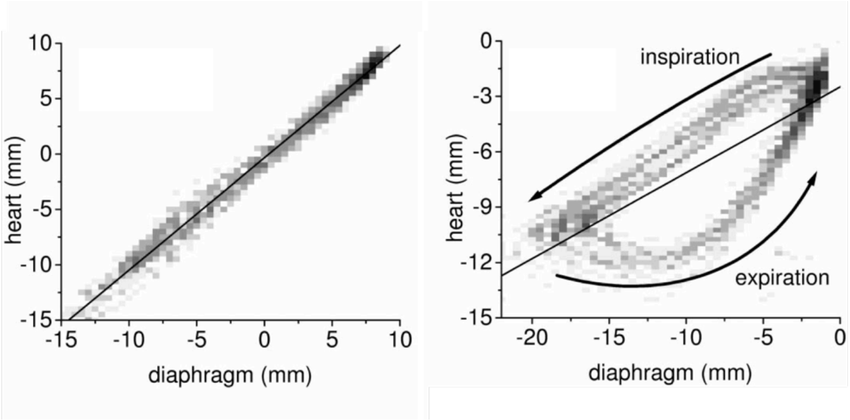

Figure 2.21 2D scatter plot of heart versus diaphragm motion for volunteers who showed linear/monotonic (left), and significant hysteretic (right) relationship. Plots are from Fig 3 of Nehrke et al. [32]

Effects of Respiratory motion During Myocardial perfusion Imaging

The respiratory motion present in all cardiac perfusion-imaging studies is inevitable due to the long scan duration (typically 3-15 minutes) [39, 40]. The effects of motion during cardiac perfusion study are blurring and mismatches between emission and transmission data.

The motion during acquisition results in blurring of the image; due to the constant field-of-view over the acquisitions, any motion occurring during the acquisitions will be registered in the image data. Both cardiac and respiratory motions are inevitable due to the length of the acquisition causing substantial image degradation [41].

The problem of mismatch arises in the process of attenuation correction. The motion occurring either during the emission and transmission scan or between the scans results in mismatches between the two. The mismatched transmission scan used for attenuation correction of the emission data will introduce errors by generating erroneous correction factors and eventually leading to artifacts in the reconstructed image. McCord et al. through simulations demonstrated emission-transmission mismatch as a problem for cardiac PET-CT: they showed that shifts of 2 cm motion could produce significant errors in the reconstructed images, with changes up to 30% in the regional activities [15]. Such misrepresentation in the apparent and regional myocardial uptake clearly limits the efficacy of the study and potentially leading to false positive results.

The occurrence of emission-transmission mismatches in cardiac images due to respiratory motion has been found to be quite high. Studies have reported that mismatches occurring when free-breathing protocol was used throughout the acquisition affected approximately 70% of clinical cases [42, 43]. Gould et al. showed that 40% of the cardiac studies exhibited attenuation correction artifacts, of which 23% were deemed as being moderate to severe [44]. It is evident that the problem of attenuation correction mismatch is important, both due to its widespread manifestation and the severity of the artifacts.

Mitigating these problems requires the prevention of motion corruption in the image data and error-free matching of the emission and transmission datasets. It is imperative to eliminate the effects of motion from both the emission and transmission scans to accurately quantify the images. Many methods have the potential to reduce these problems, which will be discussed in the following section.

Respiratory Gating

Respiratory gating is a method that employs a physiological signal recorded simultaneously with the image acquisition to divide the acquired data into frames. This method is apt for periodic/cyclic motions, such that each gated frame contains only a portion of data that is associated with a specific part of the cycle. Thus each gated frame contains very little motion and can be applied to both the cardiac and respiratory cycles. Dividing the data into little motion frames serves as starting point for motion correction wherein the frames are subsequently aligned and re-summed. This results in motion-free images with inclusion of most or all of the acquired data, resulting in very low noise characteristics in the final image.

A wide variety of techniques for recording respiratory traces using external measures have been developed, many for use with radiotherapy [45] to improve the accuracy of the treatment delivery. Most of these techniques are based on measuring the motion of the chest-wall or abdomen, which include the tracking of reflective marker [46, 47], and the use of pneumatic bellows or strain gauge around the chest or abdomen [48, 49]. Other techniques are based on measuring the change in lung volume using spirometer [50-52]. Studies have suggested that the spirometer gives the most accurate representation of lung motion but is less tolerated by patients [45].

All of these measurements acting as surrogates for the motion of internal organs therefore make an assumption that the measured parameter represents the internal organ motion. This assumption fails to explain the fact that the organ motion is complex and predicting the motion from a single parameter (such as the motion from the chest-wall or the abdomen or lung volume from spirometer) may not entirely account for the motion trajectories of the organs of interest. The presence of hysteresis is one such example, wherein the organ position cannot be determined solely based on the respiratory amplitude, but also requires the knowledge of the phase (inspiratory or expiratory) of the respiratory cycle. Hysteresis has been observed and reported in the respiratory motions of the heart [32] and of tumors [31, 36-38]. Chi et al. studied the relationship between the external chest and abdomen markers and the motion of lung tumors using 4D CT [37] and found that for a given patient the relationship between the tumor motion and the markers varied between consecutive respiratory cycles explaining the presence of varying degrees of hysteresis. This illustrates that a prediction of tumor or organ motion solely from the abdominal or chest-wall markers would likely result in errors, minimizing the effectiveness of gating method.

A few problems associated with external markers and their assumed correlation to the internal organ motion can be mitigated with the use of data-driven gating techniques, where the information from the acquired data is used to derive a respiratory trace and avoid the need for external measurements. This method has been used with PET data [53, 54]: short time frames are used to derive a respiratory trace, from which the data are retrospectively binned in to appropriate respiratory frames. The image data from the corresponding respiratory positions are summed, as done with the external marker gating methods. The signal-to-noise ratio (SNR) of short time frames with limited counts is particularly poor and it is critical that the signal extraction methods are robust to prevent any erroneous measurements.

The question of how to best divide the data into frames from the obtained respiratory trace can be answered by two methods: one method is based on the amplitude [55-57] which divides the data over the range of overall amplitude of the motion, while the other method is based on the phase [47, 58] where the data is divided according to the time elapsed from the start of the cycle.

The variability of the breathing cycle influences the efficiency of the gating. Irregular breathing is a common occurrence and presents an additional problem to respiratory gating [59, 60]. Figure 2.22 shows the respiratory motion of the heart recorded over 5 minutes for 2 volunteers, measured using dynamic MRI scans. These traces show a large degree of variability, with variations in amplitude of motion, the period of respiratory cycle and the position of baseline. This suggests that the respiratory induced motions of organs are also variable, adding to the problems of respiratory gating.

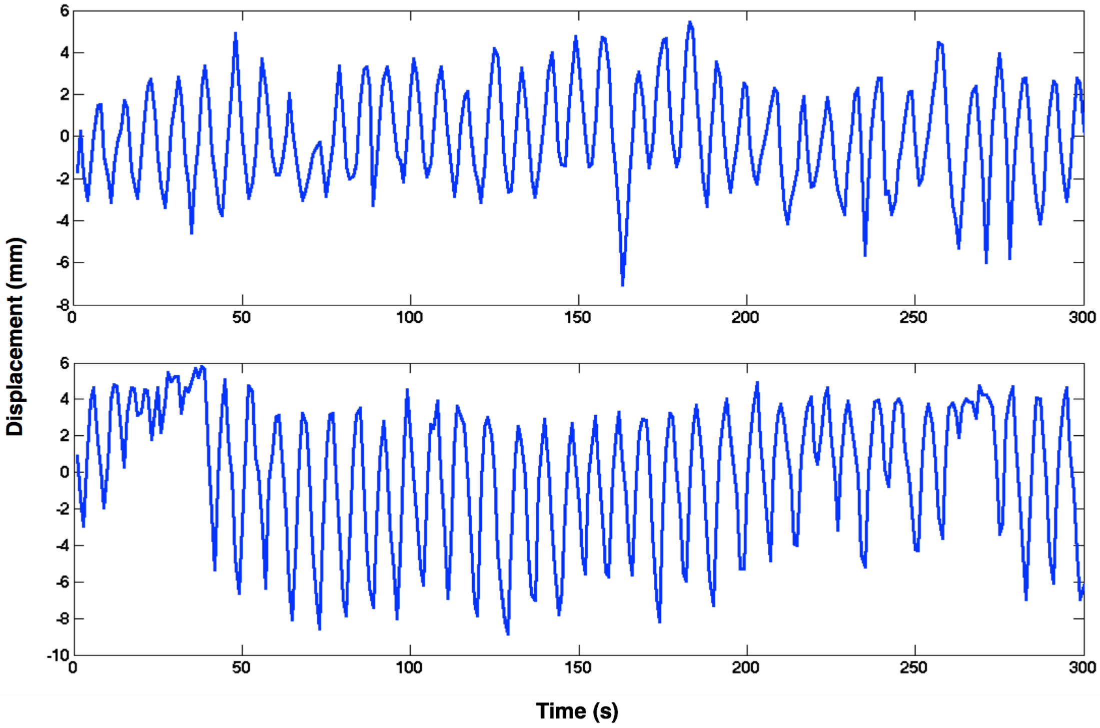

Figure 2.22 The respiratory motion of 2 volunteers, acquired over a 5 minute time period using MRI. Note the large variations in terms of the amplitude for both volunteers.

Phase based gating has been found to be more susceptible to these variations than amplitude based gating due to the fact that equivalent phases of the cycle are summed regardless of the depth of breathing [61]. On the other hand, though amplitude based gating is more robust to changes in the depth of breathing [29, 57], it does not account for hysteresis and assumes that position of the organ maintains the same position for a given lung volume. Currently SPECT and PET/CT scanners cannot perform this type of gating on the fly. The data sorting needs to be performed during post-acquisition using the list-mode data. List-mode acquisitions consists of the information associated with every detected event, such as the time of the occurrence of trigger signals that are used to synchronize the respiratory trace with the emission acquisition [62]. The emission data is then sorted into bins according to the respiratory trace. Despite the advantages of the amplitude based gating on the list-mode data, it is currently limited to the research setting and not widely used in the clinic.

The respiratory cycle variations along with hysteresis will lead to a degradation of the gating, which in turn leads to motion corruption in the gated images. This leads to blurring in addition to the blurring present from the residual motion occurring within a frame to finite length. The issues of the residual motion and the limitations of gating in the presence of irregular breathing and hysteresis should be considered. Due to residual blurring, the organs affected by motion may not have the expected appearance in either the emission or transmission scans. Use of motion-corrupted transmission images for attenuation correction may introduce additional errors into the emission data. These are some of the crucial factors motivating research into amplitude based gating and motion correction that are less susceptible to these artifacts by accounting for hysteresis and irregular breathing cycles. With the advent of multimodality imaging (simultaneous PET-MRI systems) and data-driven methods of gating and motion correction mitigates the effects of motion artifacts.

Currently, to correct for respiratory motion, the frames (projection sets) for each phase or amplitude bin are reconstructed separately, and then the sets are combined through three-dimensional (3D) registration of the heart [48, 53, 60, 63-69]. Once the 3D motion has been estimated by use of registration, a second pass through reconstruction is performed using the estimated motion for each bin such that all of the bins are reconstructed into a single set of slices [35, 56, 70-72]. The issues of residual blurring due to hysteresis and irregular depth of breathing are not addressed in the current motion correction methods and have led to investigation of alternate techniques to account for hysteresis [38, 50, 73, 74]. This is the focus of this project, where methods to account for hysteresis to minimize residual blurring are sought in order to provide robust amplitude based gating for binning list-mode data. By using the respiratory information from both the thoracic and the abdomen regions, comparable to the studies demonstrated by Fayad et al. [73] and Odille et al. [74] indicates that a better motion model is necessary to account for both hysteretic and irregular breathing patterns. For material on the current status of respiratory motion modeling, the reader is referred to an excellent recent review [75] providing more details on such modeling in medical imaging.

The Bouc-Wen model of hysteresis [76, 77], widely used in the field of smart structures and civil engineering, is capable of modeling a wide range of hysteretic cycle shapes and is described below.

2.5 Bouc-Wen model

Hysteresis is a global phenomenon that occurs in various disciplines of science and engineering areas such as electronics, mechanics, life sciences, etc. Several mathematical models have been put forward to describe the behavior of hysteretic processes [78]: the Duhem model [79], Ishlinskii hysteresis operator [80], the Preisach model [81] and the Bouc-Wen model [76, 77]. The Bouc-Wen model, due to its ease of numerical implementation and its ability to describe a broad range of hysteretic cycle shapes, is popular in mechanical and structural engineering. The Bouc-Wen model in its original form can generate stable clockwise hysteresis loops while hysteresis associated with the respiratory system is counterclockwise [32, 82]. Therefore, a modified Bouc-Wen model [83, 84] capable of describing counterclockwise hysteresis of the respiratory trace is proposed in this study to better predict the behavior of the structures influenced by hysteretic respiratory motion.

2.6 NURBS based Cardiac-Torso (NCAT) Phantom

The four dimensional (4-D) NCAT digital software phantom [85, 86] was developed to provide real-life model for human physiology and anatomy primarily to evaluate and optimize imaging systems for cardiac and respiratory motions. It is comprised of the organs of the thoracic and abdomen regions. The cardiac model was developed based upon a tagged-MRI data and three-dimensional (3D) angiogram data of a normal subject. The modeling of the remaining organs was based on the CT data. Non-Uniform Rational B-Splines (NURBS) method was used to construct and mimic real-life shaped organs that move and are distorted with respiration. The NCAT provides the user with flexibility of specifying a particular type of respiratory motion with the options of varying both the amplitude and the frequency. It also proved the user the ability to define the sizes, positions and activity levels of the organs, such as the heart, liver and spleen.

To evaluate the effect of different respiratory motion patterns in the process of imaging, the software allows the user to choose the magnitude of motion for each organ. By default, the respiratory motion of the heart is caused by both the diaphragmatic and the chest-wall motions and is in phase with both of these motions. The amplitude of the respiratory heart motion in the superior-inferior (SI) direction is matched to that of the diaphragm and in the anterior-posterior (AP) direction to that of the chest-wall. However, in the real case, the heart motion is typically of a lower magnitude than that of the diaphragm and in the presence of hysteresis slightly out of phase. To offer more real-life organ motions with improved resolution, the NCAT phantom has been updated to the “extended cardiac-torso phantom”, XCAT [87, 88].

2.7 References

[1] E. Antman, J.-P. Bassand, W. Klein, M. Ohman, J. L. Lopez Sendon, L. Rydén*, et al.*, "Myocardial infarction redefined—a consensus document of The Joint European Society of Cardiology/American College of Cardiology committee for the redefinition of myocardial infarctionThe Joint European Society of Cardiology/ American College of Cardiology Committee∗," *Journal of the American College of Cardiology,* vol. 36, pp. 959-969, 2000.

[2] A. S. Go, D. Mozaffarian, V. L. Roger, E. J. Benjamin, J. D. Berry, W. B. Borden*, et al.*, "Heart Disease and Stroke Statistics—2013 Update: A Report From the American Heart Association," *Circulation,* vol. 127, pp. e6-e245, January 1, 2013 2013.

[3] E. G. M. Depuey, E. V. Garcia, and D. S. Berman, *Cardiac SPECT imaging*: Wolters Kluwer Health, 2001.

[4] M. N. Wernick and J. N. Aarsvold, *Emission tomography: the fundamentals of PET and SPECT*: Access Online via Elsevier, 2004.

[5] M. D. Cerqueira, N. J. Weissman, V. Dilsizian, A. K. Jacobs, S. Kaul, W. K. Laskey*, et al.*, "Standardized myocardial segmentation and nomenclature for tomographic imaging of the heart. A statement for healthcare professionals from the Cardiac Imaging Committee of the Council on Clinical Cardiology of the American Heart Association," *J Nucl Cardiol,* vol. 9, pp. 240-5, Mar-Apr 2002.

[6] E. H. Botvinick, Y. Y. Zhu, W. J. O'Connell, and M. W. Dae, "A quantitative assessment of patient motion and its effect on myocardial perfusion SPECT images," *J Nucl Med,* vol. 34, pp. 303-10, Feb 1993.

[7] F. M. Prigent, M. Hyun, D. S. Berman, and A. Rozanski, "Effect of motion on thallium-201 SPECT studies: a simulation and clinical study," *J Nucl Med,* vol. 34, pp. 1845-50, Nov 1993.

[8] K. McLeish, D. L. G. Hill, D. Atkinson, J. M. Blackall, and R. Razavi, "A study of the motion and deformation of the heart due to respiration," *Medical Imaging, IEEE Transactions on,* vol. 21, pp. 1142-1150, 2002.

[9] M. DE, *Respiratory Anatomy and Physiology*: CV Mosby Company, 1988.

[10] P. H. Pretorius and M. A. King, "A study of possible causes of artifactual decreases in the left ventricular apex with SPECT cardiac perfusion imaging," *Nuclear Science, IEEE Transactions on,* vol. 46, pp. 1016-1023, 1999.

[11] K. Cho, S. Kumiata, S. Okada, and T. Kumazaki, "Development of respiratory gated myocardial SPECT system," *J Nucl Cardiol,* vol. 6, pp. 20-8, Jan-Feb 1999.

[12] B. M. W. Tsui, W. P. Segars, and D. S. Lalush, "Effects of upward creep and respiratory motion in myocardial SPECT," *Nuclear Science, IEEE Transactions on,* vol. 47, pp. 1192-1195, 2000.

[13] W. P. Segars, D. S. Lalush, and B. M. W. Tsui, "Modeling respiratory mechanics in the MCAT and spline-based MCAT phantoms," *Nuclear Science, IEEE Transactions on,* vol. 48, pp. 89-97, 2001.

[14] A. G. Pitman, V. Kalff, B. Van Every, B. Risa, L. R. Barnden, and M. J. Kelly, "Effect of Mechanically Simulated Diaphragmatic Respiratory Motion on Myocardial SPECT Processed With and Without Attenuation Correction," *Journal of Nuclear Medicine,* vol. 43, pp. 1259-1267, September 1, 2002 2002.

[15] M. E. McCord, S. L. Bacharach, R. O. Bonow, V. Dilsizian, A. Cuocolo, and N. Freedman, "Misalignment Between PET Transmission and Emission Scans: Its Effect on Myocardial Imaging," *Journal of Nuclear Medicine,* vol. 33, pp. 1209-1214, June 1, 1992 1992.

[16] I. Matsunari, G. Böning, S. I. Ziegler, I. Kosa, S. G. Nekolla, E. P. Ficaro*, et al.*, "Effects of Misalignment Between Transmission and Emission Scans on Attenuation-Corrected Cardiac SPECT," *Journal of Nuclear Medicine,* vol. 39, pp. 411-416, March 1, 1998 1998.

[17] A. Lundberg, "Kinematics of the ankle and foot. In vivo roentgen stereophotogrammetry," *Acta Orthop Scand Suppl,* vol. 233, pp. 1-24, 1989.

[18] P. C. Lauterbur, "Image formation by induced local interactions. Examples employing nuclear magnetic resonance. 1973," *Clin Orthop Relat Res,* pp. 3-6, Jul 1989.

[19] A. Kumar, D. Welti, and R. R. Ernst, "NMR Fourier zeugmatography. 1975," *J Magn Reson,* vol. 213, pp. 495-509, Dec 2011.

[20] P. Mansfield, "Multi-planar image formation using NMR spin echoes," *Journal of Physics C: Solid State Physics,* vol. 10, p. L55, 1977.

[21] E. L. Hahn, "Spin Echoes," *Physical Review,* vol. 80, pp. 580-594, 11/15/ 1950.

[22] A. N. Garroway, P. K. Grannell, and P. Mansfield, "Image formation in NMR by a selective irradiative process," *Journal of Physics C: Solid State Physics,* vol. 7, p. L457, 1974.

[23] R. L. Ehman and J. P. Felmlee, "Adaptive technique for high-definition MR imaging of moving structures," *Radiology,* vol. 173, pp. 255-63, Oct 1989.

[24] T. D. Nguyen, Y. Wang, R. Watts, and I. Mitchell, "k-Space weighted least-squares algorithm for accurate and fast motion extraction from magnetic resonance navigator echoes," *Magn Reson Med,* vol. 46, pp. 1037-40, Nov 2001.

[25] Y. Wang, R. C. Grimm, J. P. Felmlee, S. J. Riederer, and R. L. Ehman, "Algorithms for extracting motion information from navigator echoes," *Magnetic Resonance in Medicine,* vol. 36, pp. 117-123, 1996.

[26] W. P. Segars, D. S. Lalush, and B. M. W. Tsui, "A realistic spline-based dynamic heart phantom," *Nuclear Science, IEEE Transactions on,* vol. 46, pp. 503-506, 1999.

[27] P. Cluzel, T. Similowski, C. Chartrand-Lefebvre, M. Zelter, J. P. Derenne, and P. A. Grenier, "Diaphragm and chest wall: assessment of the inspiratory pump with MR imaging-preliminary observations," *Radiology,* vol. 215, pp. 574-83, May 2000.

[28] D. Ruan, J. A. Fessler, J. M. Balter, and J. J. Sonke, "Exploring breathing pattern irregularity with projection-based method," *Med Phys,* vol. 33, pp. 2491-9, Jul 2006.

[29] A. F. Abdelnour, S. A. Nehmeh, T. Pan, J. L. Humm, P. Vernon, H. Schoder*, et al.*, "Phase and amplitude binning for 4D-CT imaging," *Phys Med Biol,* vol. 52, pp. 3515-29, Jun 21 2007.

[30] S. A. Nehmeh, Y. E. Erdi, T. Pan, E. Yorke, G. S. Mageras, K. E. Rosenzweig*, et al.*, "Quantitation of respiratory motion during 4D-PET/CT acquisition," *Medical Physics,* vol. 31, pp. 1333-1338, Jun 2004.

[31] Y. Seppenwoolde, H. Shirato, K. Kitamura, S. Shimizu, M. van Herk, J. V. Lebesque*, et al.*, "Precise and real-time measurement of 3D tumor motion in lung due to breathing and heartbeat, measured during radiotherapy," *Int J Radiat Oncol Biol Phys,* vol. 53, pp. 822-34, Jul 15 2002.

[32] K. Nehrke, P. Bornert, D. Manke, and J. C. Bock, "Free-breathing cardiac MR imaging: Study of implications of respiratory motion-initial results," *Radiology,* vol. 220, pp. 810-815, Sep 2001.

[33] G. Shechter, C. Ozturk, J. R. Resar, and E. R. McVeigh, "Respiratory motion of the heart from free breathing coronary angiograms," *IEEE Trans Med Imaging,* vol. 23, pp. 1046-56, Aug 2004.

[34] J. Dey, P. Tinsu, M. Smyczynski, H. Pretorias, D. Choi, and M. A. King, "Investigation of respiration motion of the heart based on semi-automated segmentation and modeling of respiratory-gated CT data," in *Nuclear Science Symposium Conference Record, 2005 IEEE*, 2005, pp. 2557-2560.

[35] L. Livieratos, L. Stegger, P. M. Bloomfield, K. Schafers, D. L. Bailey, and P. G. Camici, "Rigid-body transformation of list-mode projection data for respiratory motion correction in cardiac PET," *Phys Med Biol,* vol. 50, pp. 3313-22, Jul 21 2005.

[36] J. M. Blackall, S. Ahmad, M. E. Miquel, J. R. McClelland, D. B. Landau, and D. J. Hawkes, "MRI-based measurements of respiratory motion variability and assessment of imaging strategies for radiotherapy planning," *Physics in Medicine and Biology,* vol. 51, pp. 4147-4169, Sep 7 2006.

[37] P. C. Chi, P. Balter, D. Luo, R. Mohan, and T. Pan, "Relation of external surface to internal tumor motion studied with cine CT," *Medical physics,* vol. 33, pp. 3116-23, Sep 2006.

[38] D. Ruan, J. A. Fessler, J. M. Balter, R. I. Berbeco, S. Nishioka, and H. Shirato, "Inference of hysteretic respiratory tumor motion from external surrogates: a state augmentation approach," *Physics in Medicine and Biology,* vol. 53, pp. 2923-2936, Jun 7 2008.

[39] V. Dilsizian, S. Bacharach, R. Beanlands, S. Bergmann, D. Delbeke, R. Gropler*, et al.*, "PET myocardial perfusion and metabolism clinical imaging," *Journal of Nuclear Cardiology,* vol. 16, pp. 651-651, 2009/08/01 2009.

[40] T. A. Holly, B. G. Abbott, M. Al-Mallah, D. A. Calnon, M. C. Cohen, F. P. DiFilippo*, et al.*, "Single photon-emission computed tomography," *J Nucl Cardiol,* vol. 17, pp. 941-73, Oct 2010.

[41] M. M. Ter-Pogossian, S. R. Bergmann, and B. E. Sobel, "Influence of cardiac and respiratory motion on tomographic reconstructions of the heart: implications for quantitative nuclear cardiology," *J Comput Assist Tomogr,* vol. 6, pp. 1148-55, Dec 1982.

[42] J. A. Nye, F. Esteves, and J. R. Votaw, "Minimizing artifacts resulting from respiratory and cardiac motion by optimization of the transmission scan in cardiac PET/CT," *Med Phys,* vol. 34, pp. 1901-6, Jun 2007.

[43] R. Lautamaki, T. L. Brown, J. Merrill, and F. M. Bengel, "CT-based attenuation correction in (82)Rb-myocardial perfusion PET-CT: incidence of misalignment and effect on regional tracer distribution," *Eur J Nucl Med Mol Imaging,* vol. 35, pp. 305-10, Feb 2008.

[44] K. L. Gould, T. Pan, C. Loghin, N. P. Johnson, A. Guha, and S. Sdringola, "Frequent Diagnostic Errors in Cardiac PET/CT Due to Misregistration of CT Attenuation and Emission PET Images: A Definitive Analysis of Causes, Consequences, and Corrections," *Journal of Nuclear Medicine,* vol. 48, pp. 1112-1121, July 1, 2007 2007.

[45] S. A. Nehmeh and Y. E. Erdi, "Respiratory motion in positron emission tomography/computed tomography: a review," *Semin Nucl Med,* vol. 38, pp. 167-76, May 2008.

[46] S. A. Nehmeh, Y. E. Erdi, C. C. Ling, K. E. Rosenzweig, H. Schoder, S. M. Larson*, et al.*, "Effect of respiratory gating on quantifying PET images of lung cancer," *J Nucl Med,* vol. 43, pp. 876-81, Jul 2002.

[47] S. S. Vedam, V. R. Kini, P. J. Keall, V. Ramakrishnan, H. Mostafavi, and R. Mohan, "Quantifying the predictability of diaphragm motion during respiration with a noninvasive external marker," *Med Phys,* vol. 30, pp. 505-13, Apr 2003.

[48] G. J. Klein, B. W. Reutter, H. Ho, J. H. Reed, and R. H. Huesman, "Real-time system for respiratory-cardiac gating in positron tomography," in *Nuclear Science Symposium, 1997. IEEE*, 1997, pp. 1284-1287 vol.2.

[49] H. D. Kubo and B. C. Hill, "Respiration gated radiotherapy treatment: a technical study," *Phys Med Biol,* vol. 41, pp. 83-91, Jan 1996.

[50] D. A. Low, P. J. Parikh, W. Lu, J. F. Dempsey, S. H. Wahab, J. P. Hubenschmidt*, et al.*, "Novel breathing motion model for radiotherapy," *International Journal of Radiation Oncology Biology Physics,* vol. 63, pp. 921-9, Nov 1 2005.

[51] J. Hanley, M. M. Debois, D. Mah, G. S. Mageras, A. Raben, K. Rosenzweig*, et al.*, "Deep inspiration breath-hold technique for lung tumors: the potential value of target immobilization and reduced lung density in dose escalation," *Int J Radiat Oncol Biol Phys,* vol. 45, pp. 603-11, Oct 1 1999.

[52] B. W. Reutter, G. J. Klein, K. M. Brennan, and R. H. Huesman, "Acquisition and automated 3-D segmentation of respiratory/cardiac-gated PET transmission

images," *IEEE Nuclear Science Symposium conference record (1997),* vol. 2, pp. 1357-1361, 1996.

[53] G. J. Klein, R. W. Reutter, and R. H. Huesman, "Four-dimensional affine registration models for respiratory-gated PET," *Nuclear Science, IEEE Transactions on,* vol. 48, pp. 756-760, 2001.

[54] P. J. Schleyer, M. J. O'Doherty, S. F. Barrington, and P. K. Marsden, "Retrospective data-driven respiratory gating for PET/CT," *Phys Med Biol,* vol. 54, pp. 1935-50, Apr 7 2009.

[55] D. A. Low, M. Nystrom, E. Kalinin, P. Parikh, J. F. Dempsey, J. D. Bradley*, et al.*, "A method for the reconstruction of four-dimensional synchronized CT scans acquired during free breathing," *Medical physics (Lancaster),* vol. 30, p. 1254, 2003.

[56] W. Lu, P. J. Parikh, J. P. Hubenschmidt, J. D. Bradley, and D. A. Low, "A comparison between amplitude sorting and phase-angle sorting using external respiratory measurement for 4D CT," *Med Phys,* vol. 33, pp. 2964-74, Aug 2006.

[57] M. Dawood, F. Buther, N. Lang, O. Schober, and K. P. Schafers, "Respiratory gating in positron emission tomography: A quantitative comparison of different gating schemes," *Medical Physics,* vol. 34, pp. 3067-3076, 07/00/ 2007.

[58] P. J. Keall, G. Starkschall, H. Shukla, K. M. Forster, V. Ortiz, C. W. Stevens*, et al.*, "Acquiring 4D thoracic CT scans using a multislice helical method," *Physics in Medicine and Biology,* vol. 49, p. 2053, 2004.

[59] R. I. Berbeco, S. Nishioka, H. Shirato, G. T. Chen, and S. B. Jiang, "Residual motion of lung tumours in gated radiotherapy with external respiratory surrogates," *Phys Med Biol,* vol. 50, pp. 3655-67, Aug 21 2005.

[60] J. Dey, W. P. Segars, P. H. Pretorius, R. P. Walvick, P. P. Bruyant, S. Dahlberg*, et al.*, "Estimation and correction of cardiac respiratory motion in SPECT in the presence of limited-angle effects due to irregular respiration," *Medical Physics,* vol. 37, pp. 6453-6465, Dec 2010.

[61] E. Rietzel, T. Pan, and G. T. Chen, "Four-dimensional computed tomography: image formation and clinical protocol," *Med Phys,* vol. 32, pp. 874-89, Apr 2005.

[62] P. P. Bruyant, C. Cheze Le Rest, A. Turzo, P. Jarritt, K. Carson, and D. Visvikis, "A method for synchronizing an external respiratory signal with a list-mode PET acquisition," *Med Phys,* vol. 34, pp. 4472-5, Nov 2007.

[63] L. Boucher, S. Rodrigue, R. Lecomte, and F. Benard, "Respiratory gating for 3-dimensional PET of the thorax: Feasibility and initial results," *Journal of Nuclear Medicine,* vol. 45, pp. 214-219, Feb 2004.

[64] M. W. Groch, D. A. Turner, and W. D. Erwin, "Respiratory gating in magnetic resonance imaging: improved image quality over non-gated images for equal scan time," *Clin Imaging,* vol. 15, pp. 196-201, Jul-Sep 1991.

[65] H. D. Kubo, P. M. Len, S.-i. Minohara, and H. Mostafavi, "Breathing-synchronized radiotherapy program at the University of California Davis Cancer Center," *Medical Physics,* vol. 27, pp. 346-353, 2000.

[66] M. Mori, K. Murata, M. Takahashi, K. Shimoyama, T. Ota, R. Morita*, et al.*, "Accurate contiguous sections without breath-holding on chest CT: value of respiratory gating and ultrafast CT," *American Journal of Roentgenology,* vol. 162, pp. 1057-1062, 1994/05/01 1994.

[67] S. A. Nehmeh, Y. E. Erdi, C. C. Ling, K. E. Rosenzweig, O. D. Squire, L. E. Braban*, et al.*, "Effect of respiratory gating on reducing lung motion artifacts in PET imaging of lung cancer," *Med Phys,* vol. 29, pp. 366-71, Mar 2002.

[68] B. E. Oppenheim, "A Method Using a Digital Computer for Reducing Respiratory Artifact on Liver Scans Made with a Camera," *Journal of Nuclear Medicine,* vol. 12, pp. 625-628, September 1, 1971 1971.

[69] D. A. Turner, E. W. Fordham, A. Ali, P. D. Rubin, R. C. Muerhrcke, B. E. Oppenheim*, et al.*, "Motion corrected hepatic scintigraphy: an objective clinical evaluation," *J Nucl Med,* vol. 19, pp. 142-8, Feb 1978.

[70] P. P. Bruyant, M. A. King, and P. H. Pretorius, "Correction of the respiratory motion of the heart by tracking of the center of mass of thresholded projections: a simulation study using the dynamic MCAT phantom," *Nuclear Science, IEEE Transactions on,* vol. 49, pp. 2159-2166, 2002.

[71] G. Kovalski, O. Israel, Z. Keidar, A. Frenkel, J. Sachs, and H. Azhari, "Correction of heart motion due to respiration in clinical myocardial perfusion SPECT scans using respiratory gating," *Journal of Nuclear Medicine,* vol. 48, pp. 630-636, Apr 2007.

[72] F. Lamare, T. Cresson, J. Savean, C. C. L. Rest, A. J. Reader, and D. Visvikis, "Respiratory motion correction for PET oncology applications using affine transformation of list mode data," *Physics in Medicine and Biology,* vol. 52, p. 121, 2007.

[73] I. Burger and E. M. Meintjes, "Elliptical subject-specific model of respiratory motion for cardiac MRI," *Magnetic Resonance in Medicine,* vol. 70, pp. 722-731, Sep 2013.

[74] D. Ruan, J. A. Fessler, and J. M. Balter, "Mean position tracking of respiratory motion," *Med Phys,* vol. 35, pp. 782-92, Feb 2008.

[75] H. Fayad, T. Pan, O. Pradier, and D. Visvikis, "Patient specific respiratory motion modeling using a 3D patient's external surface," *Medical Physics,* vol. 39, pp. 3386-3395, 06/00/ 2012.

[76] F. Odille, N. Cindea, D. Mandry, C. Pasquier, P. A. Vuissoz, and J. Felblinger, "Generalized MRI reconstruction including elastic physiological motion and coil sensitivity encoding," *Magn Reson Med,* vol. 59, pp. 1401-11, Jun 2008.

[77] J. R. McClelland, D. J. Hawkes, T. Schaeffter, and A. P. King, "Respiratory motion models: a review," *Med Image Anal,* vol. 17, pp. 19-42, Jan 2013.

[78] R. Bouc, "Modèle mathématique d’hystérésis," *Acustica,* vol. 24, pp. 16-25, 1971.

[79] Y.-K. Wen, "Method for random vibration of hysteretic systems," *Journal of the Engineering Mechanics Division,* vol. 102, pp. 249-263, 1976.

[80] A. Visintin, *Differential Models of Hysteresis* vol. 111. Berlin: Springer-Verlag, 1994.

[81] P. Duhem, "Die dauernden aenderungen und die thermodynamik," *I. Z. Phys. Chem.,* 1897.

[82] M. K. A. Pokrovskii, "Systems with hysteresis," *Moscow, Nauka,* 1983.

[83] F. Preisach, "Über die magnetische Nachwirkung," *Zeitschrift für physik,* vol. 94, pp. 277-302, 1935.

[84] M. v. Siebenthal, "Analysis and modelling of respiratory liver motion using 4DMRI," Ph.D, Eidgenössische Technische Hochschule ETH Zürich, Konstanz, 2008.

[85] K. R. Qin and X. A. Cheng, "Hysteresis modeling for calcium-mediated ciliary beat frequency in airway epithelial cells," *Mathematical Biosciences,* vol. 229, pp. 101-108, Jan 2011.

[86] J. Hu, K. R. Qin, C. Xiang, and T. H. Lee, "Modeling of Hysteresis in Gene Regulatory Networks," *Bulletin of Mathematical Biology,* vol. 74, pp. 1727-1753, Aug 2012.

[87] W. P. Segars, B. Tsui, D. Lalush, E. Frey, M. King, and D. Manocha, "Development and application of the new dynamic Nurbs-based Cardiac-Torso (NCAT) phantom," 2001.

[88] W. P. Segars, D. S. Lalush, and B. M. Tsui, "A realistic spline-based dynamic heart phantom," *Nuclear Science, IEEE Transactions on,* vol. 46, pp. 503-506, 1999.

[89] W. Segars, M. Mahesh, T. Beck, E. Frey, and B. Tsui, "Realistic CT simulation using the 4D XCAT phantom," *Medical physics,* vol. 35, p. 3800, 2008.

[90] W. P. Segars, B. M. Tsui, E. Frey, and E. Fishman, "Extension of the 4D NCAT phantom to dynamic x-ray CT simulation," in *Nuclear Science Symposium Conference Record, 2003 IEEE*, 2003, pp. 3195-3199.

Chapter 3 - MRI Investigation of the Linkage between Respiratory Motion of the Heart and Markers on Patient's Abdomen and Chest: Implications for Respiratory Amplitude Binning List-Mode PET and SPECT Studies

Paul Dasari[a,b], Karen Johnson [b], Joyoni Dey [b], Clifford Lindsay [c], Mohammed S. Shazeeb[a,b], Joyeeta Mitra Mukherjee[b], Shaokuan Zheng[b], and Michael A. King[b]

[a] Department of Radiology, University of Massachusetts Medical School, Worcester
[b] Department of Biomedical Engineering, Worcester Polytechnic Institute, Worcester
[c] Department of Computer Science, Worcester Polytechnic Institute, Worcester

The material presented in Chapter 3 is based on a paper by *Paul Dasari, Karen Johnson, Joyoni Dey, Clifford Lindsay, Mohammed S. Shazeeb, Joyeeta Mitra Mukherjee, Shaokuan Zheng, and Michael A. King*, "MRI Investigation of the Linkage Between Respiratory Motion of the Heart and Markers on Patient's Abdomen and Chest: Implications for Respiratory Amplitude Binning List-Mode PET and SPECT Studies", © 2014 IEEE; reprinted, with permission, from (IEEE Transactions on Nuclear Science, vol. 61, pp. 192-201, 2014)

Abstract— Respiratory motion of the heart impacts the diagnostic accuracy of myocardial-perfusion emission-imaging studies. Amplitude binning has come to be the method of choice for binning list-mode based acquisitions for correction of respiratory motion in PET and SPECT. In some subjects respiratory motion exhibits hysteretic behavior similar to damped non-linear cyclic systems. The detection and correction of hysteresis between the signals from surface movement of the patient's body used in binning and the motion of the heart within the chest remains an open area for investigation. This study reports our investigation in nine volunteers of the combined MRI tracking of the internal respiratory motion of the heart using Navigators with stereo-tracking of markers on the volunteer's chest and abdomen by a visual-tracking system (VTS). The respiratory motion signals from the internal organs and the external markers were evaluated for hysteretic behavior analyzing the temporal correspondence of the signals. In general, a strong, positive correlation between the external marker motion (AP direction) and the internal heart motion (SI direction) during respiration was observed. The average ± standard deviation in the Spearman's ranked correlation coefficient (ρ) over the nine volunteer studied was 0.92 ± 0.1 between the external abdomen marker and the internal heart, and 0.87 ± 0.2 between the external chest marker and the internal heart. However despite the good correlation on average for the nine volunteers, in three studies a poor correlation was observed due to hysteretic behavior between inspiration and expiration for either the chest marker and the internal motion of the heart, or the abdominal marker and the motion of the heart. In

all cases we observed a good correlation of at least either the abdomen or the chest with the heart. Based on this result, we propose the use of marker motion from both the chest and abdomen regions when estimating the internal heart motion to detect and address hysteresis when binning list-mode emission data.

3.1 Introduction

Respiratory motion and other body motions in cardiac-perfusion PET and SPECT imaging are inevitable due to the long scan duration (typically 3-15 mins) [1, 2]. The motion during acquisition result in blurring and mismatch between emission and transmission scans used in estimating attenuation maps. These in turn degrade the accuracy of the diagnostic imaging.

Motion can be reduced by using some respirator-surrogate signal to select for acquisition just the data acquired near end-expiration, when one typically pauses momentarily [3]. However, this can trade an increase in noise due to a reduction in counts acquired or require a prolongation of acquisition for improved resolution due to less motion being present. With use of list-mode acquisition, all the counts can be acquired and combined into motion states (bins) post-acquisition based on a simultaneously acquired signal related to the extent of respiration. Use of the amplitude of this signal has been shown to result in more accurate and consistent binning than use of the phase for correction of respiratory motion [4-6]. It has been demonstrated that the respiratory motion of the diaphragm is correlated with the anterior / posterior motion of the abdomen [7]. Thus, the internal motion of the diaphragm can be predicted from an external respiratory signal. The respiratory motion of the heart results primarily from the motion of the diaphragm in the superior-inferior (SI) direction and rocking of the ribs causing anterior-posterior (AP) motion [8, 9]. However, the relationship between the amplitude of the external signal and the actual position of internal structures can be complex.

A number of studies have been performed using MRI and CT to investigate and model the respiratory motion of various anatomical regions. The most common regions investigated have been the lung [10-14], diaphragm [7, 15], and heart [9, 16, 17]. For example, Nehrke *et al.* [9] reported on the presence of hysteresis between the displacements of the heart and the diaphragm during free breathing using a multi-navigator echo technique in MRI.

The aim of this study was to follow-up on the investigations of Nehrke *et al.* [9] with the goal of better understanding the relationship between internal motion of the heart and external motion of surrogates during respiratory motion using MRI and a visual-tracking system (VTS) [18], respectively. This was done by motion-tracking external markers on the abdomen and chest simultaneously with MRI tracking of respiratory motion the heart, chest, and dome of the liver. An analysis of the correlation between the external and internal motion of these locations was then employed to further explore the relationship between external signals and motion of the heart.

3.2 Materials and Methods

The VTS employed in these investigations allows near-infrared tracking of multiple markers within the 3-dimensional imaging volume of the MRI [18]. The VTS is comprised of the following components: the infrared cameras, the controlling hardware module, and the software to analyze and present the data. Three cameras of the VTS system were mounted on the wall of the MRI room adjusted such that the center of the volume to be tracked is at the iso-center of the MRI. Before each experimental session the VTS system is calibrated for stereo motion-tracking and tested for minimal RF interference with the MRI as discussed in [19]. Stereo imaging of the external retro-reflective markers on the thoracic-abdominal regions of volunteers by VTS was performed at 30 frames per second throughout MRI imaging. Synchronization between the MR scanner and VTS system was established by using a trigger signal from the MR scanner at the beginning of acquisition to start motion capture by the VTS system.

Nine healthy volunteers without counter-indications to MRI were studied in this investigation. One of the volunteers was investigated on two different occasions. The participation of volunteers was with IRB approval and informed consent. The volunteers were prepared for VTS imaging by wrapping bands with 7 markers about their chest and abdomen as illustrated in Figure 3.1(a). The markers were 2 cm diameter retro-reflectively coated hollow spheres filled with copper sulfate solution. The marker positions were those employed clinically for robust motion tracking and correction in our clinic [18]. They were derived over several years of clinical usage. During imaging the volunteers were positioned supine on the table of the MRI (Figure 3.1(b)). Their hands were over their heads on the same support as employed during cardiac SPECT imaging in our clinic, and their feet faced the VTS. They were instructed to breathe slowly and regularly over the approximately 5-minute period during which MRI and motion-tracking were performed.

MRI was performed using a Philips Healthcare ACHIEVA 3.0-T whole body MR scanner. The MR software provided for acquisition by three independent pencil-beam navigator radio-frequency pulses (navigators)[20]. These could be freely placed in space at any desired location and angle as guided by patient anatomy portrayed in Survey slices acquired at the start of each imaging session. Read-out gradients in the direction of the pencil-beams acquire the navigator echo signals. The Fourier transform of the signal produces the projection of the magnetization in the motion direction (read-out direction) on to the navigator profile. This is displayed as an M mode image (Figure. 3.2). Real-time displacement of the anatomic region along the direction of the pencil-beam was determined by performing cross-correlational analysis between the current navigator profile and the previous reference profile [21].

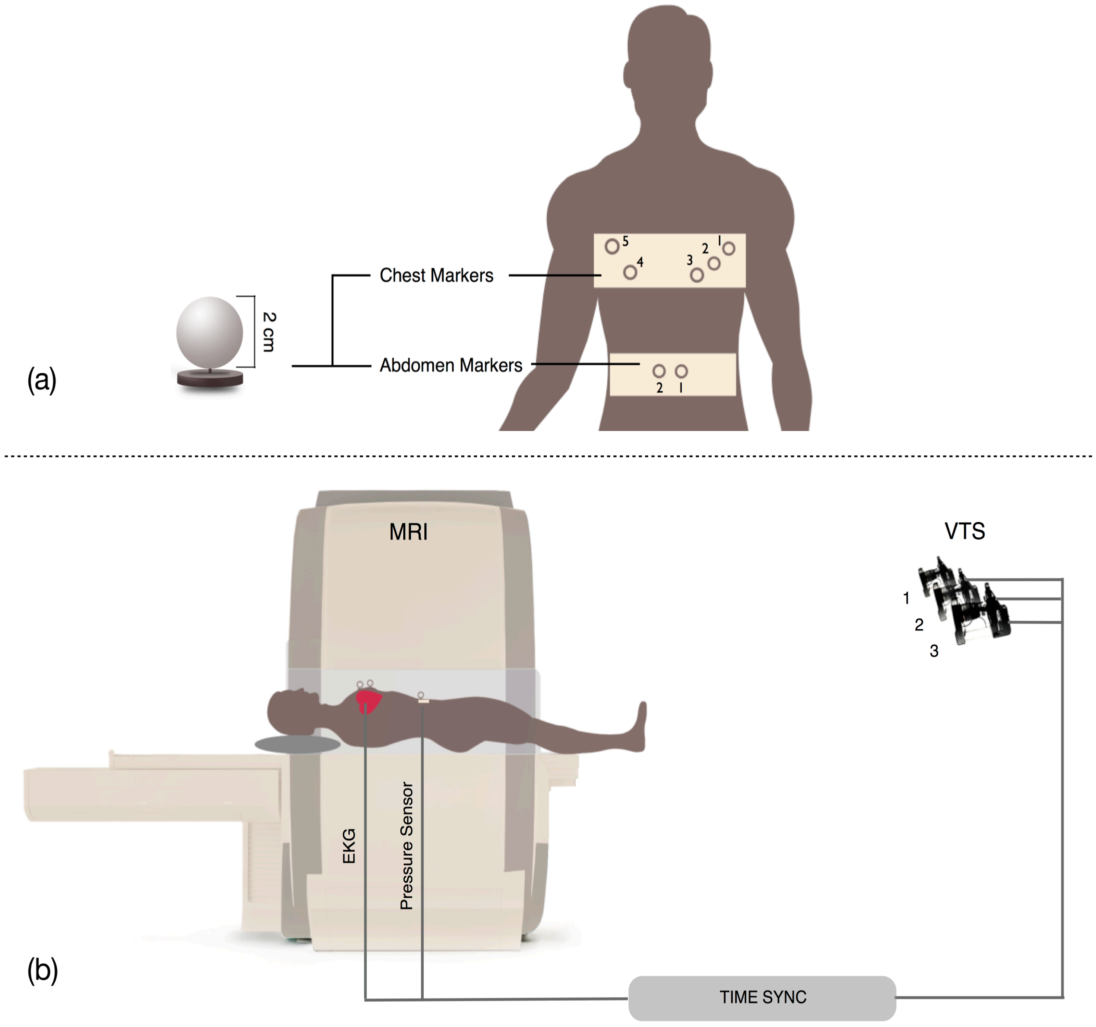

Figure 3.1 (a) Layout of 7 external marker positions on the chest and abdomen of subjects. (b) Illustration of a subject undergoing imaging positioned in supine and feet-first orientation in the MR scanner with 3 cameras of the VTS employed for tracking external marker motion. The MR scanner and the VTS are temporally synchronized by having a signal from the MRI trigger the start of motion tracking. ECG and respiratory information from the pressure sensor is acquired simultaneously during MRI acquisition.

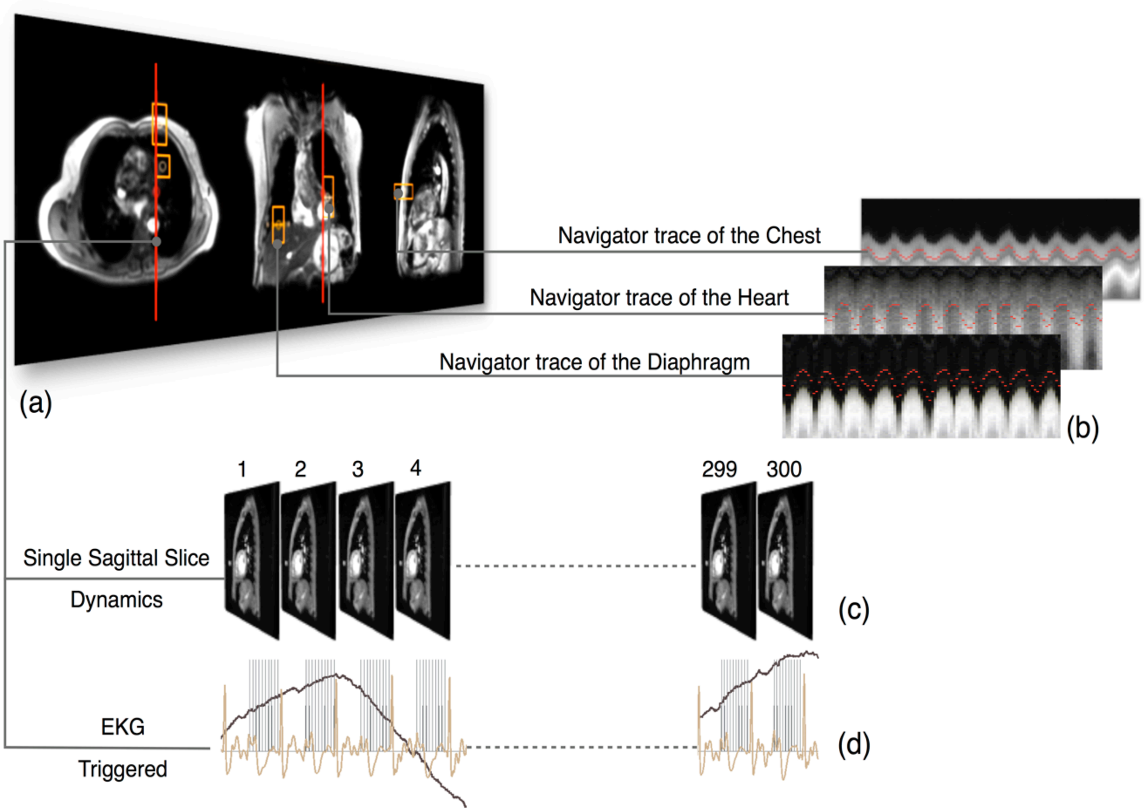

Figure 3.2 **(a) Illustrated is the positioning of navigator beams (shown as boxes) on the dome of the right hemi-diaphragm, the superior wall of the left ventricle, and the chest wall. The vertical lines in the transaxial and the coronal slices indicate the position of sagittal slices acquired along with the navigator signals. (b) Shown is example output from the 3 navigator beams as plots of the 1D gray-scale information perpendicular to each body interface versus time. These portray respiratory motion of the chest wall, heart, and diaphragm. (c) Illustrated are the 300 dynamic sagittal slices acquired when the heart was at mid-diastole. (d) Shown at the bottom along with portions of the EKG signal is the signal from the pressure sensor about the abdomen of the volunteers.**

Using Survey slices of the volunteer for guidance the three navigator windows were positioned at the selected locations of the volunteers as illustrated in Figure 3.2. Shown there are transverse, coronal and sagittal slices with the location of one or two of the three windows superimposed on each slice. The first of the navigator windows was positioned on the superior left-ventricular wall/lung boundary. As illustrated in the

Figure 3.2, this provided tracking of the ventricular wall in the SI direction, which is the direction of the largest component of cardiac respiratory motion [8, 9]. The second navigator window was on the dome of the right diaphragm. It too was positioned to track the SI motion of this structure as a relationship between diaphragm motion and the SI motion of the heart has been well established [8, 9]. Also it has been shown that there is an excellent correlation between the motion of the diaphragm and that of an external surrogate [7]. Thus the motion obtained from this navigator was employed to validate the AP motion of the abdominal markers as determined by the VTS. The third navigator window was positioned on the anterior wall of the chest to track its AP motion. The purpose of this navigator was to validate the AP motion determined from the chest markers of the VTS. The location of the tissue interfaces in these navigator beams were stored in real-time in list format in the scanner software for further analysis.

In addition to this multi-navigator sequence, dynamic acquisition of 300 single sagittal slices through the left ventricle (LV) of the heart was acquired to provide an independent measure from the navigator methodology of the respiratory motion of the heart.

MRI was performed during continuous breathing using the ECG-triggered single shot, 2D Fast-Field-Echo (Gradient Echo) sequence, with TR/TE = 5.5/2.1 ms, 128 x128 image matrix, and a 250 ms acquisition window at mid-diastole. The MRI acquisitions also included recording the signal from a bellows (pressure sensor) on the volunteer's abdomen and the EKG.

The signal for the location of the tissue interface recorded from each of the internal navigators and the vertical motion of the external markers were separated into inspiration and expiration phases based on peak detection. Selected pair-wise comparisons of respiratory signals from thoracic and abdomen regions were plotted against each other as a function of time to visually look for spatial and temporal correlations respectively between the signals. Statistically the signals were checked for correlations through calculation of parametric (linear) and non-parametric (ranked) measures of correlation. A Pearson product-moment correlation coefficient (r) [22] was computed to assess the strength of a linear association in the relationship between amount of displacement of the chest and abdominal markers, and of the heart and the diaphragm navigators. The Spearman rank-order correlation coefficient (ρ) [23] was computed as a non-parametric measure of the strength and direction of association between the external AP motion of the markers and the internal SI motion of the heart. The chest wall navigator was used along with the external VTS marker to study the correlation strength between the two modalities by computing Spearman rank-order correlation coefficient (ρ).

The MRI sagittal slices from the dynamic acquisitions were used in determining the extent of heart motion in terms of SI translation, AP translation, and rotation about the lateral axis using semi-automatic segmentation and registration [24]. This was done by using a 2-D semi-automated segmentation algorithm that segments the heart in the dynamic MRI datasets for estimating the respiratory motion of the heart. The segmented first dynamic slice was used in 3 degree-of-freedom (DOF) affine registration to estimate the respiratory motion relative to it for each subsequent slice. The translation motion of the heart in the SI direction obtained from the registration algorithm was compared against that of the heart navigator to validate these measurements. The VTS marker data was re-sampled to match the sampling rate of the heart navigator in order to perform correlation analysis between the external markers and the internal motion of the heart.

The respiratory signal from the bellows on the volunteer's abdomen was recorded but was not used in this study. All data analysis was performed in MATLAB (R2011b, Mathworks, Natick, MA).

3.3 Results

Showing all the results from our nine volunteers is prohibited by the amount of space that would be required. Thus we will show the results of selected example volunteer studies herein. Each volunteer was assigned a number for the purpose of this paper and this volunteer number will be provided when results are given.

The VTS chest markers and the chest wall navigator showed a strong, positive correlation with an average ± standard deviation of 0.95 ± 0.02 for nine volunteers. The heart motion obtained from the navigators and the slices through registration of the segmented heart also showed a strong, positive correlation with an average ± standard deviation of 0.96 ± 0.02 for nine volunteers. Thus we were able to validate through the comparison of these two independently derived measures the usage of the Navigator signal for tracking the external motion of the chest wall and for usage in tracking the SI motion of the superior wall of the LV internally. Herein we will use the Navigator measured internal motion of the heart and the VTS externally measured motion of chest as our comparisons of tracked motions.

Example results of the data from external markers and internal navigators for Volunteer 3 are provided in Figure 3.3. Notice the strong similarity of motion between the five chest markers and between the two abdomen markers for this volunteer. This trend was seen for all nine volunteers as exemplified by the strong pair-wise correlation over all-pairs of comparison between the motions of the five chest markers (0.97 ± 0.02) and the two abdomen markers (0.98 ± 0.01). This implies that any of the chest markers or either of the abdomen markers could be used for comparison to the navigator measured internal motions. This result is further illustrated in Figure 3.4, which shows plots of the individual chest and abdomen Spearman ranked correlations of the motion of individual external markers with the navigator internal heart motion for nine volunteers. Notice that the extent of external to internal agreement does vary with volunteers, but is quite similar between markers for a given volunteer. Thus we will show the results for marker 3 on the chest and marker 1 on the abdomen (seen Figure 3.1(a) for marker location) in the rest of our results presented herein.

Examples of the agreement found between VTS determined AP displacements of the external chest and abdomen markers with the internal SI respiratory motion of the heart superior LV wall as determined by the navigator for 3 volunteers are shown in Figure 3.5. The Spearman ranked correlation coefficients between the internal heart motion and the VTS chest and abdomen markers are also given to provide a quantitative measure of the correlation in the shapes (but not actual magnitudes) of the motions. The plots of Figure 3.5(a) visually demonstrate a well-defined temporal correlation between the internal and the external motions despite the irregularity in this volunteer's respiration. The visual impression of good agreement was supported by the correlation coefficients obtained for this study.

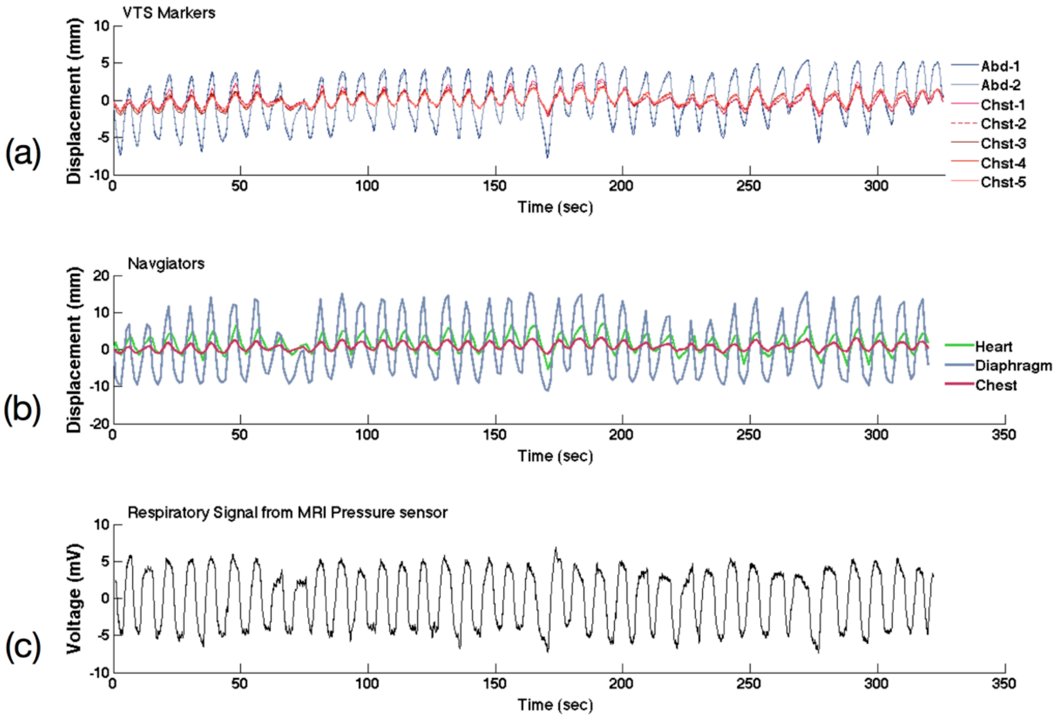

Figure 3.3 (a) Shown is the plot of the displacements of the external chest and abdomen markers as a function of time for about 5 minutes as measured by the VTS for volunteer 3. (b) Plotted are the displacements of the internal heart, diaphragm and chest wall respiratory motions obtained by the respective navigator as a function of time. (c) Plot of the respiratory pressure sensor data during MR acquisition. The plots demonstrate the well-defined spatial and temporal correlation between the internal and the external motion for this subject.

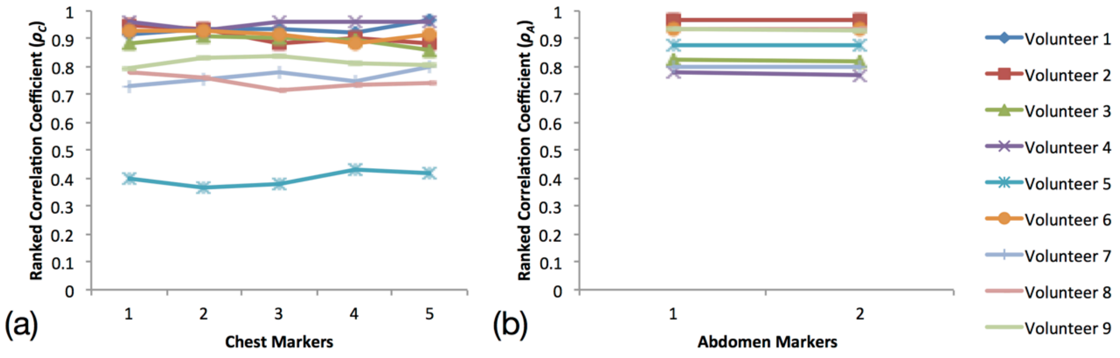

Figure 3.4 Shown are the Spearman ranked correlation coefficients between the MRI Navigator heart motion and the VTS (a) chest and (b) abdomen markers versus marker number for 5 volunteers.

In general over the nine volunteers, a strong, positive correlation between the external marker motion (AP direction) and the internal heart motion (SI direction) during expiration and inspiration phases was observed. The average ± standard deviation in the Spearman's ranked correlation coefficient (ρ) over the nine volunteer studies was 0.92 ± 0.1 between the external abdomen marker and the internal heart, and 0.87 ± 0.2 between the external chest marker and the internal heart. Though generally good, not all studies showed a strong correlation to both abdomen and chest markers. This is illustrated in Figure 5 (b), which shows the time series plot for a volunteer with moderate agreement (ρ = 0.78) between the abdomen marker and the heart, and a strong correlation between the chest marker and the heart (ρ = 0.96). In Figure 5 (c) is shown an example of a poor correlation (ρ = 0.38) between the chest marker and the heart, and a strong agreement between the abdomen and the heart ρ = 0.88). Thus we have observed either the chest or the abdomen marker signals to not correlate strongly with the motion of the heart; however, for the limited number of volunteers in this study, we have not encountered a case where both the chest markers and the abdomen markers were poorly correlated with the heart motion.

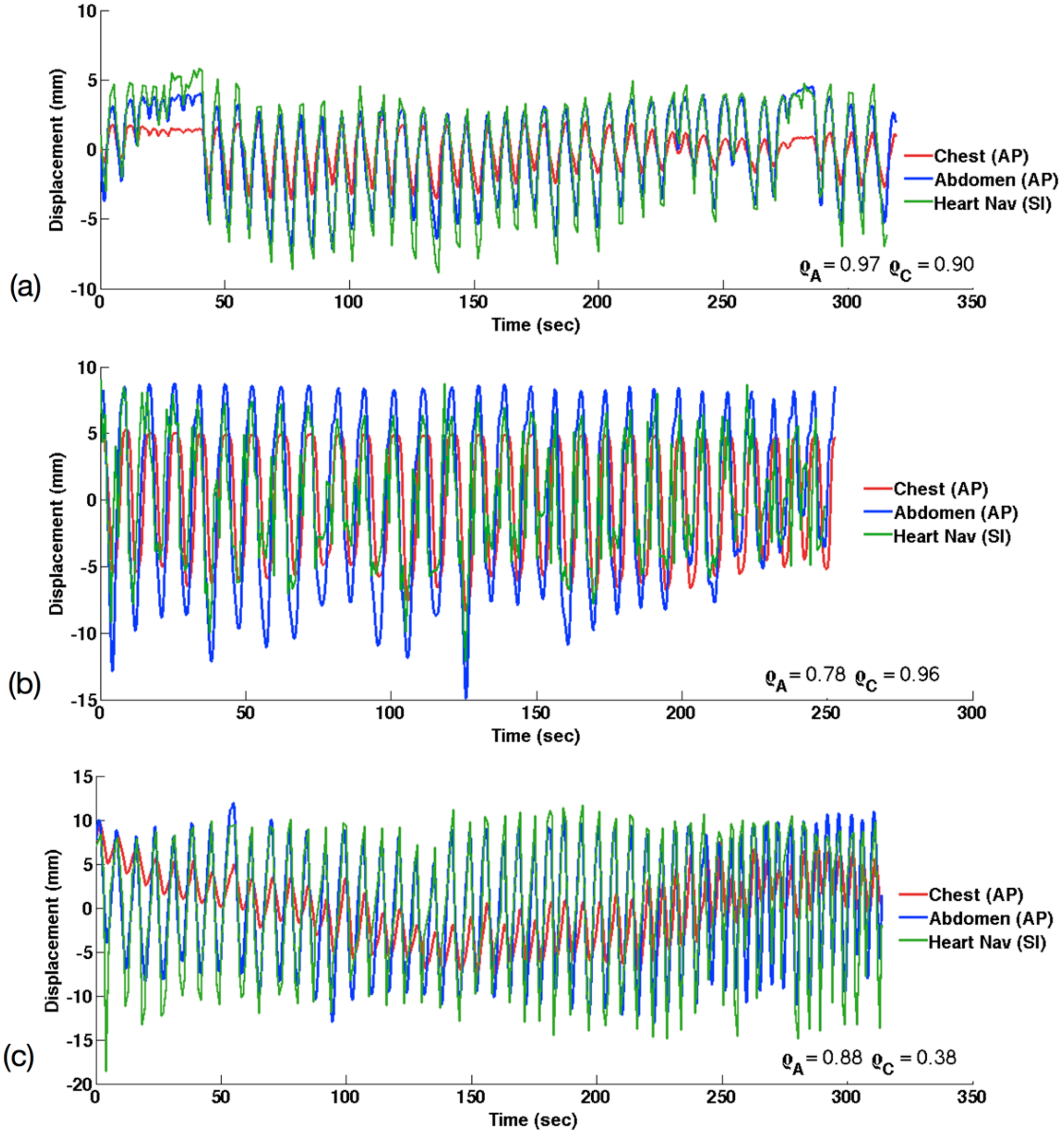

Figure 3.5 The time series plots for Volunteers 2 (a), 4 (b) and 5 (c) show the VTS determined AP displacements of selected external chest and abdomen markers as a function of time during MRI acquisition. Also shown is the internal SI respiratory motion of the heart superior LV wall as determined by the Navigator. The Spearman ranked correlation coefficients between the MRI Navigator heart motion and the VTS chest (ρ_C) and abdomen (ρ_A) markers are also shown.

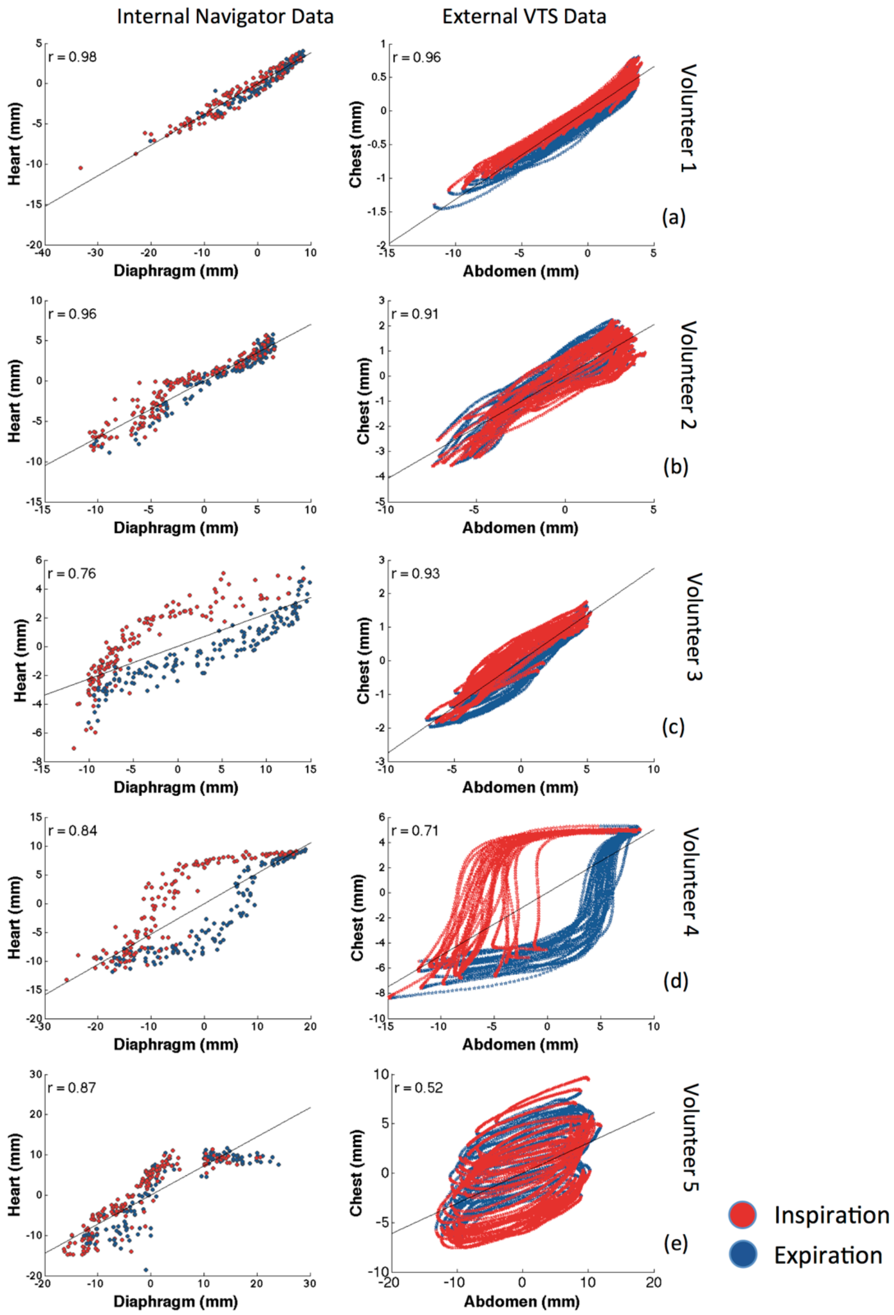

Figure 3.6 Shown in (a) through (e) are 2D scatter plots of pair-wise comparisons of the navigator data for the heart and the diaphragm, and the VTS data for the external chest and abdomen markers for five volunteers. The straight lines are linear fits to the data with Pearson's correlation coefficient r in upper left corner of each plot. The respiratory signals acquired from the navigator and VTS are separated into inspiration and expiration for better visualization of the inspiratory and expiratory trajectories of the heart and external markers. Note scales vary for each plot and that the higher sampling rate of the external markers is evident in the increased density of the points plotted.

It is difficult to visualize the differences in the motion of the heart versus the external tracking of motion in Figure 3.5 (b) and (c). This is better seen in the 2D scatter plots shown in Figure 6, which provides results for measurements in these two volunteers plus three more of our nine volunteers. As illustrated on the left in this figure there was in many but not all cases a strong, positive correlation between the internal motions of the heart and the diaphragm. The average ± standard deviation in the Pearson correlation coefficient (*r*) over all nine volunteer studies was 0.87 ± 0.13. On the right of this figure is shown the corresponding external motions of the chest and abdomen markers, which also generally show a strong, positive correlation. The average ± standard deviation in the Pearson correlation coefficient was 0.82 ± 0.21.

As shown in the plots of Figure 3.6 not all volunteers exhibited a monotonic relationship between the two tracked motions. Some of the plots show hysteresis, a difference in trajectories between inspiration and expiration as seen with volunteers 3 and 4.

Note that the extent of hysteresis is highly volunteer dependent. In this study of nine volunteers, six showed a linear or monotonic relationship visually for both the internal and external measurements. Further these six had common trajectories in the 2D plots for both inspiration and expiration phases as illustrated in Figure 3.6 (a) and (b). The scatter plots for two other volunteers shown in Figure 3.6 (c) and (d), exhibited moderate to strong hysteresis for both the internal and external measurements, with distinct trajectories for inspiration and expiration. For one case shown in Figure 3.6 (e) the 2D scatter plot for external marker motions of the chest and abdomen showed hysteretic loops drifting downward, while the corresponding scatter plot for internal motion exhibited a monotonic trend. The direction of the hysteretic loops is always counter-clockwise, but with varying degree of hysteresis for every respiratory cycle. The time series plots for this volunteer were shown in Figure 3.5 (c).

The 2D scatter plots of Figure 3.7 provide a direct comparison between the external markers (chest and abdomen) and the internal respiratory motion of the heart for examples of linear and hysteretic motion. The linear case is shown in Figure 3.7(a) and is from volunteers 2. Note that the motion of both the chest and abdomen markers correlates linearly with the internal motion of the heart. The hysteretic case shown in Figure 3.7(b) is from volunteer 4. Note the linear correspondence between the chest motion and internal heart motion; however, the correlation between the abdomen motion and the internal heart motion was poor, which is in good agreement with the results seen in Figure 3.6(d).

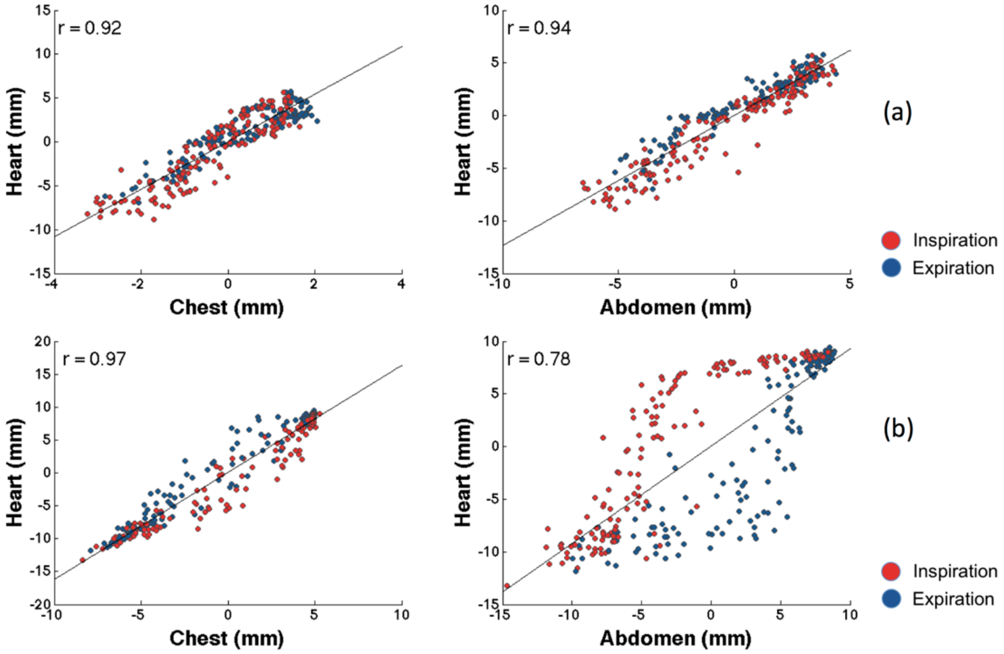

Figure 3.7 2D scatter plots of pair-wise comparisons between the navigator data of the heart and the down-sampled VTS data of the external chest and abdomen markers for two cases: (a) linear pattern (Volunteer 2), and (b) hysteretic pattern (Volunteer 4). The plots illustrate the correlation between the external markers (chest and abdomen) and the internal respiratory motion of the heart.

Figure 3.8 shows the original and repeat studies at a later date for Volunteer 4 that showed the greatest extent of hysteresis. From the plots we see that the volunteer exhibited hysteretic pattern both internally and externally when deeper breathing was performed; on the other hand, the respiratory curves on the scatter plots showed a linear trend for shallow breathing. This indicated that the hysteretic effect is not the characteristic of this individual but rather could manifest randomly, i.e. it not only varies between volunteers but in time (or with extent of respiration) in a given volunteer.

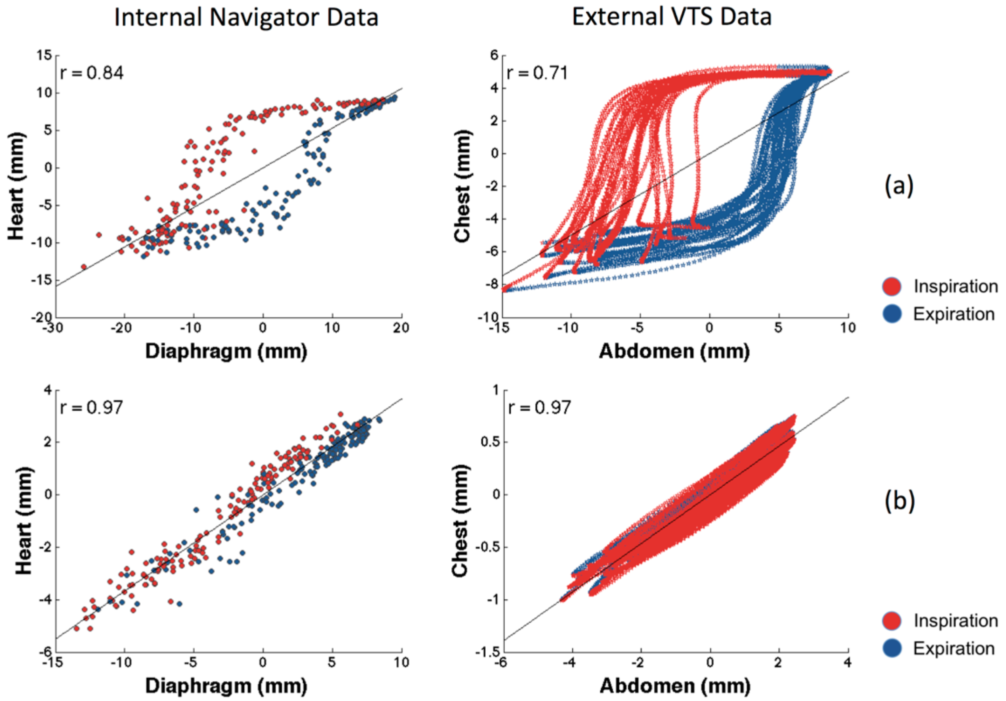

Figure 3.8 2D scatter plots of pair-wise comparisons of the navigator data for the heart and the diaphragm, and the VTS data for the external chest and abdomen markers for one volunteer 4 are shown for (a) deep breathing and (b) shallow breathing acquired on different days. Note how these plots clearly show the hysteretic (a) and linear (b) behavior internally and externally.

3.4 Discussion

The irregular breathing patterns along with the hysteresis observed in our studies may have significant impact on the accuracy and reliability of the gating / binning methods used in respiratory-motion correction in emission tomography when imaging the heart and other structure in the chest and abdomen. It can also impact the formation of 4D-CT studies [4, 5, 25, 26] and patient treatment in radiation therapy [10, 14, 27-29]. As illustrated in Figure 3.6 (c) and (d), with external-signal amplitude based binning of list-mode studies, when hysteresis is present a fixed range of displacement of the abdomen marker can corresponds to a deviation in displacement of the heart for expiratory and inspiratory respiratory phases. Performing amplitude binning in such a study would result in considerable variation in the SI location of the heart in the list-mode events placed in that bin. This would result in an incomplete correction of respiratory motion.

In addition to the hysteresis, variation in respiratory amplitude and baseline as has shown in Figures 3.5(c) and 3.6(e) presents another complication when performing amplitude binning. This can result in incorrect sorting of spatial positions of the heart for a given amplitude bin eventually affecting the diagnostic accuracy of the images. Such variability has been determined to be present in patients undergoing PET/CT [30] and SPECT [31] imaging.

The most direct approach to tackle the problem of hysteresis is to treat the inspiration and expiration phases separately [4]. However, the resulting images are subjected to poor signal-to-noise ratio since each of the frames contains only part of the counts available throughout the acquisition of a respiration average emission dataset therefore yielding noisy images. Alternatively, since the pattern of hysteresis if present manifests itself both internally and externally one could combine the respiratory information acquired from the chest or the abdomen areas with a motion model that takes hysteresis into account when predicting the motion of the heart. Conceivably, from the examples presented in this study, using the respiratory information from both the chest and the abdomen regions, comparable to the work shown by Fayad *et al.* [32] and by Odille *et al*. [33], along with a better motion model to account for both hysteresis and irregular breathing patterns would result in more accurate respiratory motion correction. An excellent recent review of respiratory motion modeling provides more details on the current status of such modeling in medical imaging [34].

We are uncertain of the physiological basis for our observations that the presence of hysteresis of heart motion internally is manifested externally in a difference in the chest and abdomen marker motion. One possible explanation is the following. There are two principle mechanisms for changing respiratory volume of the lungs. The first is that of the SI motion of the diaphragm, which would result in AP motion of markers on the abdomen as demonstrated by Vedam et al [7]. The second is a rocking of the ribs, which expands the circumference of the chest [35], thereby causing AP motion of chest markers. The interplay of these with the viscoelastic nature of the lungs [9] and possible internal imbalances in lung pressure [36] could play a part in retarding the internal motion of the heart. Such a damping could then result in delayed periodic motion as observed in a forced damped oscillation [37]. However study of a much larger population of volunteers including those with lung pathologies is needed to further clarify the physiological basis for our findings.

3.5 Conclusion

In this study, we investigated the correspondence of the respiratory motion of the heart as assessed internally using the Navigator methodology to the external motion of markers measured by a VTS. We determined hysteresis and irregular motion to be present in several of our volunteers. The hysteresis between the markers of the chest and the abdomen correlates with SI motion of the heart and the diaphragm. It is thus potentially a means to indicate the presence of hysteresis and could be useful in predicting the respiratory motion of the heart. The motion of the ensemble of the markers combined with a better motion model may be useful in providing an improved strategy for binning list-mode emission data into more accurate, consistent binning. Our future work will involve the development of a suitable motion model to account for hysteresis and irregular breathing, and then to study the performance of the developed model on phantom simulations and clinical studies.

Acknowledgment

This work was supported by the National Institute of Biomedical Imaging and Bioengineering (NIBIB) under grant R01 EB001457 and a grant from Philips Healthcare. The contents are solely the responsibility of the authors and do not necessarily represent the official views of the NIBIB or Philips Medical Systems.

3.6 References

[1] V. Dilsizian, S. Bacharach, R. Beanlands, S. Bergmann, D. Delbeke, R. Gropler*, et al.*, "PET myocardial perfusion and metabolism clinical imaging," *Journal of Nuclear Cardiology,* vol. 16, pp. 651-651, 2009/08/01 2009.

[2] T. A. Holly, B. G. Abbott, M. Al-Mallah, D. A. Calnon, M. C. Cohen, F. P. DiFilippo*, et al.*, "Single photon-emission computed tomography," *J Nucl Cardiol,* vol. 17, pp. 941-73, Oct 2010.

[3] K. Cho, S. Kumiata, S. Okada, and T. Kumazaki, "Development of respiratory gated myocardial SPECT system," *J Nucl Cardiol,* vol. 6, pp. 20-8, Jan-Feb 1999.

[4] J. R. Olsen, W. Lu, J. P. Hubenschmidt, M. M. Nystrom, P. Klahr, J. D. Bradley*, et al.*, "Effect of novel amplitude/phase binning algorithm on commercial four-dimensional computed tomography quality," *International Journal of Radiation Oncology Biology Physics,* vol. 70, pp. 243-52, Jan 1 2008.

[5] A. F. Abdelnour, S. A. Nehmeh, T. Pan, J. L. Humm, P. Vernon, H. Schoder*, et al.*, "Phase and amplitude binning for 4D-CT imaging," *Phys Med Biol,* vol. 52, pp. 3515-29, Jun 21 2007.

[6] M. Dawood, F. Buther, N. Lang, O. Schober, and K. P. Schafers, "Respiratory gating in positron emission tomography: A quantitative comparison of different gating schemes," *Medical Physics,* vol. 34, pp. 3067-3076, 07/00/ 2007.

[7] S. S. Vedam, V. R. Kini, P. J. Keall, V. Ramakrishnan, H. Mostafavi, and R. Mohan, "Quantifying the predictability of diaphragm motion during respiration with a noninvasive external marker," *Med Phys,* vol. 30, pp. 505-13, Apr 2003.

[8] K. McLeish, D. L. Hill, D. Atkinson, J. M. Blackall, and R. Razavi, "A study of the motion and deformation of the heart due to respiration," *IEEE Trans Med Imaging,* vol. 21, pp. 1142-50, Sep 2002.

[9] K. Nehrke, P. Bornert, D. Manke, and J. C. Bock, "Free-breathing cardiac MR imaging: Study of implications of respiratory motion-initial results," *Radiology,* vol. 220, pp. 810-815, Sep 2001.

[10] Y. Seppenwoolde, H. Shirato, K. Kitamura, S. Shimizu, M. van Herk, J. V. Lebesque*, et al.*, "Precise and real-time measurement of 3D tumor motion in lung due to breathing and heartbeat, measured during radiotherapy," *Int J Radiat Oncol Biol Phys,* vol. 53, pp. 822-34, Jul 15 2002.

[11] J. M. Blackall, S. Ahmad, M. E. Miquel, J. R. McClelland, D. B. Landau, and D. J. Hawkes, "MRI-based measurements of respiratory motion variability and assessment of imaging strategies for radiotherapy planning," *Physics in Medicine and Biology,* vol. 51, pp. 4147-4169, Sep 7 2006.

[12] P. C. Chi, P. Balter, D. Luo, R. Mohan, and T. Pan, "Relation of external surface to internal tumor motion studied with cine CT," *Medical physics,* vol. 33, pp. 3116-23, Sep 2006.

[13] C. Liu, A. M. Alessio, and P. E. Kinahan, "Respiratory motion correction for quantitative PET/CT using all detected events with internal---external motion correlation," *Medical Physics,* vol. 38, pp. 2715-2723, 05/00/ 2011.

[14] D. Ruan, J. A. Fessler, J. M. Balter, R. I. Berbeco, S. Nishioka, and H. Shirato, "Inference of hysteretic respiratory tumor motion from external surrogates: a state augmentation approach," *Physics in Medicine and Biology,* vol. 53, pp. 2923-2936, Jun 7 2008.

[15] S. J. McQuaid, T. Lambrou, and B. F. Hutton, "A novel method for incorporating respiratory-matched attenuation correction in the motion correction of cardiac PET-CT studies," *Phys Med Biol,* vol. 56, pp. 2903-15, May 21 2011.

[16] I. Burger and E. M. Meintjes, "Elliptical subject-specific model of respiratory motion for cardiac MRI," *Magn Reson Med,* Oct 8 2012.

[17] P. Dasari, K. Johnson, J. Dey, J. M. Mukherjee, Z. Shaokuan, C. Connolly*, et al.*, "MRI investigation of the linkage between respiratory motion of the heart and markers on patient's abdomen and chest: Implications for respiratory amplitude binning list-mode PET and SPECT studies," in *Nuclear Science Symposium and Medical Imaging Conference (NSS/MIC), 2011 IEEE*, 2011, pp. 3748-3751.

[18] J. E. McNamara, P. H. Pretorius, K. Johnson, J. M. Mukherjee, J. Dey, M. A. Gennert*, et al.*, "A flexible multicamera visual-tracking system for detecting and correcting motion-induced artifacts in cardiac SPECT slices," *Medical Physics,* vol. 36, pp. 1913-1923, 05/00/ 2009.

[19] M. A. King, J. Dey, K. Johnson, P. Dasari, J. Mukherjee, J. McNamara*, et al.*, "Use of MRI to assess the prediction of heart motion by stereo-tracking of markers on the body surface," in *Nuclear Science Symposium Conference Record (NSS/MIC), 2010 IEEE*, 2010, pp. 3320-3325.

[20] R. L. Ehman and J. P. Felmlee, "Adaptive technique for high-definition MR imaging of moving structures," *Radiology,* vol. 173, pp. 255-63, Oct 1989.

[21] Y. Wang, R. C. Grimm, J. P. Felmlee, S. J. Riederer, and R. L. Ehman, "Algorithms for extracting motion information from navigator echoes," *Magn Reson Med,* vol. 36, pp. 117-23, Jul 1996.

[22] S. C. Jean Dickinson Gibbons, *Nonparametric Statistical Inference*, 5 ed.: Chapman and Hall, 2010.

[23] D. J. Best and D. E. Roberts, "Algorithm {AS} 89: The upper tail probabilities of {S}pearman's rho," *Journal of the Royal Statistical Society. Series C (Applied Statistics),* vol. 24, pp. 377-379, // 1975.

[24] J. Dey, T. Pan, D. J. Choi, D. Robotis, M. S. Smyczynski, P. H. Pretorius*, et al.*, "Estimation of Cardiac Respiratory-Motion by Semi-Automatic Segmentation and Registration of Non-Contrast-Enhanced 4D-CT Cardiac Datasets," *IEEE Trans Nucl Sci,* vol. 56, pp. 3662-3671, Dec 8 2009.

[25] T. Pan, T. Y. Lee, E. Rietzel, and G. T. Chen, "4D-CT imaging of a volume influenced by respiratory motion on multi-slice CT," *Med Phys,* vol. 31, pp. 333-40, Feb 2004.

[26] W. Lu, P. J. Parikh, J. P. Hubenschmidt, J. D. Bradley, and D. A. Low, "A comparison between amplitude sorting and phase-angle sorting using external respiratory measurement for 4D CT," *Med Phys,* vol. 33, pp. 2964-74, Aug 2006.

[27] S. Webb, "Motion effects in (intensity modulated) radiation therapy: a review," *Phys Med Biol,* vol. 51, pp. R403-25, Jul 7 2006.

[28] P. J. Barnes, C. Baldock, S. R. Meikle, and R. R. Fulton, "Benchmarking of a motion sensing system for medical imaging and radiotherapy," *Phys Med Biol,* vol. 53, pp. 5845-57, Oct 21 2008.

[29] Y. Seppenwoolde, R. I. Berbeco, S. Nishioka, H. Shirato, and B. Heijmen, "Accuracy of tumor motion compensation algorithm from a robotic respiratory tracking system: a simulation study," *Med Phys,* vol. 34, pp. 2774-84, Jul 2007.

[30] P. Kinahan, S. Wollenweber, A. Alessio, S. Kohlmyer, L. MacDonald, T. Lewellen*, et al.*, "Impact of respiration variability on respiratory gated whole-body PET/CT imaging," *J NUCL MED MEETING ABSTRACTS,* vol. 48, pp. 196P-, May 1, 2007 2007.

[31] J. M. Mukherjee, K. L. Johnson, J. E. McNamara, and M. A. King, "Quantitative Study of Rigid-Body and Respiratory Motion of Patients Undergoing Stress and Rest Cardiac SPECT Imaging," *Nuclear Science, IEEE Transactions on,* vol. 57, pp. 1105-1115, 2010.

[32] H. Fayad, T. Pan, O. Pradier, and D. Visvikis, "Patient specific respiratory motion modeling using a 3D patient's external surface," *Medical Physics,* vol. 39, pp. 3386-3395, 06/00/ 2012.

[33] F. Odille, N. Cindea, D. Mandry, C. Pasquier, P. A. Vuissoz, and J. Felblinger, "Generalized MRI reconstruction including elastic physiological motion and coil sensitivity encoding," *Magn Reson Med,* vol. 59, pp. 1401-11, Jun 2008.

[34] J. R. McClelland, D. J. Hawkes, T. Schaeffter, and A. P. King, "Respiratory motion models: a review," *Med Image Anal,* vol. 17, pp. 19-42, Jan 2013.

[35] Martin D. E. and J. W. Youtsey., *Respiratory Anatomy and Physiology*: St. Louis: The C. V. Mosby Company 1988.

[36] D. A. Low, P. J. Parikh, W. Lu, J. F. Dempsey, S. H. Wahab, J. P. Hubenschmidt*, et al.*, "Novel breathing motion model for radiotherapy," *International Journal of Radiation Oncology Biology Physics,* vol. 63, pp. 921-9, Nov 1 2005.

[37] E. Gutiérrez and C. Paulotto, "Delay Correlation of Mechanical Hysteresis and Damping," *Journal of Structural Engineering,* vol. 136, pp. 76-85, 2010/01/01 2009.

Chapter 4 - Adaptation of the Bouc-Wen Model to Compensate for Hysteresis in Respiratory Motion for the List-mode Binning of Cardiac SPECT and PET Acquisitions: Testing using MRI

Paul Dasari [a,b], Mohammed S. Shazeeb [a,b], Arda Konik [a], Clifford Lindsay [c], Joyeeta M. Mukherjee [a], Karen L. Johnson [a] and Michael A. King [a].

[a] Department of Radiology, University of Massachusetts Medical School, Worcester
[b] Department of Biomedical Engineering, Worcester Polytechnic Institute, Worcester
[c] Department of Computer Science, Worcester Polytechnic Institute, Worcester

Part of this work was presented at the 2012 annual meetings of the IEEE Nuclear Science Symposium & Medical Imaging Conference, Anaheim, California, USA.

Manuscript in Progress

Abstract— Binning list-mode acquisitions as a function of a surrogate signal related to respiration has been employed to reduce the impact of respiratory motion on image quality in cardiac emission tomography (SPECT and PET). Inherent in amplitude binning is the assumption that there is a monotonic relationship between the amplitude of the surrogate signal and respiratory motion of the heart. This assumption is not valid in the presence of hysteresis when heart motion exhibits a different relationship with the surrogate during inspiration and expiration. The purpose of this study was to investigate the novel approach of using the Bouc-Wen model to provide a signal accounting for hysteresis when binning list-mode data with the goal of thereby improving motion correction. The study in based on our previous observations that hysteresis between chest and abdomen markers was indicative of hysteresis between abdomen markers and the internal motion of the heart. In nineteen healthy volunteers we determined the internal motion of the heart and diaphragm in the superior-inferior (SI) direction during free-breathing using MRI navigators. A Visual Tracking System (VTS) synchronized with MRI acquisition tracked the anterior-posterior (AP) motions of external markers placed on the chest and abdomen. This data was employed to develop and test the Bouc-Wen model by inputting the VTS derived chest and abdomen motions into it and using the resulting output signals as surrogates for cardiac motion. The data of the volunteers were divided into training and testing sets. The training set was used to obtain initial values for the model parameters for all of the volunteers in the set, and for set members based on whether they were or were not classified as exhibiting hysteresis

using a metric derived from the markers. These initial parameters were then employed with the testing set to estimate output signals. Pearson's linear correlation coefficient between the abdomen, chest, and Bouc-Wen derived signals versus the true internal motion of the heart from MRI was used to judge the signals match to the heart motion. The results show that the Bouc-Wen model generated signal correlated better on average with the heart motion compared to either of the signals from the external markers alone, although the improvement was not statistically significant. Furthermore, the model's flexibility was observed by tailoring it to subject-specific respiratory patterns: either monotonic or hysteretic patterns. The results suggest that the proposed model has the potential to be a unified framework for modeling hysteresis in respiratory motion in cardiac perfusion studies, and beyond.

4.1 Introduction

Respiratory motion is inevitable in emission tomography due to the long acquisition times of emission scans. This leads to image artifacts and errors in quantification [1-3]. With the emergence of multimodality imaging scanners (e.g., PET/CT and SPECT/CT), the problems from uncorrected motion have been amplified due to the artifacts present in the attenuation corrected images caused by an inconsistency in respiratory motions between the transmission / CT and the emission data [4-7]. In addition to inaccurate attenuation correction, respiratory motion leads to image blur resulting in loss of contrast and biased quantification [8].

Several acquisition methods based on respiratory gating have been proposed for mitigating the effects of respiratory motion [9-11]. Such gated acquisitions yield a number of images corresponding to distinct parts of the respiratory cycle. Each gated set of images contains only a small part of the total respiratory motion resulting in images with minimal motion artifacts. Respiratory gating of the emission data can be performed employing: (a) phase-based gating and/or (b) amplitude-based gating. Both are based on a respiratory signal obtained by tracking some aspect of respiratory motion in the subject. In phase-based gating, the emission data is sorted based on the phase or relative time point within the subject’s respiratory cycle. In this approach, however, the extent of respiratory motion is not considered thereby resulting in inconsistent distribution of motion among the set of gated images. On the other hand, in amplitude-based gating, the sorting of emission data is based on the measured amplitude of the respiratory signal, irrespective of the phases in the subject's respiratory cycle. This method captures the extent of respiratory motion more accurately. This is especially important when patient respiration is variable. Experimental analysis from various studies [12-16] indicates that the amplitude-based gating is the preferred method, with the exception of when respiration is very regular. The amplitude-based gating method assumes that the organs move in the same trajectory for both inspiration and expiration. However, studies have shown that certain individuals can exhibit hysteresis, in which the organs follow different trajectories during the inspiratory and expiratory phases of the respiratory cycle [17-19]. The effects of hysteresis have been investigated and reported for lung tumor motion [20-22], and for a lesser extent for heart motion [17, 18].

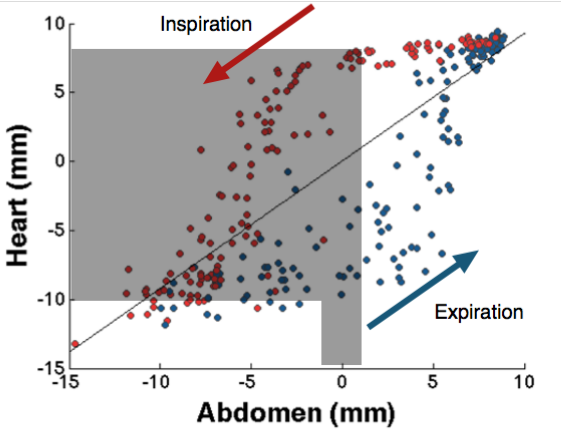

Figure 4.1 2D Scatter plot illustrating the phenomenon of hysteresis in the respiratory motion of the heart relative to that of an external abdominal marker. The MRI Navigator methodology was employed to measure the superior/ inferior motion of the heart in a free-breathing human volunteer. The inspiration and expiration phases depict distinct trajectories of the heart motion. The shaded area shows the extent of residual motion present in the middle-bin if abdomen signal were to be selected in amplitude binning

In the presence of hysteresis, for a given displacement of an external respiratory signal (e.g., from markers or bellows on patient’s surface), the actual internal motion of the heart can show a variation in its displacement. This is illustrated using the MRI Navigator data from a volunteer in Fig. 1, wherein the position of the heart is very different with respect to the position of the abdomen during expiratory and inspiratory phases of the respiratory cycle. Therefore, performing binning using a hysteretic respiratory signal based on amplitude alone results in suboptimal correction. This complex internal behavior indicates that estimating the heart motion from a single parameter (such as the respiratory signal related to abdominal motion) may not fully describe the motion trajectories of the heart thereby introducing errors and reducing the effectiveness of amplitude-based binning method.

Dasari *et. al*.[19], investigated the relationship between the anterior-posterior (AP) motion of external markers on the chest and the abdomen of free-breathing human volunteers using a Visual Tracking System (VTS) [23]. In addition, the relationship between the superior-inferior (SI) motion of the heart and the diaphragm were investigated by internal tracking using MR-Navigators in synchrony with external tracking VTS. This study inferred that if hysteresis is present internally between the heart and diaphragm, a similar behavior might manifest externally in the chest and the abdomen signals. The most direct approach to address the problem of hysteresis is to treat the inspiratory and expiratory phases separately using the amplitude-based gating method [12]. However, the resulting gated images are deteriorated by lower signal-to-noise ratio (SNR), since each gated image possesses a smaller portion of the total counts available at that signal amplitude. This also nearly doubles the number of reconstructions necessary to estimate respiratory motion for later correction in a combined iterative reconstruction with motion correction of all the acquired events [16]. Therefore, a method that accounts for the effects of hysteresis without sacrificing the SNR of the reconstructed images or significantly increasing processing time would be desirable. One such method can be based on using the respiratory information from both the chest and the abdomen regions [24] in combination with a better motion model to account for the effects of hysteretic respiratory motion.

The hysteretic behavior is encountered in a diverse range of processes such as magnetism, ferro-electricity, mechanics, structures, biology and other areas. Several mathematical models [25] have been put forth to describe the behavior of hysteretic processes including the Duhem model [26], the Preisach model [27], and the Bouc-Wen model [28-30]. The Bouc-Wen model is popular in mechanical and structural engineering due to its simple numerical implementation and its ability to represent a wide range of hysteretic loop shapes. The Bouc-Wen model in its original form generates stable clockwise hysteretic loops while hysteresis associated with the respiratory system is counterclockwise [17, 19]. Therefore, in this study we utilized a modified Bouc-Wen model [31, 32] to estimate the heart position relative to the external signals influenced by hysteretic respiratory motion. We tested the proposed

Bouc-Wen model in accounting for hysteresis using the MRI data of the volunteers, as detailed in the following section.

4.2 Materials and Methods

4.2.A Subjects

Nineteen volunteers without counter-indications to MRI were recruited for this study. The participation of volunteers for motion tracking using both MRI and VTS was in compliance with IRB approval and informed consent. The volunteers were prepared for the VTS stereo imaging and MRI acquisition by wrapping bands with markers (2-cm diameter retro-reflective markers filled with copper sulfate solution) about their chest and abdomen as illustrated in Figure 4.2. The volunteers were instructed to breathe slowly and regularly for approximately a 5-minute period during which the motion associated with the markers and the internal organs were tracked by VTS and MRI, respectively.

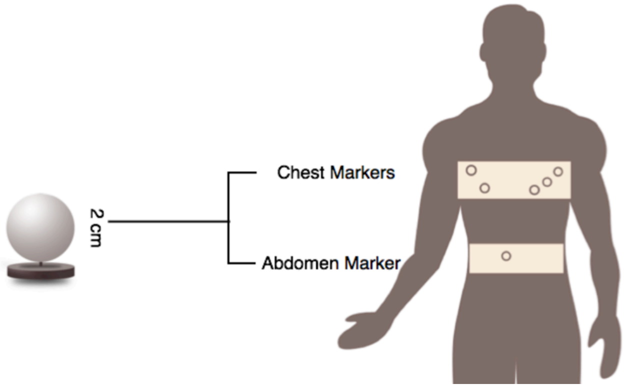

Figure 4.2 Layout of markers used on volunteers for tracking external chest and abdomen motions. The 2-cm diameter retro-reflective markers were used for VTS tracking.

4.2.B External Respiratory Motion Tracking System: VTS

The VTS employed in this study allows near-infrared tracking of multiple markers within the 3-dimensional imaging volume of the MRI as shown in Figure 4.3. The components of the VTS include: the near-infrared cameras, the controlling hardware module, and the software to analyze and present the data. Three cameras of the VTS, mounted on the wall of the MRI room, were arranged in a manner such that the center of the volume to be tracked is at the iso-center of the MRI scanner. Before each experimental session, the VTS was calibrated for stereo motion-tracking and tested for minimal RF interference with the MRI as discussed in [33]. The VTS performs stereo imaging of the external retro-reflective markers placed on the thoracic/abdominal regions at 30 frames per second throughout the MR acquisition. Synchronization between the MRI scanner and the VTS was established by using a trigger signal from the MRI scanner at the beginning of acquisition to start motion capture by the VTS. Example plots of the AP motion of the markers for one subject are shown in Figure 4.4a.

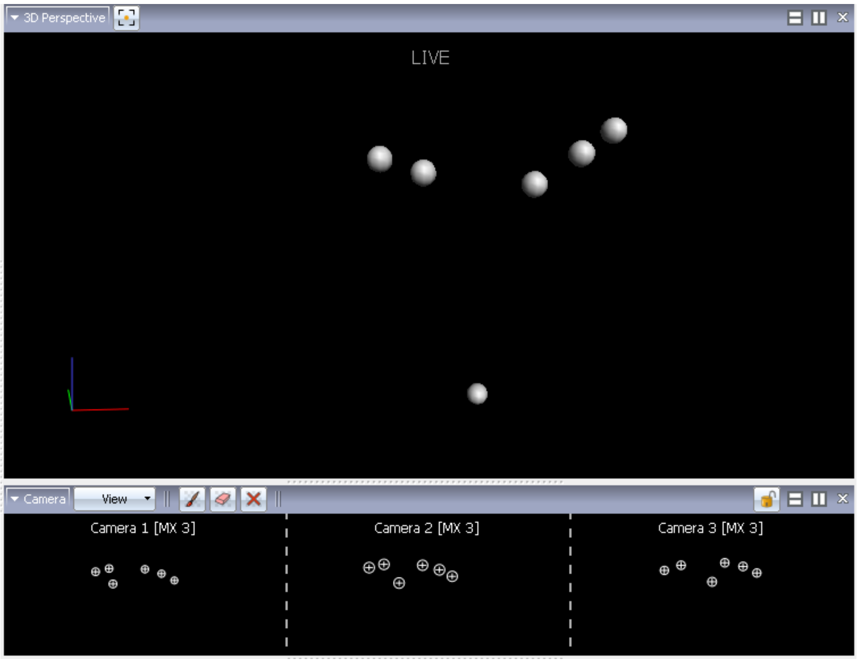

Figure 4.3 Marker layout view as seen in VTS software. The top window shows a 3D rendering of the markers placed on the subject's body within the imaging volume as determined by the analysis of the three stereo cameras. 2D renditions of the marker locations from each of the cameras are shown in bottom windows.

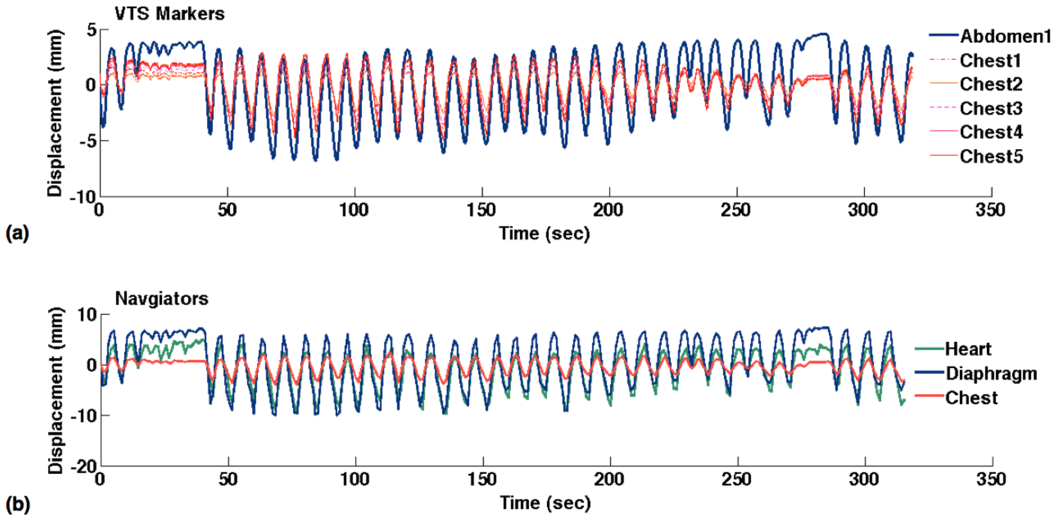

Figure 4.4 (a) Plot of the AP displacements of the external chest and abdomen markers as a function of time as measured by the VTS for a subject (b) Plot of the displacements of the internal heart, diaphragm and chest wall respiratory motions obtained by the respective MRI navigators as a function of time.

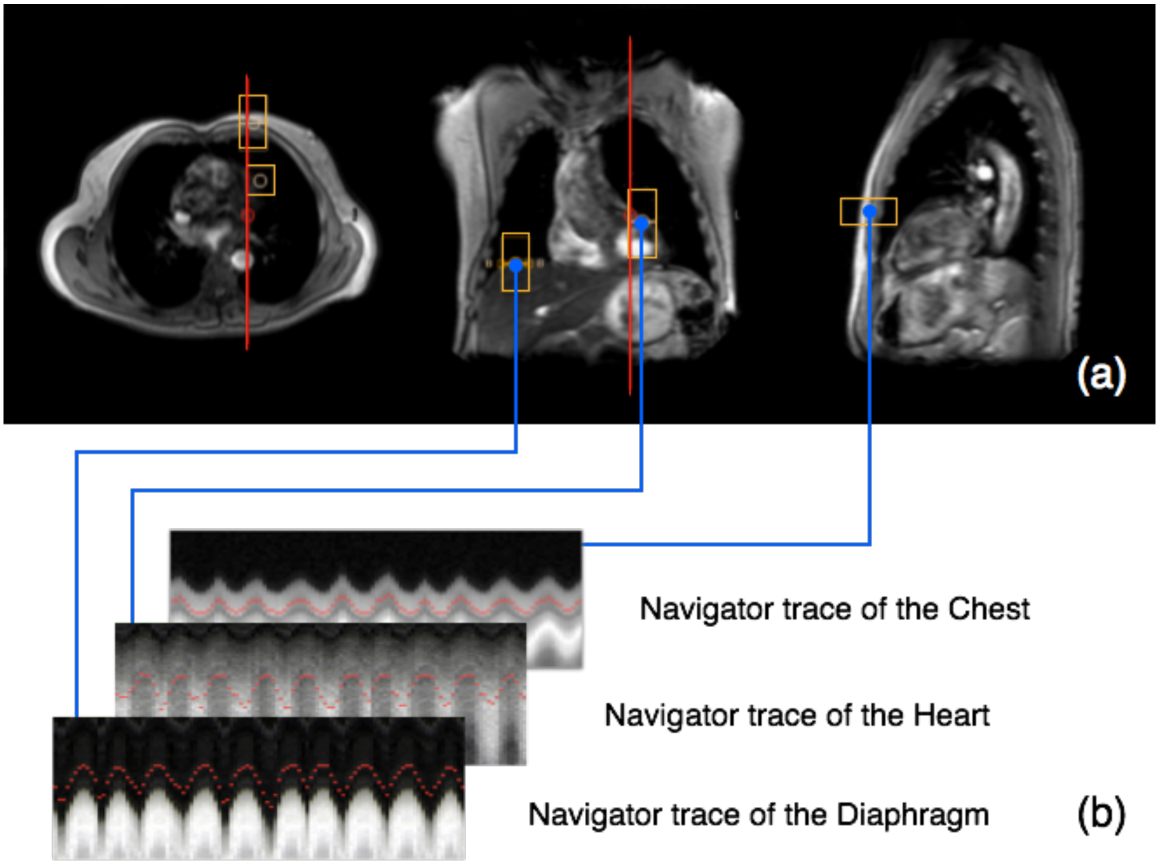

Figure 4.5 (a) Positioning of navigator beams (boxes) on the dome of the right hemi-diaphragm, the left ventricle, and the chest wall. The lines in the trans-axial and the coronal slices indicate the position of the sagittal slice acquired along with the navigator beams. (b) The output from the 3 navigator beams are shown as plots of 1D gray-scale information perpendicular to each body interface versus time. These portray the respiratory motions of the diaphragm, heart, and chest wall.

4.2.C Internal Respiratory Motion Tracking System: MR Navigator technique

MR imaging of the participants was performed using a Philips Healthcare ACHIEVA 3.0-T whole body MRI scanner. The MRI software provided three independent pencil-beam navigator radio-frequency pulses [34]. Each pulse can be freely placed in space at any desired angle as guided by patient anatomy in pilot scans. As illustrated in Figure 4.5, the three navigator windows were localized on the superior left-ventricular wall/lung boundaries, the right diaphragm, and the anterior wall of the chest to track the motion of the corresponding structures. An example of the observed displacements is shown in Figure 4.4b. The multi-navigator MR dynamic imaging through the left ventricle of the heart was performed for 300 dynamic scans during continuous breathing using the ECG-triggered single shot, 2D Fast-Field-Echo sequence, with TR/TE = 5.5/2.1 ms, 128×128 image matrix, 3 mm voxel size, and 250 ms acquisition window at mid-diastole.

4.2.D Modeling Respiratory Motion using the BW Model

In this study, we utilized a variant of the BW model [31, 32] to estimate the internal motion of the heart by utilizing the respiratory motion from the chest and the abdomen regions. This model was experimentally modified to describe counter-clockwise hysteretic loops as observed in respiratory dynamics (Fig. 1). This modified form is given as:

$$\dot{w} = \rho(\dot{x} + \delta\, x\, |\dot{w}| - \sigma\, |\dot{x}|\, w - \gamma\, w|\dot{w}|) \tag{4.1}$$

where, *x(t)* and *w(t)* represent the anterior-posterior (AP) displacements of the abdomen and chest markers as a function of time, respectively. Also in this equation $|\dot{w}| = \dot{w} \cdot sgn(\dot{w}), |\dot{x}| = \dot{x} \cdot sgn(\dot{x}), \dot{w} = dw/dt\,, \dot{x} = dx/dt\,, sgn(\dot{x}) = \begin{cases} -1\; if\; \dot{x} < 0 \\ 0\; if\; \dot{x} = 0 \\ 1\; if\; \dot{x} > 0 \end{cases}$, and *ρ, δ, σ,* and *γ* are the parameters that determine the shape and extent of hysteresis in the modified BW model.

Instead of the respiratory rates in Eq. (4.1), we are interested in the variation of respiratory motion between the chest and the abdomen regions, given by *dw/dx*. This can be derived by rearranging Eq. (1) and dividing it by the respiratory rate *dx/dt*:

$$w_{Est} = dw/dx = \rho(1 - \sigma\, w\, sgn(x))/(1 - \rho\, \delta\, x\, sgn(w) + \rho\, \gamma\, w\, sgn(w)) \quad (4.2)$$

The differential term (w_{Est}) represents the estimated data points on the hysteretic loop, which describes the estimated internal heart motion information in the superior–inferior direction. w_{Est} will be the new respiratory signal, which replaces the abdomen signal in performing the amplitude binning of the list mode data to estimate the heart motion with minimal hysteresis.

4.2.E Parameter Identification Scheme

A critical first step when employing an iterative fitting process is the selection or identification of the initial values of the parameters. Although the BW model is widely used for modeling hysteresis in other disciplines, to the best of our knowledge,, its application to fit respiratory hysteresis has not been reported. Thus, the following parameter identification scheme was employed to determine the optimal initial set of parameter values for a given respiratory pattern (either monotonic or hysteretic).

Herein, the sum-squared error (*E*) between the model-response (w_{Est}) and the actual experimental value (w) was used as the objective function and expressed as

$$E = \sum_{m=1}^{M} (w_{Est}(m) - w(m))^2 \quad (4.3)$$

where, M is the total number of samples, $w(m)$ denotes the observed experimental value of the m^{th} sample of the chest marker, and $w_{Est}(m)$ denotes the corresponding m^{th} estimated value from the model expressed by Eq. (4.2). The optimization problem can be stated as the minimization of this objective function. To solve the optimization problem, the Nelder–Mead simplex algorithm was adopted in Eq. (4.3) iteratively [35]. The MATLAB optimization algorithm (*fmincon*) was used to implement the iterative process. Since hysteresis is a non-linear phenomenon, fitting to experimental data with a multi-parameter non-linear model is done using an iterative procedure that require initial values. The procedure must start with the given initial values for each parameter, inappropriate starting values can prevent the procedure from finding a best fit by converging to a local minimum rather than the global minimum. Therefore, it is imperative for the optimization algorithm to begin the iterations with a good initial estimate of the four parameters to avoid being trapped in local minimums. To circumvent the use of arbitrary values as initial parameters, a systematic search was performed to determine a parameter set that results in best fit using an exhaustive search algorithm coupled with the optimization algorithm as illustrated in the flowchart in Figure 4.6. A permutation matrix of parameter values consisting of non-negative real numbers with a row sum of unity was used to sweep through all possible values in steps of 0.05 for each of the four parameters. The estimated values from the model were then correlated with the navigator heart motion (“truth”). A Pearson product-moment linear correlation coefficient (r) was computed to assess the strength of the linear association between the BW model-estimated heart motion and the true heart motion from the navigators, which in-turn depicts the effectiveness of the parameter estimation. The best estimate of the true heart position was obtained using the set of initial parameters from the permutation matrix that resulted in the maximum correlation coefficient (r_{Max}) in the optimization algorithm. Apart from this parameter set, the search resulted in multiple parameter sets that resulted in similar correlational values.

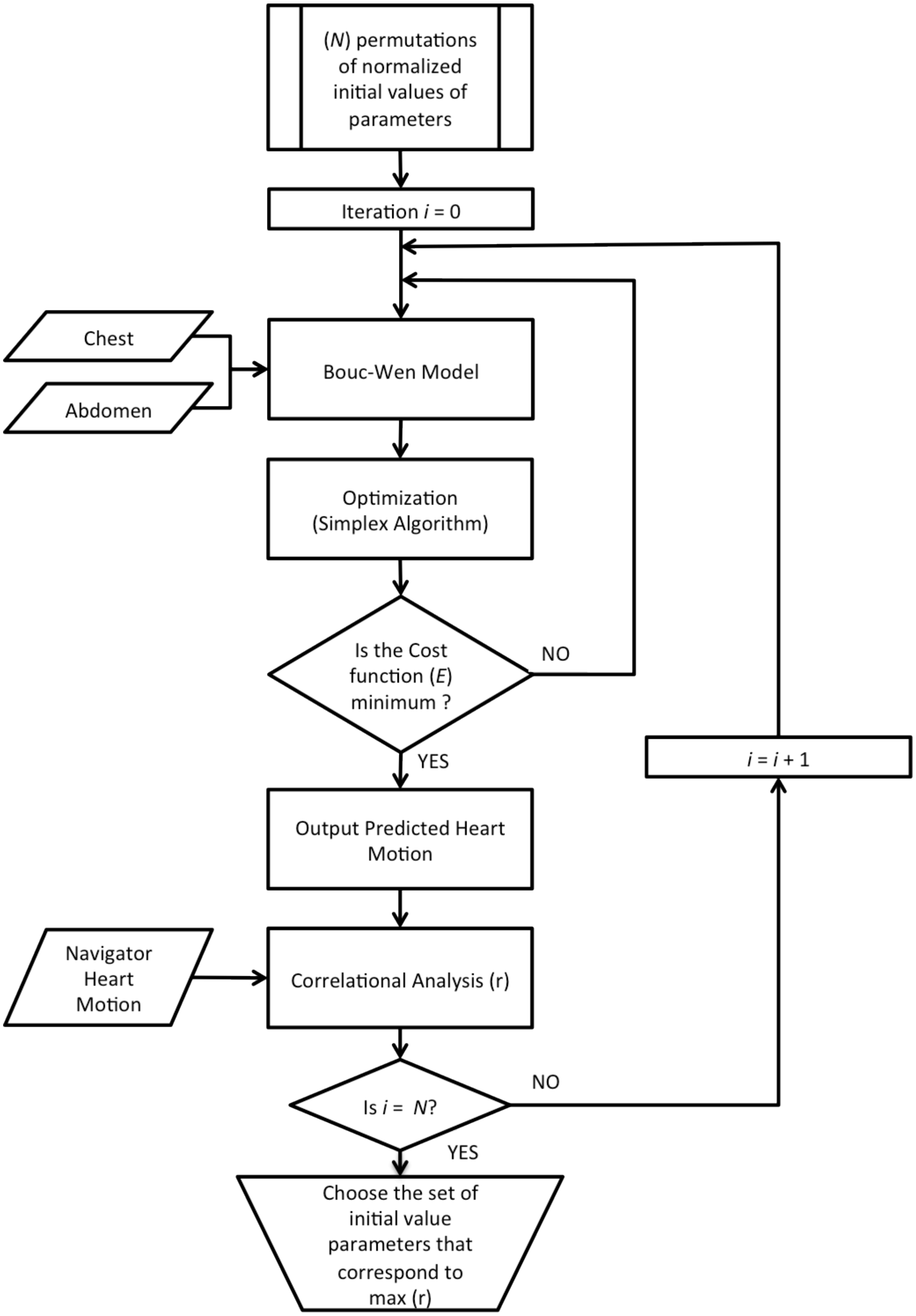

Figure 4.6 Flowchart to determine the optimum set of Bouc-Wen model initial parameters for a given external chest and abdomen respiratory signal.

4.2.F Average-Area algorithm for Respiratory Motion Classification

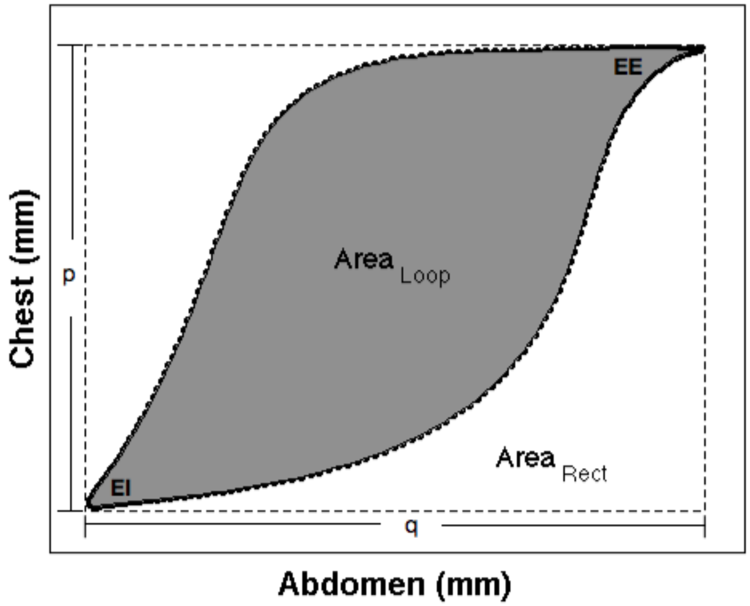

Figure 4.7 Schematic plot of the motion of chest versus abdomen markers during a single respiratory cycle from end-expiration (EE) to end-inspiration (EI) and back to EE when hysteresis is present. The shaded region shows the area of the respiratory loop ($Area_{Loop}$). The ratio of $Area_{Loop}$ /$Area_{Rect}$ averaged over all respiratory cycles is proposed as the parameter to describe the extent of hysteresis in the subject's breathing pattern.

In our preliminary tests of the Bouc-Wen (BW) model we determined that there existed multiple initial parameter sets producing near identical response for a given respiratory pattern and identified a global set of initial parameter values that allowed the model to adequately adapt between monotonic and hysteretic respiratory patterns. However, the performance of the model was further improved when two distinct sets of initial parameter values were employed for each of the respective patterns. The selection process of the initial parameter values unique to monotonic and hysteretic patterns of respiratory motion is described in section 4.2.G. To automate the determination of which set of initial parameters was to be employed, with each dataset we developed a measure of the extent of hysteresis *H*. The motivation for our definition of *H* is illustrated in Figure 4.7. *H* is calculated as:

$$H(\%) = \left[\sum_{i=1}^{N} (Area_{Loop}/Area_{Rect})_i \ / \ N\right] \times 100 \qquad (4.4)$$

where, *N* is the number of respiratory cycles, $Area_{Loop}$ is the area of the individual respiratory cycle, and $Area_{Rect}$ is the area of the rectangle with sides ‘p’ and ‘q’ corresponding to the depth of breathing shown by the chest and abdomen markers, respectively.

4.2.G Training and testing of the BW model for Respiratory Cardiac Motion

Our objective is to determine and validate initial parameter sets for use in estimating respiratory cardiac motion. If this is successful the error in estimating the heart motion can be minimized. In addition to minimizing the error in estimation the computational burden usually associated with exhaustive search algorithm can be minimized. To achieve this, the subject data were divided into training and testing sets to determine the model’s initial parameters and test the estimating ability of the model when employing these initial values.

Training set: A training set of 7 from the 19 available subjects was chosen retrospectively based on the *H* value by sub-setting the original data in a manner that it included examples of 4 monotonic patterns and 3 hysteretic patterns. The algorithm described in section 4.2.E. was applied to these studies to select the initial sets of parameters (one for monotonic and one for hysteretic) to be used with the testing studies to judge the utility of our proposed methodology. The method for selecting the initial parameter sets was performed as follows:

i) A pool of parameter value sets was selected from the permutation matrix such that the Pearson product-moment linear correlation coefficient (*r*) was within 5% of the maximum correlation coefficient (r_{Max}) for each subject as well as across the seven subjects in the training set.

ii) For each of the parameter value sets in the pool, the percentage difference was calculated for each subject by calculating the difference between (r_{Max}) and (*r*) for the corresponding parameter value set.

iii) The mean of the percentage differences corresponding to each parameter value set from the pool was calculated independently for the monotonic subjects, the hysteretic subjects, and the combined seven subjects in the training set.

iv) The parameter sets resulting in the lowest mean percentage difference unique to the monotonic subjects, the hysteretic subjects, and the combined subjects were chosen accordingly.

Testing set: The remaining 12 subjects unused in the training set were considered as the testing set. The proposed Average-Area algorithm discussed in section 4.2.F. was applied on the testing set to determine the algorithm’s ability to select the initial set of parameters determined using the training dataset, which when employed gave similar correlations to the internal heart motion as that of the optimal set obtained through the exhaustive search.

4.2.H Data Analysis

For both training and testing data sets, pair-wise comparisons along with correlational analysis were performed between the navigator heart motion and: 1) the external abdomen marker; 2) the external chest marker; 3) the Bouc-Wen model derived signals. The measure used for assessing the performance of the model in the testing sets was Pearson product-moment linear correlation coefficient (*r*). A paired Student's t-test with Bonferroni correction to account for multiple comparisons was performed with the null hypothesis that the performance between the signals estimating relative heart motion did not differ. A *p*-value of less than 0.05 indicates that the results differ from each other significantly.

4.3 Results

4.3.A Determination of initial model parameter values

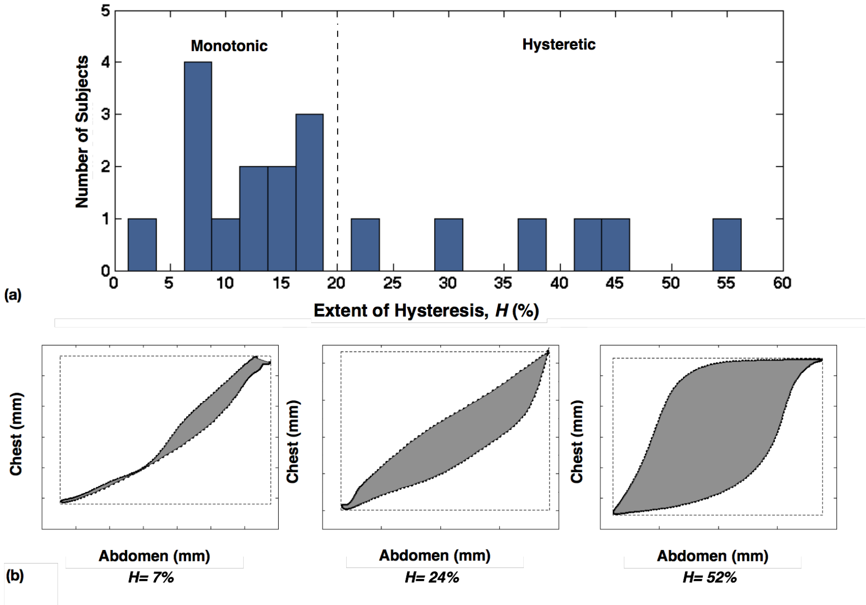

Figure 4.8 (a) Histogram of subjects with respect to the *H* value. Respiratory data with *H* < 20% was considered monotonic and the ones with *H* > 20% was considered hysteretic. (b) Plots illustrating the extent of hysteresis (*H*) in one respiratory cycle for: Monotonic (left), and Hysteretic (center and right) respiratory patterns.

Figure 4.8 (a) shows the plot of the number of subjects whose *H* (measure of extent of hysteresis) fell within binned values versus *H.* Based on these results we selected a threshold value of 20% to categorize their respiratory chest versus abdomen motion as either monotonic or hysteretic. Figure 4.8 (b) shows examples of the extent of hysteresis for one respiratory cycle along with their corresponding *H* values for three subjects with varying *H*.

Table 4.1 Shown are the initial four parameter values along with the corresponding highest correlation coefficient (*r*) values for seven volunteers in the training set. The extent of hysteresis, *H* (%) and the pattern categorization are also tabulated.

Subject #	Initial Parameter Value				Correlation Coefficient (*r*)	*H* (%)	Pattern
	ρ	δ	σ	γ			
1	0	0.1	0.15	0.75	0.953	12	Monotonic
2	0	0.05	0.85	0.20	0.972	12	Monotonic
3	0.1	0.4	0.05	0.45	0.973	7	Monotonic
4	0.05	0.15	0.1	0.7	0.952	8	Monotonic
5	0.05	0.6	0.1	0.25	0.850	22	Hysteresis
6	0.05	0.00	0.60	0.35	0.902	54	Hysteresis
7	0	0	0.05	0.95	0.902	56	Hysteresis

Table 4.1 lists the initial parameter values for each of the 7 studies in the training set which resulted in the highest (*r*) (between the BW model predicted and the navigator signals) obtained from the exhaustive search of the studies in the training set. Also listed are the corresponding values of (*r*), the extent of observed hysteresis (*H*) between the abdomen and chest markers, and the pattern determined by using 20% as a threshold value on *H*.

Note that the set of initial parameters varies from one study to another. As stated in section 4.2.F., no common starting set of initial parameters was observed which resulted in the highest (*r*) for all studies in the training set. However the exhaustive search on the training studies resulted in multiple parameter value sets with nearly maximal (*r*). In clinical applications, besides the computational burden in the use of exhaustive search, the true cardiac motion is unavailable to determine the optimum initial parameters. Hence, using the training set three different parameter sets based on the criteria discussed in section 2.G. were selected. These initial parameter value sets along with their corresponding mean percentage differences for the monotonic, the hysteretic, and the combined subjects are reported in Table 4.2. Notice that using the "monotonic" parameter value set resulted in the lowest percentage difference for the monotonic subjects. Similarly the "hysteretic" and the "global" parameter value sets resulted in the lowest percentage difference for the hysteretic subjects and for the combination of all subjects, respectively, in the training set.

Table 4.2 Shown are the initial parameter value sets with corresponding mean percentage differences for the monotonic (4 subjects), the hysteretic (3 subjects), and the combined (7 subjects) sets.

Parameter Set Type	Parameter Set				Mean Percentage Difference (%)		
	ρ	δ	σ	γ	Monotonic Set	Hysteretic Set	Combined Set
Monotonic	0.05	0.15	0.05	0.75	**0.70**	1.74	1.14
Hysteretic	0.4	0.1	0.4	0.1	1.73	**0.56**	1.23
Global	0.25	0.15	0.25	0.35	0.94	1.12	**1.02**

The performance of the BW model, in estimating the heart motion using the chest and abdomen markers is assessed by correlating with the true cardiac motion determined by the Navigator, is shown for five selected subjects from the training set in Figure 4.9. The first two rows in Figure 4.9 show plots for studies with monotonic patterns, and the last three rows show plots for the hysteretic patterns. The first column shows plots of the chest marker motion as a function of the abdomen marker motion. The corresponding BW model fits obtained using the set of initial parameter values through the Average-Area algorithm are overlaid with the experimental data to illustrate the impact of BW model fitting. The correlation of each of the plotted signals in the first column with the Navigator-measured SI motion of the heart internally is shown in the rest of the scatter plots within the figure in columns 2-4. In each of these plots the correlation coefficients for the two plotted signals are displayed in the upper left corner of each plot. Notice that both visually and by the (*r*) values, the BW model derived signal shows consistently stronger correlation with the internal heart motion than either the chest or abdomen marker signal alone. It should be noted that the exact agreement in the magnitude of these external signals with the internal motion of the heart is not being sought; rather, the goal is to determine a signal which provides the best correlation with the true heart motion so that it can be used as an external surrogate for binning list-mode acquisitions.

4.3.B Testing methodology to select the initial parameters of the BW model

Table 4.3 summarizes the correlation coefficient results for the 12 subjects in the testing set with respect to the Navigator determined heart motion for the abdomen signal, the chest signal, the Average-Area algorithm ($BW_{Average\text{-}Area}$) and the exhaustive search ($BW_{Exhaustive\text{-}Search}$). The extent of hysteresis (*H*) and pattern categorization are also shown. Note that in all cases shown in this table, the signal from the $BW_{Exhaustive\text{-}Search}$ provided the largest or tied for largest correlation coefficient. Although the *r* values from the $BW_{Exhaustive\text{-}Search}$ were higher than those of the $BW_{Average\text{-}Area}$ and the abdomen signals, the difference was statistically insignificant ($p = 0.43$ and $p = 0.24$, respectively). There was a significant difference between the chest signal and the $BW_{Exhaustive\text{-}Search}$ ($p = 0.0001$), and the $BW_{Average\text{-}Area}$ ($p = 0.0005$) signals. This indicates that usage of solely the chest signal to bin cardiac list-mode data is not a good choice. The average correlation of the $BW_{Average\text{-}Area}$ signal was larger than that of the signal from the abdomen markers, but this was not statistically significant ($p = 0.69$).

Table 4.3 Correlation coefficient (*r*) between the Navigator determined true heart motion and the signal from the abdomen, chest, BW model using the set of initial parameters selected through Average-Area algorithm ($BW_{Average\text{-}Area}$) and Exhaustive search algorithm ($BW_{Exhaustive\text{-}Search}$). The extent of hysteresis, *H*(%) and the pattern categorization are also shown.

Subject #	Correlation Coefficient (*r*)				*H* (%)	Pattern
	Abdomen	Chest	$BW_{Avg\text{-}Area}$	$BW_{Exhaustive\text{-}Search}$		
1	0.96	0.90	0.97	0.97	7	Monotonic
2	0.91	0.90	0.95	0.95	8	Monotonic
3	0.97	0.93	0.98	0.99	14	Monotonic
4	0.93	0.71	0.89	0.94	38	Hysteretic
5	0.98	0.68	0.97	0.99	43	Hysteretic
6	0.81	0.80	0.85	0.87	7	Monotonic
7	0.96	0.93	0.97	0.97	30	Hysteretic
8	0.96	0.96	0.98	0.98	17	Monotonic
9	0.96	0.95	0.96	0.98	14	Monotonic
10	0.92	0.93	0.93	0.97	2	Monotonic
11	0.95	0.88	0.95	0.97	18	Monotonic
12	0.97	0.94	0.97	0.97	17	Monotonic
Mean ± SD	0.94 ± 0.05	0.88 ± 0.09	0.95 ± 0.04	0.96 ± 0.03		

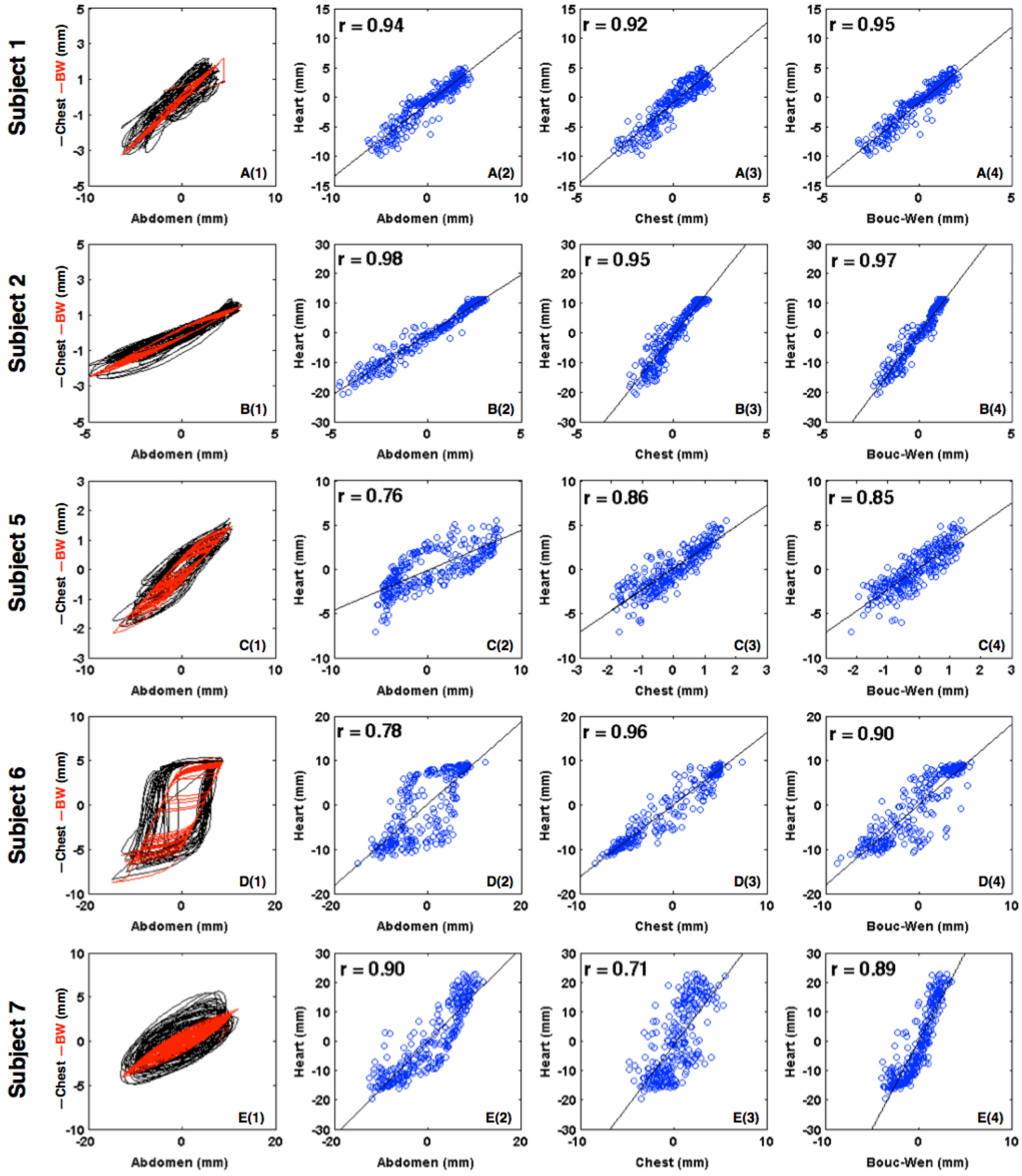

Figure 4.9 Pair-wise scatter plots of external, BW model derived, and internal Navigator measured signals for five of the seven subjects from the training set. First column: external chest marker (AP) and BW derived signals versus abdomen marker signal (AP). Second column: Navigator-determined internal heart motion (SI) versus abdomen marker signal. Third Column: internal heart motion versus chest marker signal. Fourth Column: internal heart motion versus BW derived signal. In each case the correlation coefficient (*r*) is indicated for the columns 2-4.

4.4 Discussion

We used experimental respiratory signals acquired from subjects to test the proposed BW model in estimating the heart position over different respiratory hysteretic patterns. The possible reasons for hysteresis are due to the complex and intricate interplay between the diaphragm and intercostal muscles responsible for inspiration and expiration. Furthermore, it is believed that the viscoelastic nature of the lungs [17] and internal imbalances in lung pressure [36] also play a part in retarding the motion of the heart mimicking the delayed periodic motion as observed in a forced damped oscillation [37].

This study used the true heart motion from the MRI navigator data to select the initial parameter set and test the BW model estimations of the heart motion. In general, for both monotonic and hysteretic cases, the response of the BW model based on the correlation values (*r*) accurately captured the trends of respiration in all the subjects. The respiratory motion from the external markers and the BW signals showed a good correlation with the heart motion. However, from the examples seen in Figure. 9, one cannot rely on the chest or the abdomen marker alone for amplitude binning due to the effects of hysteresis. For example, in our limited number of studies we observed that the chest marker performed better in some cases while the abdomen marker performed better in other cases in estimating the heart motion. This is an undesirable situation to estimate the heart motion with just a single surrogate signal. For instance, if amplitude binning was to be performed on the respiratory signal obtained from the abdomen marker (hysteretic) corresponding to Fig. 9D, the middle bins would inherit motion in the range of 15 to 20 mm resulting in residual blurring of the images corresponding to those bins. Such undesirable effects can be overcome to some extent by applying a suitable model with the information from both the thoracic and abdomen regions as we demonstrated in this study using the BW model.

Having known the true heart motion from the navigator data, we were able to determine the initial parameter value sets suitable for the BW model that describe a monotonic or a hysteretic behavior in estimating the heart motion. The results from the proposed Average-Area algorithm on the testing set demonstrate the potential of the Bouc-Wen model in accounting for either monotonic or hysteretic respiratory patterns in a brief amount of computational time.

4.5 Conclusion

The Bouc-Wen model has been used to describe, and predict the responses of nonlinear systems to transient inputs due to its ability to incorporate and reproduce a wide range of real cases of hysteretic behavior. To the best of our knowledge, this study introduces a novel approach in estimating the heart motion using the Bouc-Wen model applied to respiratory signals from the external body markers. The results of our study suggest that the proposed model may serve as a unified framework for modeling hysteresis seen in respiratory motion of the heart, and perhaps other organ systems, Future work will include simulations and clinical SPECT studies of image reconstruction using the Bouc-Wen model to improve the estimation of the heart motion.

Acknowledgement

This work is a continuation of investigations previously reported at the 2012 IEEE Nuclear Science Symposium and Medical Imaging Conference as: Dasari P, Konik A, Shazeeb MS, King MA. Accounting for the hysteresis of respiratory motion of the heart in cardiac SPECT and PET using the Bouc-Wen model of hysteresis. Proceedings of 2012 IEEE Nuclear Science Symposium and Medical Imaging Conference, MIC15-53, pp 3030-3032, 2012.

This work was supported by the National Institute of Biomedical Imaging and Bioengineering (NIBIB) under grant R01 EB001457 and a grant from Philips Healthcare. The contents are solely the responsibility of the authors and do not necessarily represent the official views of the NIBIB or Philips Healthcare. The authors would also like to thank Dr. Kai-Rong Qin and Dr. Cheng Xiang for their valuable assistance in modeling by sharing their code.

4.6 References

[1] C. Liu, L. A. Pierce, 2nd, A. M. Alessio, and P. E. Kinahan, "The impact of respiratory motion on tumor quantification and delineation in static PET/CT imaging," *Phys Med Biol,* vol. 54, pp. 7345-62, Dec 21 2009.

[2] A. S. Beddar, K. Kainz, T. M. Briere, Y. Tsunashima, T. Pan, K. Prado*, et al.*, "Correlation between internal fiducial tumor motion and external marker motion for liver tumors imaged with 4D-CT," *International Journal of Radiation Oncology Biology Physics,* vol. 67, pp. 630-638, 2/1/ 2007.

[3] R. A. Dvorak, R. K. J. Brown, and J. R. Corbett, "Interpretation of SPECT/CT Myocardial Perfusion Images: Common Artifacts and Quality Control Techniques," *Radiographics,* vol. 31, pp. 2041-2057, November 1, 2011 2011.

[4] D. Visvikis, O. Barret, T. Fryer, A. Turzo, F. Lamare, C. Cheze le Rest*, et al.*, "A posteriori respiratory motion gating of dynamic PET images," in *Nuclear Science Symposium Conference Record, 2003 IEEE*, 2003, pp. 3276-3280 Vol.5.

[5] D. Papathanassiou, S. Becker, R. Amir, B. Menéroux, and J.-C. Liehn, "Respiratory motion artefact in the liver dome on FDG PET/CT: comparison of attenuation correction with CT and a caesium external source," *European Journal of Nuclear Medicine and Molecular Imaging,* vol. 32, pp. 1422-1428, 2005/12/01 2005.

[6] T. S. Pan, C. Mawlawi, S. A. Nehmeh, Y. E. Erdi, D. S. Luo, H. H. Liu*, et al.*, "Attenuation correction of PET images with respiration-averaged CT images in PET/CT," *Journal of Nuclear Medicine,* vol. 46, pp. 1481-1487, Sep 2005.

[7] A. Konik, J. Kikut, R. Lew, K. Johnson, and M. A. King, "Comparison of methods of acquiring attenuation maps for cardiac SPECT in the presence of respiratory motion," *J Nucl Cardiol,* vol. 20, pp. 1093-107, Dec 2013.

[8] Y. E. Erdi, S. A. Nehmeh, T. Pan, A. Pevsner, K. E. Rosenzweig, G. Mageras*, et al.*, "The CT Motion Quantitation of Lung Lesions and Its Impact on PET-Measured SUVs," *Journal of Nuclear Medicine,* vol. 45, pp. 1287-1292, August 1, 2004 2004.

[9] L. Boucher, S. Rodrigue, R. Lecomte, and F. Benard, "Respiratory gating for 3-dimensional PET of the thorax: Feasibility and initial results," *Journal of Nuclear Medicine,* vol. 45, pp. 214-219, Feb 2004.

[10] S. A. Nehmeh, Y. E. Erdi, T. Pan, E. Yorke, G. S. Mageras, K. E. Rosenzweig*, et al.*, "Quantitation of respiratory motion during 4D-PET/CT acquisition," *Medical Physics,* vol. 31, pp. 1333-1338, Jun 2004.

[11] O. Guivarc'h, A. Turzo, D. Visvikis, and Y. Bizais, "Synchronization of pulmonary scintigraphy by respiratory flow and by impedance plethysmography," pp. 1166-1175, 2004.

[12] J. R. Olsen, W. Lu, J. P. Hubenschmidt, M. M. Nystrom, P. Klahr, J. D. Bradley*, et al.*, "Effect of novel amplitude/phase binning algorithm on commercial four-dimensional computed tomography quality," *International Journal of Radiation Oncology Biology Physics,* vol. 70, pp. 243-52, Jan 1 2008.

[13] A. F. Abdelnour, S. A. Nehmeh, T. Pan, J. L. Humm, P. Vernon, H. Schoder*, et al.*, "Phase and amplitude binning for 4D-CT imaging," *Phys Med Biol,* vol. 52, pp. 3515-29, Jun 21 2007.

[14] M. Dawood, F. Buther, N. Lang, O. Schober, and K. P. Schafers, "Respiratory gating in positron emission tomography: A quantitative comparison of different gating schemes," *Medical Physics,* vol. 34, pp. 3067-3076, Jul 2007.

[15] W. Lu, P. J. Parikh, J. P. Hubenschmidt, J. D. Bradley, and D. A. Low, "A comparison between amplitude sorting and phase-angle sorting using external respiratory measurement for 4D CT," *Med Phys,* vol. 33, pp. 2964-74, Aug 2006.

[16] J. Dey, W. P. Segars, P. H. Pretorius, R. P. Walvick, P. P. Bruyant, S. Dahlberg*, et al.*, "Estimation and correction of cardiac respiratory motion in SPECT in the presence of limited-angle effects due to irregular respiration," *Medical Physics,* vol. 37, pp. 6453-6465, Dec 2010.

[17] K. Nehrke, P. Bornert, D. Manke, and J. C. Bock, "Free-breathing cardiac MR imaging: Study of implications of respiratory motion-initial results," *Radiology,* vol. 220, pp. 810-815, Sep 2001.

[18] I. Burger and E. M. Meintjes, "Elliptical subject-specific model of respiratory motion for cardiac MRI," *Magnetic Resonance in Medicine,* vol. 70, pp. 722-731, Sep 2013.

[19] P. Dasari, K. Johnson, J. Dey, C. Lindsay, M. S. Shazeeb, J. M. Mukherjee*, et al.*, "MRI Investigation of the Linkage Between Respiratory Motion of the Heart and Markers on Patient's Abdomen and Chest: Implications for Respiratory Amplitude Binning List-Mode PET and SPECT Studies," *IEEE Transactions on Nuclear Science,* vol. 61, pp. 192-201, 2014.

[20] J. M. Blackall, S. Ahmad, M. E. Miquel, J. R. McClelland, D. B. Landau, and D. J. Hawkes, "MRI-based measurements of respiratory motion variability and assessment of imaging strategies for radiotherapy planning," *Physics in Medicine and Biology,* vol. 51, pp. 4147-4169, Sep 7 2006.

[21] P. C. M. Chi, P. Balter, D. S. Luo, R. Mohan, and T. S. Pan, "Relation of external surface to internal tumor motion studied with cine CT," *Medical Physics,* vol. 33, pp. 3116-3123, Sep 2006.

[22] D. Ruan, J. A. Fessler, J. M. Balter, R. I. Berbeco, S. Nishioka, and H. Shirato, "Inference of hysteretic respiratory tumor motion from external surrogates: a state augmentation approach," *Physics in Medicine and Biology,* vol. 53, pp. 2923-2936, Jun 7 2008.

[23] J. E. McNamara, P. H. Pretorius, K. Johnson, J. M. Mukherjee, J. Dey, M. A. Gennert*, et al.*, "A flexible multicamera visual-tracking system for detecting and correcting motion-induced artifacts in cardiac SPECT slices," *Medical Physics,* vol. 36, pp. 1913-1923, 05/00/ 2009.

[24] H. Fayad, T. Pan, O. Pradier, and D. Visvikis, "Patient specific respiratory motion modeling using a 3D patient's external surface," *Medical Physics,* vol. 39, pp. 3386-3395, 06/00/ 2012.

[25] A. Visintin, *Differential Models of Hysteresis* vol. 111. Berlin: Springer-Verlag, 1994.

[26] O. Jinhyoung and D. S. Bernstein, "Semilinear Duhem model for rate-independent and rate-dependent hysteresis," *IEEE Transactions on Automatic Control,* vol. 50, pp. 631-645, 2005.

[27] I. D. Mayergoyz and G. Friedman, "Generalized Preisach model of hysteresis," *Magnetics, IEEE Transactions on,* vol. 24, pp. 212-217, 1988.

[28] M. Ismail, F. Ikhouane, and J. Rodellar, "The Hysteresis Bouc-Wen Model, a Survey," *Archives of Computational Methods in Engineering,* vol. 16, pp. 161-188, Jun 2009.

[29] J. R. Fayçal Ikhouane, *Systems with Hysteresis: Analysis, Identification and Control Using the Bouc-Wen Model*, 1 ed.: Wiley-Interscience, 2007.

[30] Y. K. Wen, "Method for Random Vibration of Hysteretic Systems," *Journal of the Engineering Mechanics Division-Asce,* vol. 102, pp. 249-263, 1976.

[31] J. Hu, K. R. Qin, C. Xiang, and T. H. Lee, "Modeling of Hysteresis in Gene Regulatory Networks," *Bulletin of Mathematical Biology,* vol. 74, pp. 1727-1753, Aug 2012.

[32] K. R. Qin and X. A. Cheng, "Hysteresis modeling for calcium-mediated ciliary beat frequency in airway epithelial cells," *Mathematical Biosciences,* vol. 229, pp. 101-108, Jan 2011.

[33] M. A. King, J. Dey, K. Johnson, P. Dasari, J. M. Mukherjee, J. E. McNamara*, et al.*, "Use of MRI to assess the prediction of heart motion with gross body motion in myocardial perfusion imaging by stereotracking of markers on the body surface," *Medical Physics,* vol. 40, pp. -, 2013.

[34] R. L. Ehman and J. P. Felmlee, "Adaptive technique for high-definition MR imaging of moving structures," *Radiology,* vol. 173, pp. 255-63, Oct 1989.

[35] J. A. Nelder and R. Mead, "A Simplex-Method for Function Minimization," *Computer Journal,* vol. 7, pp. 308-313, 1965.

[36] D. A. Low, P. J. Parikh, W. Lu, J. F. Dempsey, S. H. Wahab, J. P. Hubenschmidt*, et al.*, "Novel breathing motion model for radiotherapy," *International Journal of Radiation Oncology Biology Physics,* vol. 63, pp. 921-9, Nov 1 2005.

[37] E. Gutiérrez and C. Paulotto, "Delay Correlation of Mechanical Hysteresis and Damping," *Journal of Structural Engineering,* vol. 136, pp. 76-85, 2010/01/01 2009.

Chapter 5 - Correction of Hysteretic Respiratory Motion in SPECT Myocardial Perfusion Imaging

Paul Dasari [a,b], P. Hendrik Pretorius [a,b], Arda Konik [a,b], Mohammed S. Shazeeb [a,b],
K. Johnson [a] W. Paul Segars [c] and Michael A. King [a]
[a] Department of Radiology, University of Massachusetts Medical School, Worcester
[b] Department of Biomedical Engineering, Worcester Polytechnic Institute, Worcester
[c] Department of Radiology Carl E. Ravin Advanced Imaging Laboratory, Duke University Medical Center Durham, North Carolina

Part of this work was presented at the 2013 annual meeting of the Society of Nuclear Medicine and Molecular Imaging, Vancouver, British Columbia, Canada and at the 12th International Meeting on Fully Three-Dimensional Image Reconstruction in Radiology and Nuclear Medicine, Lake Tahoe, California, 2013.

Manuscript in Progress

Abstract—The objective of this study is to investigate the effects of hysteretic respiratory motion (RM) and assesses the effectiveness of using the Bouc-Wen (BW) model in correcting it in ^{99m}Tc-Sestamibi myocardial perfusion SPECT (MPS). Simulated phantoms and patient scans were used in this study. 4-D NCAT phantoms were used in simulating three types of respiratory patterns, namely monotonous, mild-hysteresis, and strong hysteresis with normal and perfusion defects in the anterior, lateral, inferior and septal locations of the mid-ventricular wall. Noise-free SPECT projections simulated using an analytical projector were then added with Poisson noise to generate noisy realizations. The VTS, BW and heart respiratory signals synchronized with the projections were used independently to generate respiratory bin projection sets. Ten clinical scans were performed using a ^{99m}Tc-Sestamibi protocol while recording the respiratory signals from the thoracic and abdomen regions using a Visual Tracking System (VTS). The VTS, BW, and heart respiratory signals synchronized with the simulated projections were used independently to generate respiratory bin projection sets in phantom studies, while the VTS and the BW respiratory signals synchronized with listmode data were used independently to generate respiratory bin projection sets in clinical studies. A segmentation-registration process was used to determine the extent of motion between the respiratory bins. This extent of motion was further inversely applied to the binned projections for correction of the respiratory motion and reconstructed using the OSEM algorithm. The process was applied to the phantom and patient studies. The efficiency of the correction was assessed through Polar map

analysis. In the phantom studies, correction performed using the hysteresis corrected BW signal demonstrated closer representations to the images corrected using the “true” heart respiratory signal in comparison to VTS respiratory signals. Statistically, the BW model provided a statistically better correction for the phantom studies with strong hysteresis over other respiratory signals when compared to monotonic and mild-hysteretic patterns. The corrected clinical images were more uniform when compared with images before correction. The slices and polar maps of clinical scan demonstrated qualitative and quantitative differences between the VTS abdomen signal and the hysteresis corrected BW signal. The true accuracy of the correction was unknown due to the lack of a ground truth measure in these clinical studies. Hysteretic occurring in respiration during MPI SPECT affects the quality and accuracy of RM corrected perfusion image. Hysteresis in respiration can be corrected using the proposed method. The degree of correction primarily depends on the patient respiratory pattern and the extent of hysteresis, which may be of clinical significance in certain cases and modalities with high spatial resolution.

5.1. Introduction

Respiratory motion (RM) during image acquisition causes artifacts that can affect the clinical diagnosis in myocardial SPECT images. Conventional respiratory correction methods make use of respiratory signals from external surrogates (e.g., tracking an external marker, a pneumatic bellow on the abdomen, or spirometer) [1, 2] based on the assumption that there exists a consistent relationship between the signals and internal heart motion. However, studies have demonstrated that patients can exhibit respiratory hysteresis, wherein the heart takes different trajectories during the inspiratory and the expiratory phases of the respiratory cycle [3, 4]. Such internal behavior suggests that prediction of the heart motion from a single parameter (such as the respiratory signal related to abdominal motion) may not sufficiently provide the information about the true motion trajectory of the heart. Motion correction methods used in RM compensation essentially bin the emission scans according to the respiratory signal from the external tracking device. Binning can be performed in one of the two ways: phase-based or amplitude-based. The amplitude-based RM correction methods have been determined to perform better than the phase-based methods by capturing the depth of breathing [5-9]. However, both binning methods fail to account for respiratory hysteresis leading to inherent residual blurring in the final image.

We have previously investigated the correlation between the internal organs and the external markers with respiration [4]. Results from this study indicate that the hysteretic behavior of the heart can be predicted using a model based on more than one source of external respiratory information. Current methods accounting for hysteresis are done either by separating the respiratory signal into inspiration and expiration phases [8, 10], or by fitting ellipses [11, 12], or state augmentation techniques [13]. These methods have been primarily used in estimating lung tumor locations. However, employing the aforementioned methods often requires either a shape prior, short pre-scans, or phase-offsets to construct an accurate model to predict the internal position. These methods are limited in application for extended imaging times due to changes in the subject's respiratory pattern in terms of phase and magnitude within and between the respiratory cycles. Furthermore, the efficiency of the motion correction method in estimating the extent of respiratory motion will be limited when separately done on the inspiration and expiration data due to low counts present, resulting in images with poor signal-to-noise ratio (SNR).

In Chapter 4 we investigated a method for correcting respiratory hysteresis using the Bouc-Wen (BW) model without the need for shape prior, pre-scans, or phase-offsets. The model uses first-order non-linear differential equations for accounting the hysteretic phenomenon occurring between the inspiration and expiration phases at the same time accounting for the variations occurring within and between the respiratory cycles. The effects of RM on image uniformity, and defect-detection have been comprehensively investigated through simulations [9, 14-16] and clinical settings [17, 18] in myocardial perfusion imaging (MPI) studies. However, to the best of our knowledge, there is no previous report in the literature on the effects of respiratory hysteresis on image uniformity, quantitation and defect-detection in MPI studies. The presence of hysteresis in cardiac RM can induce residual motion into the respiratory bins that are formed according to the amplitude of the respiratory signal; the effect of residual motion on the MPI images is image blurring and hence decreased image contrast.

The working hypothesis of the study reported here suggests that the quality of the MPI studies affected by respiratory hysteresis can be improved following its correction using the BW model. Accordingly, the objective of this study was twofold: first, to evaluate the impact of respiratory hysteresis on MPI images when amplitude-based motion correction is performed and, second, to evaluate the performance of the amplitude-based motion correction when hysteresis compensated respiratory signal obtained through the BW model is employed. In the previous study [reference here], the use of the BW model in correcting respiratory hysteresis was described in detail, and thus not discussed in detail herein. In the studies reported herein the effects of respiratory hysteresis and its correction on MPI images were evaluated using both anthropomorphic digital phantom simulations and clinical studies. The RM in the simulation studies was based on recordings of internal organs (superior-inferior direction) in free-breathing volunteers using the navigator technique during MRI imaging. The MRI imaging was synchronized with acquisition anterior-posterior motion of external markers measured via a Visual Tracking System (VTS) [4]. The simulations were used to investigate under controlled conditions with known truth the impact of

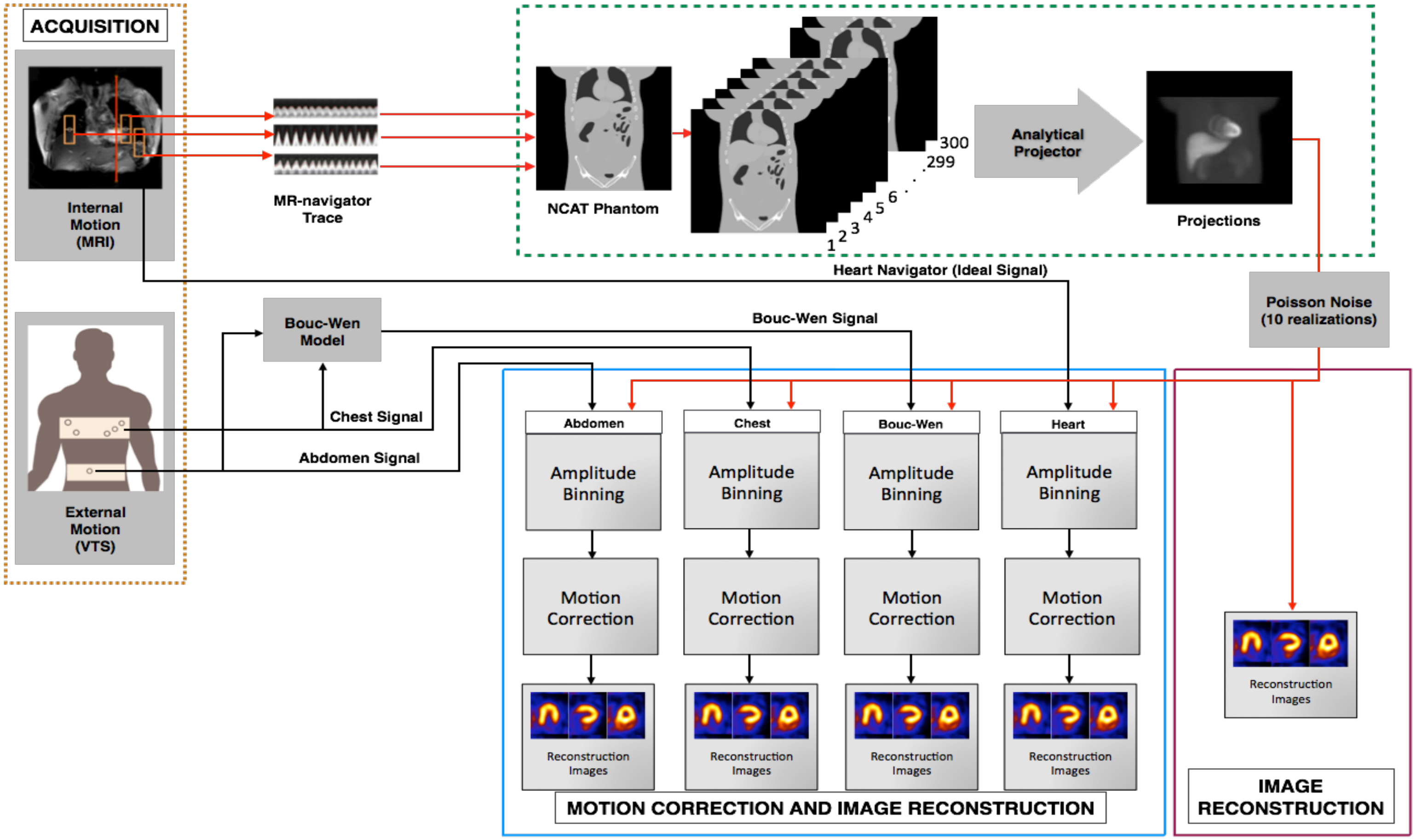

Figure 5.1 Schematic diagram illustrates the simulation process. Simultaneous acquisition of internal (MR-Navigator) and external (VTS) motion data from free-breathing volunteers was employed to generate NCAT phantoms simulating SPECT MPI imaging with realistic organ RM, and correct for it by employing the external respiratory signals in amplitude based motion correction strategies. The performance of each respiratory signal employed in RM correction algorithm is then assessed through reconstructed image.

hysteresis on respiratory motion correction strategies. An overview of this process is illustrated in Figure 5.1. Polar map based quantitative analysis of the RM correction methods was done on both the phantom and clinical data to evaluate the effects of respiratory hysteresis and its correction on MPI images.

5.2. Materials and Methods

5.2.A Respiratory Signals and their acquisitions

The RM correction method used in this study employs the amplitude-based technique on a given respiratory signal. Therefore, the performance of the RM correction primarily depends on the nature of input respiratory signal used, which implies that, to obtain final images without the impact of hysteresis, one need to use a respiratory signal free from hysteresis. Table 5.1 summarizes the list of respiratory signals and the manner they are used in this study. MR-navigator technique was employed to measure the superior-inferior (SI) respiratory motion of the organs over 300 EKG-gated cardiac cycles. The respiratory traces acquired using MR-navigators served two main purposes: Firstly, as the basis for generating respiratory motion of the phantom's organs. Secondly, served as the "truth" through which the performance of the RM correction using the external respiratory signals (from the abdomen, the chest and the BW) was compared. External respiratory signals here refer to the anterior-posterior (AP) respiratory motion of the external markers placed on the abdomen and chest regions that were tracked using a Visual Tracking System (VTS)[19].

The BW signal here represents the respiratory signal derived from the BW model described in subsection 5.2.B. All respiratory signals used in this study are from our previous work [4].

Table 5.1 Respiratory signals and their usage

Source	*Respiratory Signal*	*Usage*
MRI-navigators*	Heart, Right and left Diaphragm	In creating phantom organ motion
VTS†	Chest and Abdomen† regions	In motion correction
BW Model†	BW signal	In motion correction

*Used in simulating organ respiratory motion in NCAT phantoms.

† Used in both simulation and clinical studies

5.2.B Bouc-Wen Model of Hysteresis and Hysteresis Compensation

The RM signals acquired from the chest and the abdomen regions tracked via the VTS are incorporated in the modified Bouc-Wen model, which is used to model hysteresis in estimating the heart motion. The modified BW model is expressed as following [20]

$$\dot{w} = \rho(\dot{x} + \delta\, x\, |\dot{w}| - \sigma\, |\dot{x}|\, w - \gamma\, w|\dot{w}|) \tag{5.1}$$

where, *x(t)* and *w(t)* are the anterior-posterior (AP) displacements of the abdomen and chest markers, respectively,

$|\dot{w}| = \dot{w} \cdot sgn(\dot{w}), |\dot{x}| = \dot{x} \cdot sgn(\dot{x}), \dot{w} = dw/dt\,, \dot{x} = dx/dt\,, sgn(\dot{x}) =$ $\begin{cases} -1\ if\ \dot{x} < 0 \\ 0\ if\ \dot{x} = 0 \\ 1\ if\ \dot{x} > 0 \end{cases}$, and *ρ, δ, σ,* and *γ* are the parameters that determine the shape and extent of hysteresis in the modified BW model.

Here we are interested in the variation of respiratory motion between the chest and the abdomen regions, rather than the respiratory rates. Hence, the term *dw/dx*, conveys the variation of respiratory motion between the chest and the abdomen region in (2) is derived by rearranging (1) and dividing it by the respiratory rate *dx/dt*:

$$w_{Est} = dw/dx = \rho(1 - \sigma\, w\, sgn(x))/(1 - \rho\, \delta\, x\, sgn(w) + \rho\, \gamma\, w\, sgn(w)) \qquad (5.2)$$

Using the respiratory motion signal acquired from the external VTS markers we estimate the respiratory motion of the heart using the BW model. This estimate of the respiratory heart motion is termed as Bouc-Wen (BW) signal and is used as a respiratory signal in the correction method to evaluate its success in comparison to the abdomen and chest signals.

2.5.C Phantoms

To assess the effect of respiratory hysteresis and its correction under controlled conditions, we performed analytical simulations of Tc-99m sestamibi cardiac-perfusion SPECT imaging using the 4-D NURBS-based cardiac-torso (NCAT) human anthropomorphic phantom [21]. From previous studies, RM of the heart is known to be small compared to that of the diaphragm [3, 4, 22]. Furthermore in the presence of hysteresis, the RM of the organs exhibit phase difference between each other [3, 4]. To simulate the phantom as close as possible to the realistic human studies, the NCAT phantom was specifically modified to accommodate for respiratory hysteresis observed, by allowing independent motions of the heart, liver and spleen (right and left diaphragm). The RM information from the previous study [TNS paper] obtained using the MR navigators over 300 cardiac cycles was translated into the phantom to simulate RM of the organs. The duration of respiration is about five minutes with 35-40 respiratory cycles. Since this investigation is primarily examining the effects of RM, the largest extent of motion occurs in the superior-inferior (SI) direction [3, 22, 23], therefore, the RM of the NCAT organs was modeled accordingly.

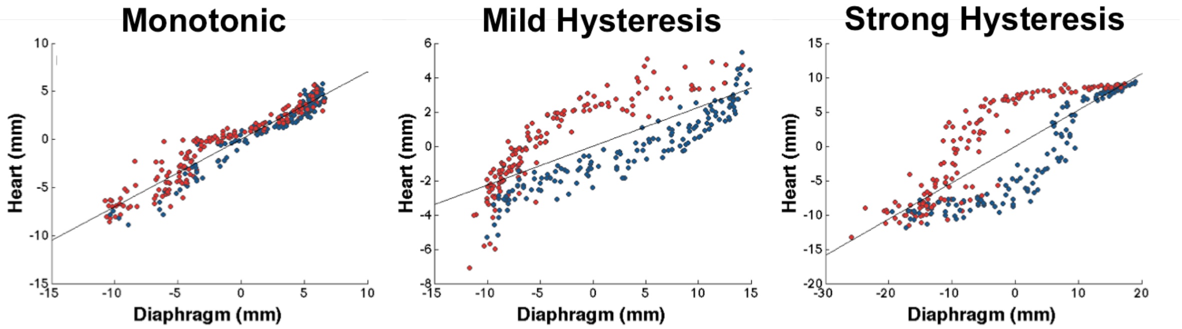

Figure 5.2 Plots for the MRI navigator measured internal motion on the heart and diaphragm for the monotonic, mild and strong hysteresis respiratory patterns simulated in the phantom studies.

Respiratory hysteresis in the phantoms were simulated for the three RM patterns, namely: i) monotonic; ii) mild-hysteresis, and; iii) strong-hysteresis with maximum extent of measured heart motion of 1.45 cm, 1.25 cm and 2.3 cm, respectively. Figure 5.2. shows the three types respiratory patterns used in this simulation study. For each pattern, 300 NCAT phantoms (matrix size: 256×256×256 and voxel size: 0.23 cm) each representing a second in time were generated; each phantom is unique in its organ displacements proportional to the navigator signal representing an instant in the RM of the organs measured. Thus creating a “breathing” phantom for a period of five minutes. In addition, the cardiac motion due to beating heart was modeled based on the average of 16 time frames. The anatomy of the phantoms used for the three different patterns remained the same.

For each of the three RM patterns, the phantom data were classified into two kinds on the basis of myocardial abnormality namely: a) Normal and b) Perfusion Defect phantoms.

Normal phantoms represent the healthy condition of heart and were used in comparing the effects of hysteresis and its correction using the respiratory signals for the three RM patterns in terms of the measure of respiratory motion estimates and the mean uniformity of short axis slices of myocardial wall.

Perfusion defect phantoms, as the name suggests represent the abnormal condition of the heart with perfusion deficits on the left ventricular wall. Perfusion defect phantoms were created by defining myocardial perfusion defects in NCAT phantoms as independent volumes, which were then subtracted from normal NCAT phantoms. Myocardial perfusion defects were simulated on the mid anterior (A), lateral (B), inferior (C), and septal (D) regions of the left ventricle wall. The size of the lesions was 60° in the circumferential dimension and 3 cm in the longitudinal direction with contrast of 50% uptake reduction compared to normal wall uptake.

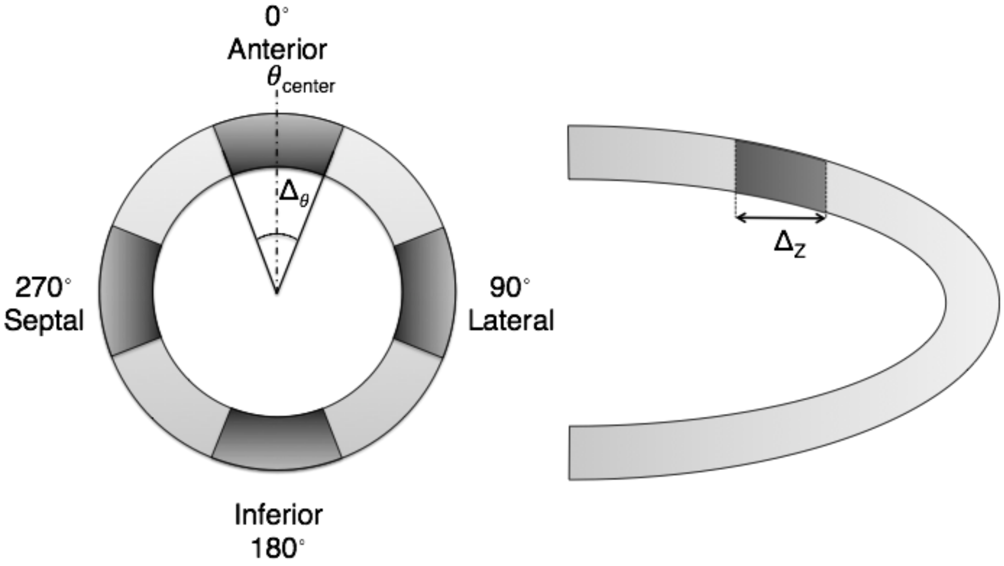

Figure 5.3 Schematic illustrations showing the short-axis (left) and long-axis (right) views of the left ventricle wall. The shaded areas represent the locations of the perfusion defects simulated on the anterior ($\theta_{center} = 0^o$), lateral ($\theta_{center} = 90^o$), inferior ($\theta_{center} = 180^o$), and septal ($\theta_{center} = 270^o$) walls with defect span (Δ_θ) $= 60^o$, and defect size (Δ_Z) $= 3\ cm$.

Figure 5.3 shows the schematics illustrating the defect locations on the left ventricle in short-axis and long axis views. These phantoms with perfusion defects were used to evaluate how accurately the defects were represented in presence of respiratory hysteresis. Figure 5.4 summarizes the manner in which the phantoms were simulated to evaluate the effect of respiratory hysteresis and its correction.

5.2.D Projection Data

For each phantom, Poisson noise fluctuations were added to generate 10 noise realizations prior to the simulation of the acquisition process. Projection data was simulated from 4D NCAT phantoms using an analytical projector [24], modeling attenuation (without scatter effect) and distance-dependent collimator blurring (low energy high resolution - LEHR). Sixty projections (radius of rotation: 25 cm) were obtained covering 180^o around each NCAT phantom, from 45° right anterior-oblique to 45° left posterior-oblique, simulating a dual head cardiac SPECT acquisition in the presence of respiration. Then, the 256×256×60 projection data were resized to 128×128×60 and scaled to ~7 million total counts to match the noise level of a ^{99m}Tc-Sestamibi cardiac SPECT study. With this set-up, unlike the variation seen in patient breathing, the 300 NCAT respiratory states were repeated for every projection angle due to the limited number of respiratory samples.

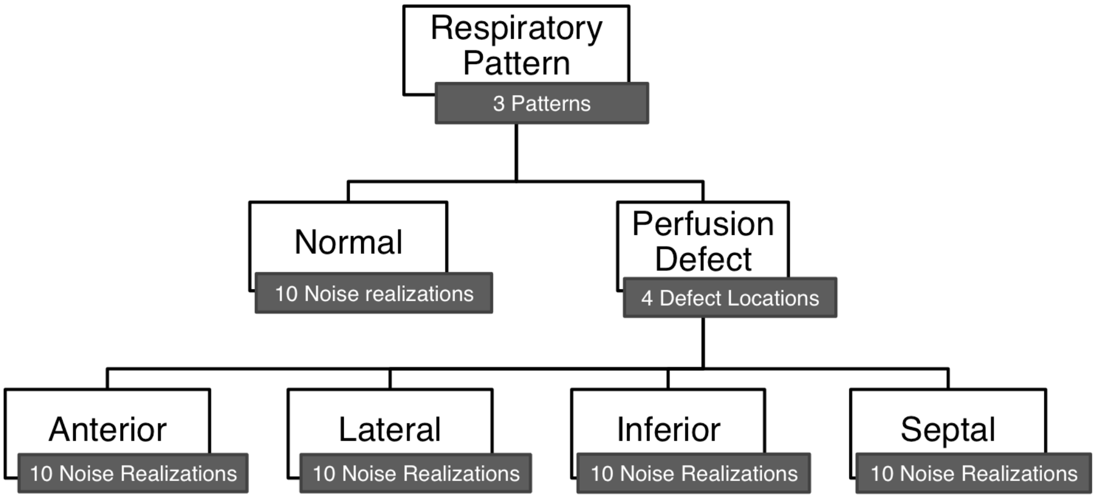

Figure 5.4 Schematic block diagram illustrating the experimental design of the simulation study. The simulations were performed for the three different respiratory patterns. Each respiratory pattern was simulated for a healthy heart (Normal) and a heart with perfusion abnormality (Perfusion Defects). Perfusion deficits were simulated separately in the mid anterior, lateral, inferior and septal regions of the left ventricle.

5.2.E Patient Data

Ten myocardial perfusion imaging (MPI) SPECT acquisitions were used in this study. A list mode Stress cardiac gated ^{99m}Tc-Sestamibi protocol was performed. The following parameters were used: 128 X 128 matrix, 60 projections, angular range of 180°, pixel size of 6.8 mm. CT-based attenuation maps were used for attenuation correction. The respiratory signals from the chest and the abdomen regions were recorded by motion-tracking the external markers using the VTS system. The list-mode SPECT data were then separated into amplitude bins using the compensated signal. The respiratory bins were generated as described earlier. The image reconstructions free from respiratory motion were obtained by employing the methods discussed in sections 5.2.F and 5.2.G.

5.2.F Amplitude binning of list-mode Phantom and Patient data

Amplitude binning: The listmode data from simulation and clinical studies were retrospectively binned into projections of different respiratory states according to the amplitude of the respiratory signal used. The amplitude of the respiratory signal was divided into odd number (7 for clinical and 9 for simulation studies) of bins with uniform intervals between the global maximum (corresponding to the end inspiration) and global minimum (corresponding to the end expiration),

Phantom Data: The amplitude binning of the simulation data was performed independently for the four different respiratory signals obtained from: 1) the external chest marker; 2) the external abdomen marker; 3) the BW model using both chest and abdomen markers, and; 4) the MRI heart navigator (ideal). The performance of the signals from the external markers and the BW model were compared against the ideal signal.

Patient Data: The Amplitude binning on the patient data was performed independently for the two different respiratory signals: 1) the external abdomen marker and 2) the BW model.

5.2.G Data Processing

RM correction was performed by using the algorithm described in [9], the projections were summed at each amplitude bin for each projection angle. For each projection angle, projections whose respiratory state fell in the same interval were summed to produce nine (seven for patient data) summed projections for that angle, one for each of the total intervals of the amplitude of respiratory signal. The summed projection in the middle respiratory bin was considered as the reference state, and the projections in the remaining bins were considered as motion states. The respiratory motion estimates were obtained by registering the motion states to the reference state. The motion estimates were computed as averages for each of the respiratory amplitude bin. These motion estimates were then incorporated in the Ordered Subset Expectation-Maximization (OSEM) algorithm [25] with attenuation correction, resolution recovery and motion compensation to generate a RM corrected by use of 5 iterations of OSEM followed by application of a post-reconstruction 3D Gaussian filter with an SD of 1 cm. For the clinical and phantom OSEM reconstructions 15 and16 subsets (4 angles per subset) were used accordingly. Attenuation correction in phantom studies was performed using the attenuation map with respiratory motion averaged over 300 NCAT phantoms for each of the three respiratory patterns.

In addition to the RM corrected reconstructions, the projections were reconstructed without motion correction using the OSEM algorithm. This formed the uncorrected reconstruction dataset, which were used in comparing the RM corrected reconstructions.

Reconstruction results for each dataset were reformatted into short and long axes slices and were assessed by generating polar map images. In-house software, CardiacApp was used to obtain the left ventricle regional uptake and quantified using a 17 segment polar map [26]. A normal polar map was generated using the reconstructions corresponding to the middle bins from the three respiratory patterns. The smoothing was performed on polar maps before final presentation and quantitative analysis.

5.2.H Data Analysis

Phantom Data

Normal phantoms: The reconstruction results of the normal phantoms between different respiratory signals were assessed based on the correlation of the respiratory motion estimates and the uniformity of the polar-maps. A Spearman rank-order correlation coefficient (ρ) [27] was computed as a non-parametric measure of the strength and the direction of association of the respiratory motion estimates between the test respiratory signals and the ideal signal (“truth”). The motion estimates were computed as averages over all ten noise-realizations and all nine respiratory amplitude bins. Scatter plots were used illustrate the correlation of the test respiratory signals with the true heart motion. In addition, side-by-side box-plots were used for each respiratory signal to compare the extent of heart motion (residual blur) present in each respiratory amplitude bin.

The uniformity of the polar maps was calculated using the circumferential count profiles (2° per step) produced by the short axis slices. The uniformity is the measure of variation in mean counts over all short axis slices from apex-to-base [28, 29]. It was calculated according to the equation.

$$Uniformity_{Apex-Base} = 100\times\left(\frac{\sum_{i=1}^{n}\{(MAX_{Slice} - MIN_{Slice})/(MAX_{Slice} + MIN_{Slice})\}_i}{n}\right) \quad (5.3)$$

where n is the total number of short axis slices, MAX_{Slice} and MIN_{Slice} are the maximum and minimum counts in the n^{th} slice. Theoretically, a uniform short axis slices would result a uniformity value of zero. Polar maps of noiseless phantoms were used to assess the uniformity.

Perfusion defect phantoms: The effects of respiratory hysteresis in studies with perfusion defects were assessed by comparing the differences in the polar maps obtained by the respiratory signals used in correction. The polar maps were normalized to their highest activity. The presence of motion causes image blurring leading to loss in contrast, which implies decreased intensity and decreased area of the true intensity values. Therefore, intensity and area of the defects in the phantom's myocardial wall were measured in the polar maps to study the severity and extent of the defects respectively for each of the three respiratory patterns. The values of defect intensity and area were measured for the all the respiratory signals used in RM correction and were compared against the values obtained by the ideal signal. Defect intensity and area are reported in terms of percent errors.

Intensity calculation was done within a region of interest (ROI) defined around the defect. Absolute differences between the polar maps of the ideal signal and the test signals were normalized by the ideal signal as calculated in (4). The differences were divided by the polar map of the ideal signal on pixel-by-pixel basis within the ROI to calculate the errors in intensity and reported as percentages.

$$\%Error_{Intensity} = 100\times(|ROI\ Intensity_{Ideal} - ROI\ Intensity_{Test}|/ROI\ Intensity_{Ideal}) \qquad (5.4)$$

where $ROI\ Intensity_{Ideal}$ and $ROI\ Intensity_{Test}$ are the intensity values within the defined ROI corresponding to the polar maps of the ideal and the test signals respectively.

To measure the extent of defects, blackout polar maps were generated. The area of the blackout pixels in blackout polar maps defines the area of the defect. A blackout pixel in this study is defined as having an intensity value with 2.5 standard deviations below the mean of a normal database. Percent error for defect area was computed as the absolute difference between the area of the defect measured in the blackout polar map of the ideal signal and the area of the defect measured in the blackout polar maps of the test signals divided by the area of the defect measured in the blackout polar map of the ideal signal.

$$\%Error_{Area} = 100\times(|Area_{Ideal} - Area_{Test}|/Area_{Ideal}) \tag{5.5}$$

where $Area_{Ideal}$ and $Area_{Test}$ are the of the areas of the blackout pixels corresponding to the polar maps of the ideal and the test signals respectively. The percent errors for both the defect intensity and area were computed as averages over the ten noise-realizations. A paired student's t-test with Bonferroni correction was applied at 95 % confidence interval to assess the results between the respiratory signals. A *p*-value of less than 0.05 was considered as statistically significant. The above analysis was simultaneously performed on the motion-averaged images without motion correction, to provide a measure against the motion-corrected results using different respiratory signals.

Patient Data

The effect of respiratory hysteresis and its correction in clinical studies was assessed visually based on the short and vertical long-axes emission images, and the corresponding polar maps; and quantitatively by comparing the following parameters for each patient study.

- The extent of heart motion: the extent of heart motion in the axial direction was calculated by measuring the difference of the motions estimated in the end-states by the amplitude-based RM correction algorithm. The extent of heart motion as estimated by the algorithm using the abdomen and the hysteresis corrected BW signals are compared. A paired *t*-test was used to evaluate the RM estimating ability of the abdomen and the BW signals.
- Global differences in polar maps: global differences between the polar maps of the uncorrected and corrected reconstructions, and between the polar maps of the corrected reconstructions were measured. The corrected reconstructions were obtained using the abdomen marker and the BW model signals independently.
- Regional uptake changes in the polar maps: Regional changes in the polar maps of the uncorrected and corrected reconstructions were quantified and compared by calculating the (Anterior + Inferior)/(Lateral + Septal) wall ratios [30].

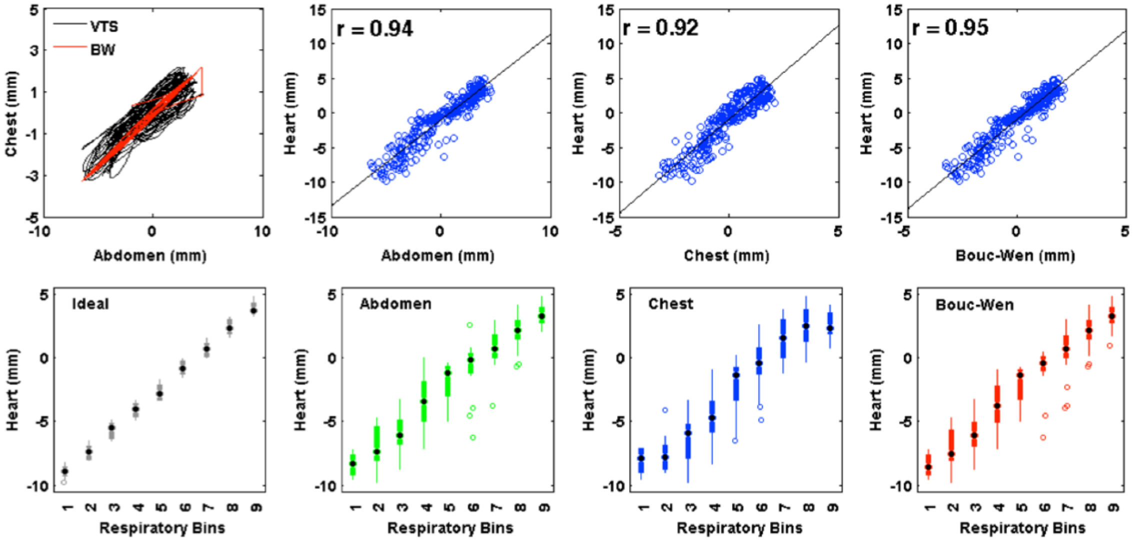

Figure 5.5 show the scatter (top row) and side-by-side box plots (bottom row) for the monotonic respiratory pattern. The scatter plots and side-by-side box plots summarize the relationship of the respiratory signals with the true heart motion and the residual extent of heart motion present in each respiratory signal amplitude bin, respectively.

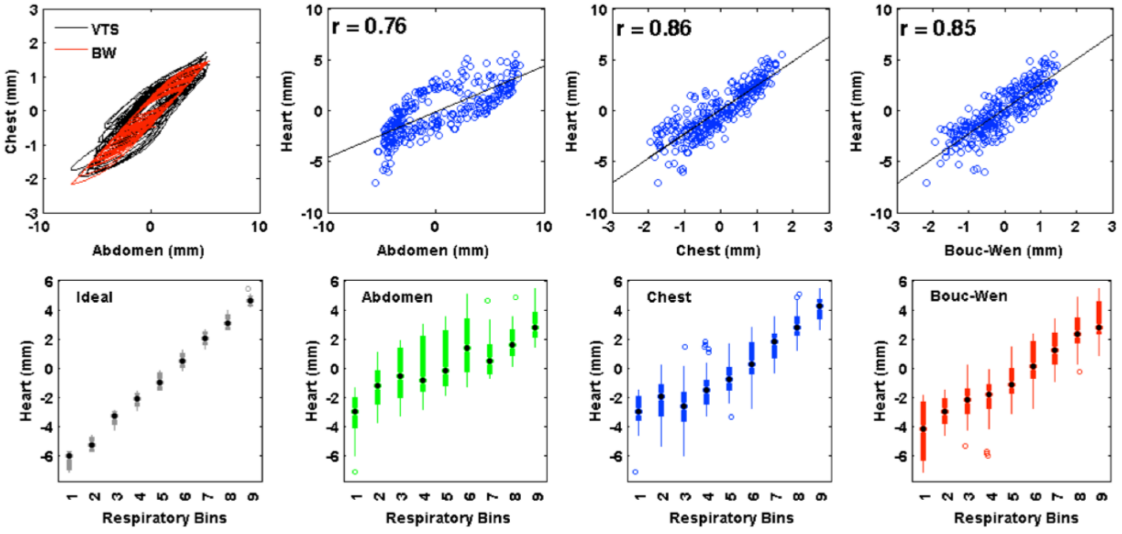

Figure 5.6 show the scatter (top row) and side-by-side box plots (bottom row) for the mild-hysteretic respiratory pattern. The scatter plots and side-by-side box plots summarize the relationship of the respiratory signals with the true heart motion. The box plots for the Bouc-Wen signal shows comparatively small residual motion in the respiratory bins compared to those of the Abdomen signal

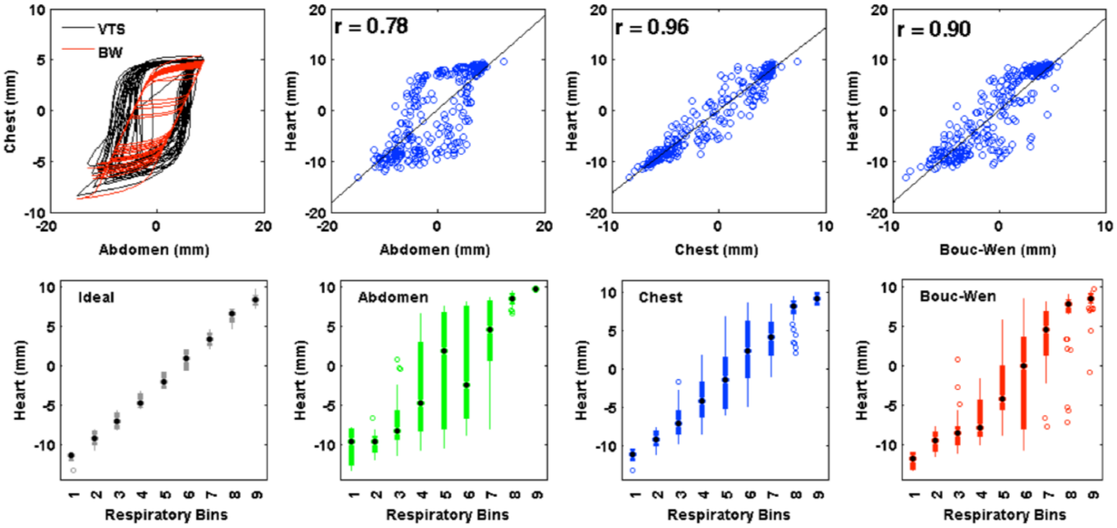

Figure 5.7 show the scatter (top row) and side-by-side box plots (bottom row) for the strong-hysteretic respiratory pattern. Comparing the middle respiratory bins in box plots for the Abdomen and Bouc-Wen signals, a substantial decrease of residual motion is noted upon correcting for hysteresis using the Bouc-Wen signal.

5.3 Results

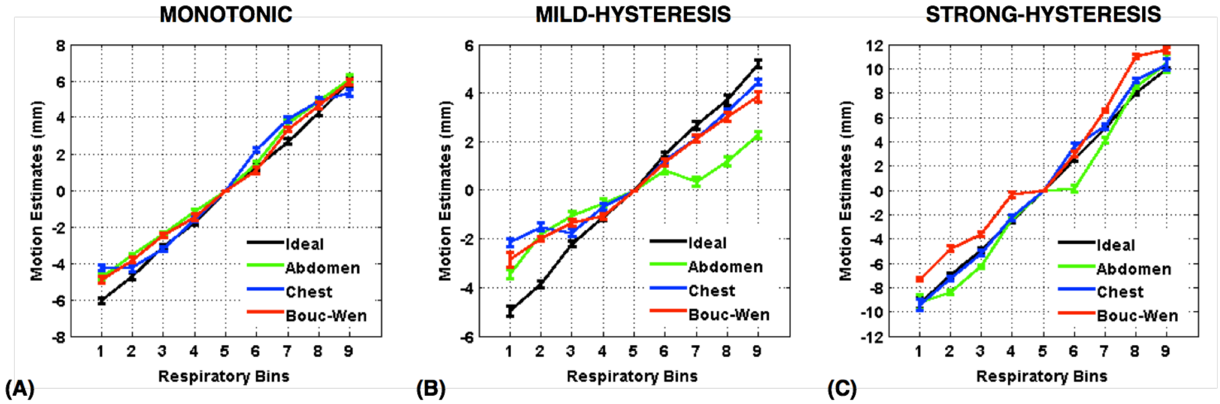

Figure 5.8 Plots (A-C) summarize the respiratory motion estimates by registration to the reference bin (bin 5) for monotonic, mild and strong hysteretic respiratory patterns obtained from the motion-correction/reconstruction algorithm using the respiratory signals from the abdomen, chest, the BW model and the heart navigator (ideal) on the phantom studies.

Phantom Data

Normal phantoms: In Figure 5.5-5.7: The scatter plots (top row) show the correlation between the AP motion of the external chest and abdomen markers, the SI motion of internal heart motion w.r.t the AP motion of the external abdomen marker, chest marker and the BW mode for the monotonic, mild and strong hysteretic respiratory patterns. The side-by-side box plots (bottom row) show the extent of heart motion present in each respiratory bin after performing amplitude binning on each respiratory signal for the monotonic, mild and strong hysteretic respiratory patterns. The medians in the boxplot approximately correspond to the respiratory motion estimates as determined by the registration algorithm.

Figure 5.8(A-C) shows the motion estimates for the respiratory signals used in motion correction of normal phantoms for the three different hysteretic patterns and ten noise realizations. It is seen that the motion estimates follow a similar trend as that of the medians in boxplots shown in Figures 5.5-5.7. The motion estimates from the test respiratory signals show good correlation with the ideal signal. Though the motion estimates of the test signals are close to the estimates of the ideal signal, the residual motion is concealed within each bin. This is especially true and exaggerated in the presence of hysteresis.

Figure 5.9(A-C) presents the polar maps of the normal phantoms together with respective apex-base uniformity values for the three hysteretic patterns. The uniformity of the polar maps is influenced by both the extent of motion and the efficiency of the motion correction method. Significant artifacts in the anterior and inferior walls can be seen with increase in the depth of respiration in correcting for it. This is more apparent in the polar maps without motion correction. The use of motion correction in general resulted in better uniformity compared to the uncorrected. The polar maps corresponding to linear pattern with 1.5 cm extent of motion shown in Figure 5.9(A) resulted in the best uniformity. The corresponding uncorrected polar map showed artifacts primarily in the inferior wall. The polar maps presented in Figure 5.9(B) correspond to mild-hysteretic pattern with 1.0 cm (approx.) extent of motion shows very good uniformity, on careful observation of the uncorrected polar map, very mild artifact is present in the inferior wall indicating that when the extent of motion is small in the presence of hysteresis it would not result in significant motion artifacts. The polar maps shown in Figure 5.9(C) correspond to strong-hysteretic pattern with 2.1 cm (approx.) extent of motion illustrating the effect of large extent of motion in combination with hysteresis. The polar map without motion correction shows a poor uniformity with severe artifacts in the anterior and inferior wall region while the polar maps with motion correction using all signals showed better uniformity. The presence of large residual motion (approx. 1-1.5 cm) in the middle respiratory bins of the abdomen signal (as shown in Figure 5.7 box-plots) causes the intensities in the polar map to be more uniform and is noticed in the corresponding polar map as a loss of apical cooling. The effects of residual motion due to respiratory hysteresis are suppressed in the due to the high-count density and low contrast in the phantoms without noise and defects.

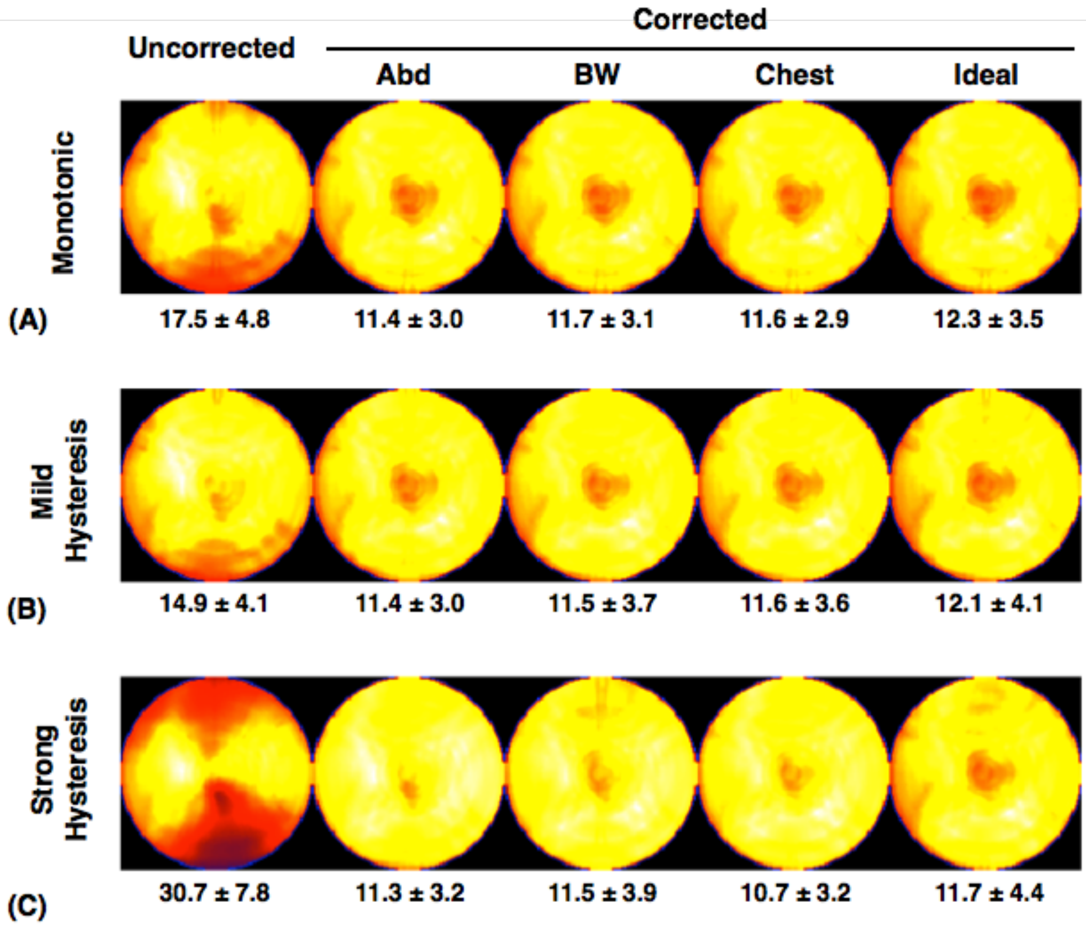

Figure 5.9 Panels A, B and C consists of polar maps for monotonic, mild and strong hysteretic respiratory patterns from the normal heart phantom reconstructions. Polar maps of the uncorrected and corrected reconstructions for the respiratory signals: abdomen (Abd), chest, the BW model (BW) and the heart navigator (Ideal) are shown. Uniformity values for the corresponding polar maps are given as mean ± SD. Note: apical cooling is expected in the NCAT phantom due to thinning of the wall in this location.

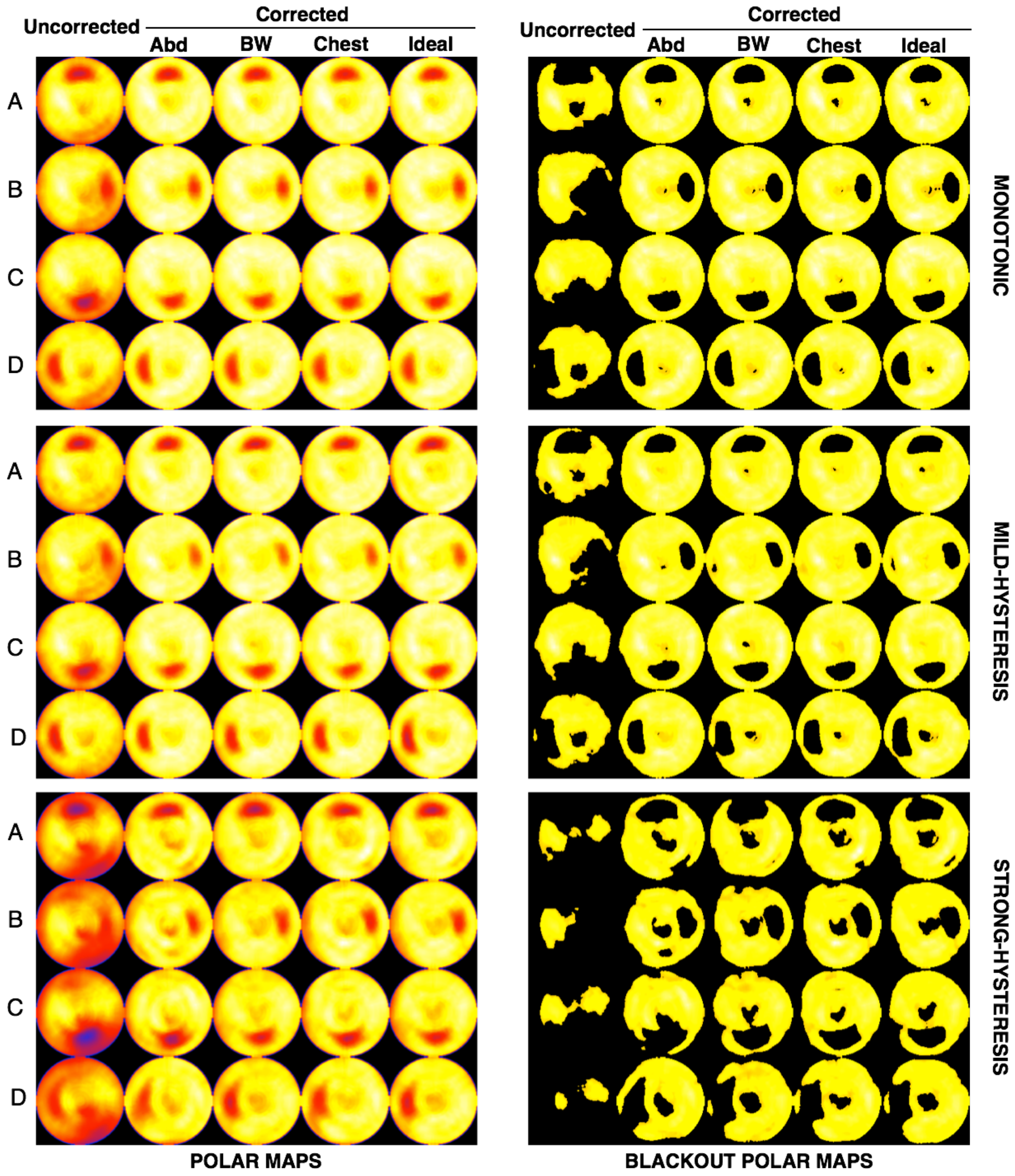

Figure 5.10 An example of one noise-realization summarizing polar maps and blackout polar maps of the perfusion defect phantoms for each of the three respiratory patterns and the four defect locations (A, B, C and D) is shown. Polar maps of uncorrected and corrected reconstructions for the respiratory signals: abdomen (Abd), chest, the BW model (BW) and the heart navigator (Ideal) used in motion correction algorithm are shown along with the corresponding blackout polar maps obtained by perfusion quantification. Defect intensity and area quantification was performed using the polar maps from all ten noise-realizations.

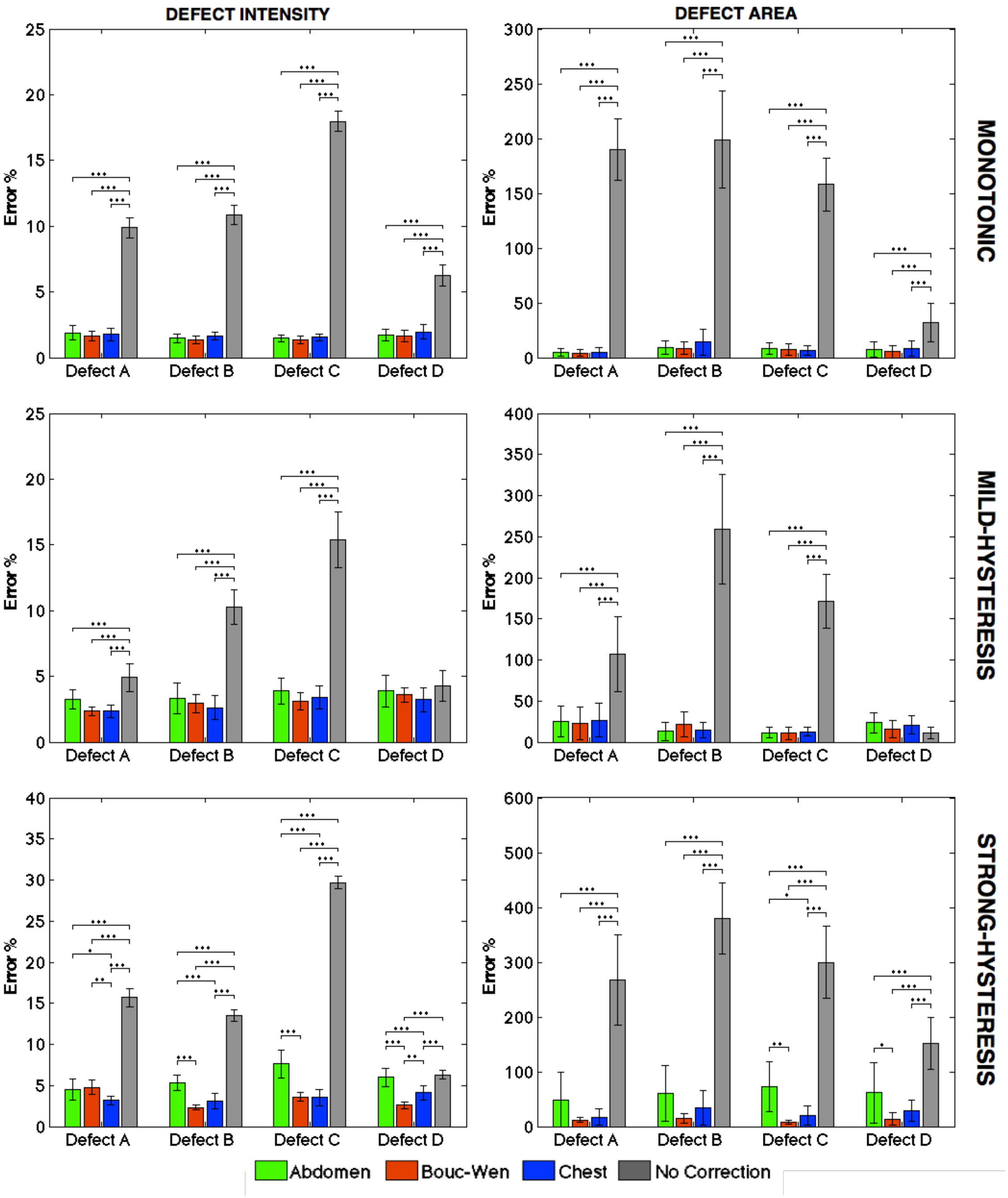

Figure 5.11 The defect intensity and defect area (expressed as percent errors) in the uncorrected and corrected reconstructions using the respiratory signals from the abdomen, chest and the BW model for the four defect locations. Results are shown for the monotonic, mild and strong hysteretic respiratory patterns. The calculated errors are significantly different with * p < .05, ** p < .01, *** p<0.001 by Paired Student's t-test with Bonferroni correction.

Perfusion defect phantoms: Figure 5.10 shows the polar maps and blackout polar maps respectively for the three respiratory patterns, one noise realization and all four defects. Figure 5.11 summarizes the results of defect intensity and area analysis of the perfusion defect studies in terms of percentage error with statistical comparisons between the uncorrected and corrected sets for each of the three respiratory patterns and the four defect locations. The errors in the correction methods for all respiratory patterns and defect locations with one exception being defect D (septal wall) in mild-hysteretic pattern was significantly lower than in the uncorrected. Although the errors for intensity and areas corresponding to the chest and the BW signals were smaller compared to the abdomen signal no statistical significance was found between them for all defect locations in the monotonic and mild hysteretic respiratory patterns. For the strong hysteretic pattern the errors resulting from using the chest and the Bouc-Wen signals in RM correction was smaller compared to that of the abdomen signal. Statistically significant differences in errors of defect intensity and area between the abdomen and the BW signals were found in defect locations B, C and D; and C and D respectively. This suggests that the effect of respiratory hysteresis is more pronounced with large amplitude respiration and use of hysteresis corrected respiratory signal decreases the error in estimating the heart motion and accurate defect representation.

Patient Data

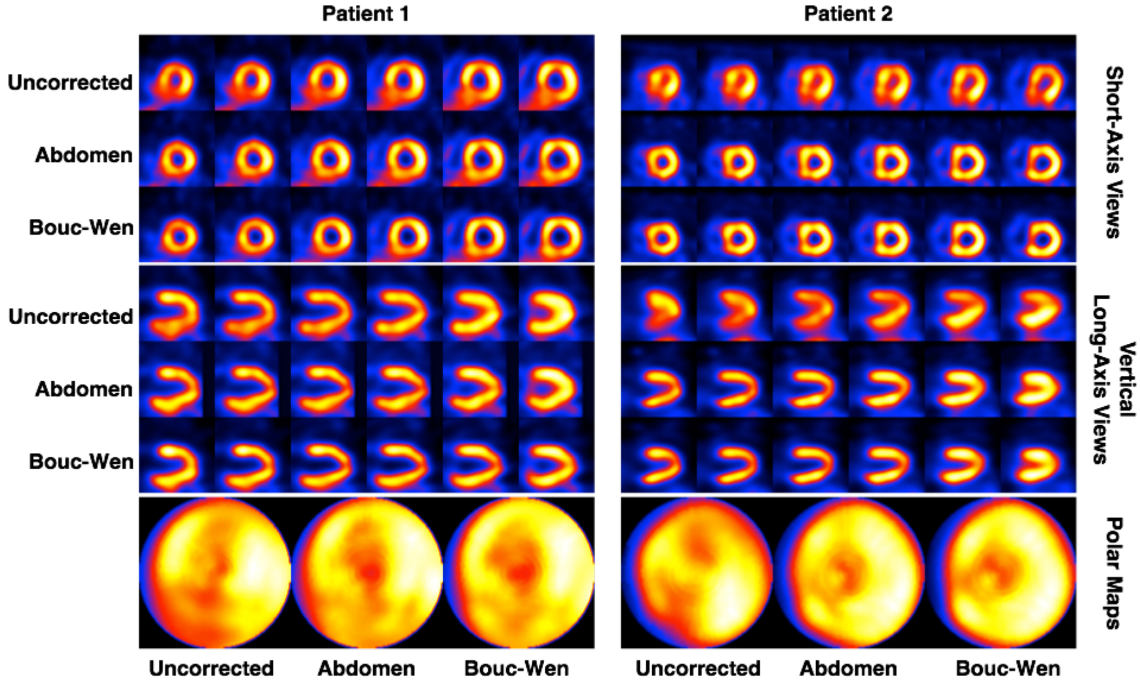

Figure 5.12 Short axis slices (top), vertical long axis slices (middle), and polar maps (bottom) of 99mTc-sestamibi stress scans for two patients without and with RM correction using the abdomen and the BW signals are shown.

In the clinical studies, a considerable variation in the extent of heart motion due to respiration ranging from 1 to 2.4 cm in the axial direction was observed. 4 out of 10 patients exhibited respiratory hysteresis in the order of mild-hysteretic pattern while the rest exhibited monotonic pattern. Figure 5.12 displays the short axis view, vertical long axis view, and polar maps of two clinical cases in which the extent of respiratory heart motion estimated by both the abdomen and the BW signals was greater than 2 cm. The effect of respiratory motion correction is well pronounced in both the corrected reconstructions using the abdomen and BW signals as compared to the uncorrected.

Minor differences suggestive of a better correction in the quality of the reconstructed slices between the BW signal and correction employing solely the abdominal marker data were noted visibly. The degree of improvement in these images depended on a variety of factors such as extent of RM, extent of respiratory hysteresis, the number of counts in motion states, and system resolution for SPECT imaging.

Figure 5.13 presents the results for the extent of heart motion estimated in axial direction for the abdomen and BW signals, global differences, and regional uptake changes in the polar maps of the uncorrected and corrected reconstructions in the ten patient studies. Figure 5.13(A) outlines the extent of heart motion in the axial as estimated by the algorithm before correction. The respiratory signals from the abdomen and the BW model showed no significant differences in estimating the extent of heart motion (p= 0.73). Global differences (Figure 5.13(B)) between the polar maps of the uncorrected and the abdomen and BW signal corrected reconstructions were greater compared to the differences between the corrected reconstructions using the abdomen and BW signals. The results of the global differences were comparable to the extent of heart motion. The larger the extent of heart motion the greater the differences between the uncorrected and corrected sets as has been observed in other studies [9, 18]. Figure 5.13(C) presents the regional uptake changes as a ratio of (Anterior + Inferior)/(Lateral + Septal) walls. The uncorrected polar maps had reduced ratio compared to the corrected polar maps due to the presence of RM. The ratios for the corrected polar maps using the Abdomen and BW resulted in similar ratios.

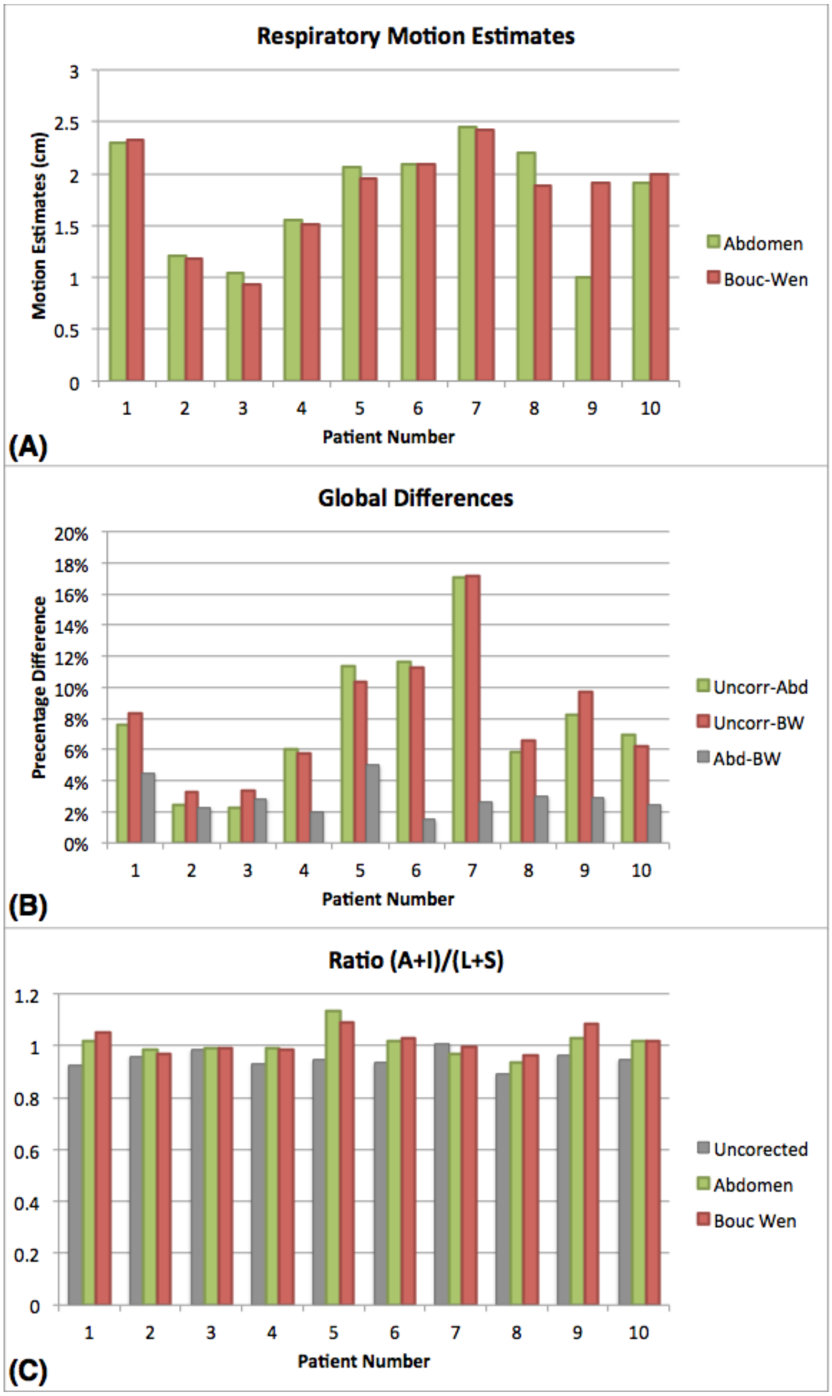

Figure 5.13 (A-C). shows the corresponding results for the extent of heart motion estimated in axial direction using the abdomen (Abd) and Bouc-Wen (BW) signals, global differences, and regional uptake changes in the polar maps of the uncorrected(Uncorr) and corrected reconstructions using the abdomen and BW signals for ten patient studies.

5.4 Discussion

Anatomical changes in the thoracic region due to respiration causes myocardial motion resulting in deteriorated MPI-SPECT images. The study was designed to assess the effect of respiratory hysteresis and its correction using the BW model by validating it in phantom simulations, and evaluating it on the clinical MPI-SPECT studies. The simulations reflect a broad range of respiratory characteristics both in terms of the extent of axial motion and the extent of hysteresis.

Current results of the simulation study indicate that the artifacts stemming from simulated respiratory hysteresis are more pronounced with increased depth of respiration. The effect of respiratory hysteresis on the uniformity between the uncorrected and corrected sets was smaller for the monotonic and mild-hysteretic (Figure 5.9 (A), (B)) and greater for the strong hysteretic patterns.

In the corresponding polar maps of the simulated perfusion defect phantoms, the differences between the uncorrected and corrected sets were larger for the hysteresis corrected BW respiratory signal compared to the use of abdomen respiratory signal, mainly in the anterior, lateral, and inferior wall of the NCAT phantom (Figure 5.11). For the mild-hysteretic pattern, the effect of correcting respiratory hysteresis using the BW signal resulted in slightly smaller errors in representing the perfusion defects compared to the those corrected using the abdomen signal but not statistically different. The residual RM as observed in the middle respiratory bins of the abdomen signal (Figure 5.7 (boxplots)) is an undesirable effect which causes image blurring and loss of contrast resulting in inaccurate representation of perfusion defects despite the RM correction, this supposition is supported by the quantitative measurements (Figure 5.11). The signal from the chest marker performed very well in comparison to the signals from the abdomen and the BW model in all the three respiratory patterns. However, the magnitude of chest signal is low thus more susceptible to body motion. Relying on either the abdomen or chest marker signals can lead to erroneous results. Thus the use of a model like BW is beneficial by combining the information from the chest and the abdomen regions.

In clinical studies, the RM correction performed using the signal obtained through the BW model was compared to that correction using the abdomen signal. The abdomen signal was used as the reference respiratory signal for patient data since the respiratory signal from the abdomen region is widely used in clinical setting. Therefore, the comparative analysis of the patient data was performed for the reconstructions corrected using the abdomen and the BW respiratory signals.

Our evaluation is based on visual observations of the emission images, and quantitative assessments of the polar maps. Patient cases showed significantly larger differences between uncorrected and corrected reconstructions. The quantitative measurements of the polar maps were found to be in good agreement with our visual observations. The differences measured in the quantitative analysis between the corrected reconstructions using the abdomen and the BW signals were consistent with the qualitative visual analysis. There was a strong indication that either correction improves the ratio in the direction one would expect with correction, and that there are small differences between abdomen and BW. The effects of respiratory hysteresis depends on patient's respiratory pattern and may be of clinical significance with smaller magnitude of respiratory motion when effective image resolution is improved.

5.5 Conclusion

Through realistic simulations of Tc-99m sestamibi MPI SPECT data, we have studied the effects of respiratory hysteresis and its correction using the BW model. It was found that in the presence of hysteresis, using a respiratory signal with hysteresis correction in image reconstruction resulted in consistently better results than the signal without hysteresis correction (abdomen signal). The effect of respiratory hysteresis and its correction depends on the subject's respiratory pattern and the depth of breathing. In our limited set of clinical studies, a minor impact of this method is observed in the reconstructed slices of patients studied thus far, primarily due to the patient's respiratory pattern. A study of a larger population of patients in which clinical truth as to disease presence would be needed to determine if there is any clinically significant difference between with and without correction, or the two correction methods.

5.6 References

[1] D. A. Low, M. Nystrom, E. Kalinin, P. Parikh, J. F. Dempsey, J. D. Bradley*, et al.*, "A method for the reconstruction of four-dimensional synchronized CT scans acquired during free breathing," *Medical physics (Lancaster),* vol. 30, p. 1254, 2003.

[2] B. W. Reutter, G. J. Klein, K. M. Brennan, and R. H. Huesman, "Acquisition and automated 3-D segmentation of respiratory/cardiac-gated PET transmission images," *IEEE Nuclear Science Symposium conference record (1997),* vol. 2, pp. 1357-1361, 1996.

[3] K. Nehrke, P. Bornert, D. Manke, and J. C. Bock, "Free-breathing cardiac MR imaging: Study of implications of respiratory motion-initial results," *Radiology,* vol. 220, pp. 810-815, Sep 2001.

[4] P. Dasari, K. Johnson, J. Dey, C. Lindsay, M. S. Shazeeb, J. M. Mukherjee*, et al.*, "MRI Investigation of the Linkage Between Respiratory Motion of the Heart and Markers on Patient's Abdomen and Chest: Implications for Respiratory Amplitude Binning List-Mode PET and SPECT Studies," *IEEE Transactions on Nuclear Science,* vol. 61, pp. 192-201, 2014.

[5] W. Lu, P. J. Parikh, J. P. Hubenschmidt, J. D. Bradley, and D. A. Low, "A comparison between amplitude sorting and phase-angle sorting using external respiratory measurement for 4D CT," *Med Phys,* vol. 33, pp. 2964-74, Aug 2006.

[6] M. Dawood, F. Buther, N. Lang, O. Schober, and K. P. Schafers, "Respiratory gating in positron emission tomography: A quantitative comparison of different gating schemes," *Medical Physics,* vol. 34, pp. 3067-3076, 07/00/ 2007.

[7] A. F. Abdelnour, S. A. Nehmeh, T. Pan, J. L. Humm, P. Vernon, H. Schoder*, et al.*, "Phase and amplitude binning for 4D-CT imaging," *Phys Med Biol,* vol. 52, pp. 3515-29, Jun 21 2007.

[8] J. R. Olsen, W. Lu, J. P. Hubenschmidt, M. M. Nystrom, P. Klahr, J. D. Bradley*, et al.*, "Effect of novel amplitude/phase binning algorithm on commercial four-dimensional computed tomography quality," *International Journal of Radiation Oncology Biology Physics,* vol. 70, pp. 243-52, Jan 1 2008.

[9] J. Dey, W. P. Segars, P. H. Pretorius, R. P. Walvick, P. P. Bruyant, S. Dahlberg*, et al.*, "Estimation and correction of cardiac respiratory motion in SPECT in the presence of limited-angle effects due to irregular respiration," *Medical Physics,* vol. 37, pp. 6453-6465, Dec 2010.

[10] D. A. Low, P. J. Parikh, W. Lu, J. F. Dempsey, S. H. Wahab, J. P. Hubenschmidt*, et al.*, "Novel breathing motion model for radiotherapy," *International Journal of Radiation Oncology Biology Physics,* vol. 63, pp. 921-9, Nov 1 2005.

[11] I. Burger and E. M. Meintjes, "Elliptical subject-specific model of respiratory motion for cardiac MRI," *Magn Reson Med,* Oct 8 2012.

[12] D. Ruan, J. A. Fessler, and J. M. Balter, "Mean position tracking of respiratory motion," *Med Phys,* vol. 35, pp. 782-92, Feb 2008.

[13] D. Ruan, J. A. Fessler, J. M. Balter, R. I. Berbeco, S. Nishioka, and H. Shirato, "Inference of hysteretic respiratory tumor motion from external surrogates: a state augmentation approach," *Physics in Medicine and Biology,* vol. 53, pp. 2923-2936, Jun 7 2008.

[14] W. P. Segars, S. P. Mok, and B. M. Tsui, "Investigation of Respiratory Gating in Quantitative Myocardial SPECT," *IEEE Trans Nucl Sci,* vol. 56, pp. 91-96, Feb 1 2009.

[15] A. Bitarafan-Rajabi, H. Rajabi, F. Rastgou, and A. A. Sharafi, "Effect of respiratory motion on quantitative myocardial gated SPECT: a simulation study," *Ann Nucl Med,* vol. 23, pp. 587-93, Aug 2009.

[16] Y. W. Yang, J. C. Chen, X. He, S. J. Wang, and B. M. Tsui, "Evaluation of Respiratory Motion Effect on Defect Detection in Myocardial Perfusion SPECT: A Simulation Study," *IEEE Trans Nucl Sci,* vol. 56, pp. 671-676, Jun 1 2009.

[17] A. Pourmoghaddas, R. Klein, R. A. deKemp, and R. G. Wells, "Respiratory phase alignment improves blood-flow quantification in Rb82 PET myocardial perfusion imaging," *Med Phys,* vol. 40, p. 022503, Feb 2013.

[18] G. Kovalski, O. Israel, Z. Keidar, A. Frenkel, J. Sachs, and H. Azhari, "Correction of heart motion due to respiration in clinical myocardial perfusion SPECT scans using respiratory gating," *Journal of Nuclear Medicine,* vol. 48, pp. 630-636, Apr 2007.

[19] J. E. McNamara, P. H. Pretorius, K. Johnson, J. M. Mukherjee, J. Dey, M. A. Gennert*, et al.*, "A flexible multicamera visual-tracking system for detecting and correcting motion-induced artifacts in cardiac SPECT slices," *Medical Physics,* vol. 36, pp. 1913-1923, 05/00/ 2009.

[20] J. Hu, K. R. Qin, C. Xiang, and T. H. Lee, "Modeling of Hysteresis in Gene Regulatory Networks," *Bulletin of Mathematical Biology,* vol. 74, pp. 1727-1753, Aug 2012.

[21] W. P. Segars and B. M. W. Tsui, "Study of the efficacy of respiratory gating in myocardial SPECT using the new 4-D NCAT phantom," *Nuclear Science, IEEE Transactions on,* vol. 49, pp. 675-679, 2002.

[22] K. McLeish, D. L. G. Hill, D. Atkinson, J. M. Blackall, and R. Razavi, "A study of the motion and deformation of the heart due to respiration," *Medical Imaging, IEEE Transactions on,* vol. 21, pp. 1142-1150, 2002.

[23] N. Koch, H. H. Liu, G. Starkschall, M. Jacobson, K. Forster, Z. Liao*, et al.*, "Evaluation of internal lung motion for respiratory-gated radiotherapy using MRI: Part I—correlating internal lung motion with skin fiducial motion," *International Journal of Radiation Oncology*Biology*Physics,* vol. 60, pp. 1459-1472, 12/1/ 2004.

[24] T. Pan, D. Luo, and M. King, "Design of an efficient 3-D projector and backprojector pair for SPECT," *Proc. Fully-3D Image Reconstruction Radiol. Nucl. Med,* 1995.

[25] H. M. Hudson and R. S. Larkin, "Accelerated Image-Reconstruction Using Ordered Subsets of Projection Data," *Ieee Transactions on Medical Imaging,* vol. 13, pp. 601-609, Dec 1994.

[26] M. D. Cerqueira, N. J. Weissman, V. Dilsizian, A. K. Jacobs, S. Kaul, W. K. Laskey*, et al.*, "Standardized myocardial segmentation and nomenclature for tomographic imaging of the heart a statement for healthcare professionals from the cardiac imaging committee of the Council on Clinical Cardiology of the American Heart Association," *Circulation,* vol. 105, pp. 539-542, 2002.

[27] D. J. Best and D. E. Roberts, "Algorithm {AS} 89: The upper tail probabilities of {S}pearman's rho," *Journal of the Royal Statistical Society. Series C (Applied Statistics),* vol. 24, pp. 377-379, // 1975.

[28] G. Kovalski, Z. Keidar, A. Frenkel, O. Israel, and H. Azhari, "Correction for respiration artefacts in myocardial perfusion SPECT is more effective when reconstructions supporting collimator detector response compensation are applied," *Journal of Nuclear Cardiology,* vol. 16, pp. 949-955, 2009/12/01 2009.

[29] M. K. O'Connor, B. Kemp, F. Anstett, P. Christian, E. P. Ficaro, E. Frey*, et al.*, "A multicenter evaluation of commercial attenuation compensation techniques in cardiac SPECT using phantom models," *Journal of nuclear cardiology,* vol. 9, pp. 361-376, 2002.

[30] A. Konik, J. Kikut, R. Lew, K. Johnson, and M. A. King, "Comparison of methods of acquiring attenuation maps for cardiac SPECT in the presence of respiratory motion," *J Nucl Cardiol,* vol. 20, pp. 1093-107, Dec 2013.

Chapter 6 - Conclusions

6.1 Summary and Conclusions

The primary focus of this thesis has been on developing methods for allowing reconstruction of quantitatively accurate respiratory motion-corrected cardiac emission images. The use of SPECT emission scans to make good motion measurements for cardiac respiratory motion model is unsuitable due to the noisy nature of the data, long acquisition times, and the relatively poor spatial resolution. Method for partitioning emission scans into motion-limited bins and aligning them have been implemented by several authors. However the effects of respiratory hysteresis have not previously received as much attention, despite its correction being needed in obtaining quantitatively accurate images. The principle focus of this work was in the development of a method to overcome the problem of hysteresis to create a system that robustly corrects all forms of patient respiratory-motion with minimal impact on clinical operation. Due to the high temporal and spatial resolution of MRI, and the fact that it does not employ ionizing radiation, it was used to obtain the truth as to cardiac motion in human volunteers. The signals from the VTS were used in forming a motion model, and to apply the developed motion model in the MPI-SPECT studies.

The following section provides a summary of the investigations reported in the chapters of this dissertation.

Chapter 3: Characterization of respiratory patterns

The first stage of the project was to investigate the behavior of respiratory motion of the heart and how it correlates with external surrogates on the subject's thoracic and abdomen regions. This was done by tracking external markers on the abdomen and chest through the VTS simultaneously with MRI tracking of motion of the heart. A correlational analysis between the external and internal motion of these locations was then employed to explore the relationship between external signals and motion of the heart. Previous findings on respiratory hysteresis had been published, however these did not report on the relationship between the external and internal motions. Thus this investigation was required to understand the respiratory hysteretic phenomenon and its detection so that the subsequent project regarding the development of a method to correct for hysteresis could be directed towards correcting the effects of respiratory hysteresis in cardiac scans. It was observed that the hysteretic effect is not the characteristic of an individual but rather could manifest randomly, i.e. it not only varies between volunteers but in time (or with extent of respiration) in a given volunteer. Performing amplitude binning based respiratory motion correction in such a study would result in considerable variation in the SI location of the heart in the list-mode events placed in that bin. This would result in an incomplete correction of respiratory motion. It was also observed that the hysteretic relationship between the markers of the chest and the abdomen correlates with SI motion of the heart and the diaphragm. It is thus potentially a means to indicate the presence of hysteresis and could be useful in estimating the respiratory motion of the heart.

The focus of the investigations performed in the rest of the dissertation work was therefore in developing a method to estimate heart motion by correcting for respiratory hysteresis such that quantitatively accurate cardiac images could be achieved with subsequent motion-correction.

Chapter 4: Development of motion-model to account for respiratory hysteresis

Taking into account the observations made from Chapter 3, an approach was proposed that involved the use of the respiratory information from both the chest and the abdomen regions, along with a motion model, to account for the variations between thoracic and abdominal breathing and hence the hysteretic and irregular breathing patterns. The Bouc-Wen (BW) model of hysteresis was used as a motion model to account for hysteresis and estimate a signal related to the motion of the heart using the respiratory information from both the chest and the abdomen surrogates. The model uses first-order non-linear differential equations to account for the hysteretic phenomenon occurring between the inspiration and expiration phases, and at the same time account for the variations occurring within and between the respiratory cycles.

An initial investigation was performed using the BW model to generate a hysteresis corrected respiratory motion signal and compare the estimated motions with those previously obtained for the heart in the same set of subjects. The performance of the BW model was assessed by computing the Pearson's correlation coefficient (*r*) as the strength of association between the estimated signal (BW) and the internal motion of the heart. The correlation of the signal resulting from the BW model showed consistently strong relationship with the internal motion of the heart for a variety of respiratory patterns compared to the correlations of the abdomen and chest signals. The algorithm developed provided a valuable tool for more robust estimation of the heart motion hence improved motion correction.

Chapter 5: Correction and evaluation of respiratory hysteresis

The final stage of the overall process was assessing the effect of respiratory-hysteresis and its correction using the BW model. This was done through phantom simulations, in which case the ground-truth is known. Using simulated SPECT studies based on the NCAT phantom, the problem caused by respiratory hysteresis and the utility of the proposed method in diminishing this error is demonstrated in this chapter. The chapter illustrated the ability of the developed method to correct the effects caused by respiratory hysteresis in short-axis slices and polar maps of the NCAT phantom for cases with 1-2 cm amplitudes of respiratory motion with monotonic, mild, and strong hysteretic respiratory patterns. Qualitative and quantitative differences between hysteresis corrected and uncorrected sets were significantly larger in data with the strong hysteretic respiratory pattern than in those with monotonic and mild-hysteretic patterns. The results also indicate that the developed method correction improved the accuracy of defect representation.

In ten cardiac-perfusion patients, with respiratory motion of 1-2.5 cm, the developed method demonstrated qualitative and quantitative differences in the slices and polar maps of patient studies. The actual accuracy of the correction was unknown because it was not possible to verify due to the absence of a ground truth measure in these clinical studies.

6.2 An overview of the Developed Technique

1. Acquire an MPI-SPECT study using the list-mode option synchronized with the respiratory sensor signals from the thoracic and abdomen regions.
2. Categorize the respiratory pattern into monotonic or hysteretic based on the *H*-value (extent of hysteresis) using the respiratory signals from the chest and abdomen regions.
3. Estimate the respiratory heart motion using the BW model by applying the initial parameter value set based on the *H*-value.
4. Time bin the list-mode data to 100ms frames while retaining the synchronization with the respiratory signal
5. Bin the list-mode into respiratory interval/bins (7 or 9) according the amplitude of the respiratory signal estimated by the BW model, with middle bin considered as the reference bin.
6. Sum the frames that fell in the same bin to produce projections for each respective bin at each angle.
7. Reconstruct slice sets for each respiratory bin.

8. Perform rigid-body six-degree-of-freedom registration on the heart region between the reference bin (center) set of slices and the other sets of slices to calculate the motion estimates.
9. In a second pass through reconstruction apply the estimated motion estimates to reconstruct a single set of slices with the heart at the location of the reference bin.
10. 7.3 Summary of Significant Findings

The summary of main findings of this thesis is as follows:

- The hysteresis between the markers of the chest and the abdomen correlates with superior-inferior (SI) motion of the heart during respiration.
- The hysteretic respiratory patterns vary between respiratory cycles within and between individuals.
- The development of a method to detect respiratory hysteresis in MPI SPECT studies based on MRI investigations in volunteers where the truth as to cardiac motion can be determined.
- The development of an algorithm for correcting respiratory hysteresis in cardiac SPECT studies
- The demonstration of the effects of hysteresis and its correction through phantom simulations and clinical application.

6.3 Future Work

To broaden the scope of the work undertaken here and to achieve images with better quantitative accuracy one could improve more advanced optimization algorithms such as Particle Swarm Optimization (PSO) in the application of the BW model for each respiratory cycle to better account for hysteresis. With the availability of large number of suitable datasets and by increasing the size of the training set, it would be expected to reduce the residual errors and to make the technique applicable to a wide range of patient studies. A minimum of 27 patient studies will be required in this two-treatment crossover study. The probability is 85% that the study will detect a treatment difference at a two-sided 0.05 significance level, if the true difference between treatments is 0.85 units with the assumption that the standard deviation of the response variable is 1.

The testing of the BW model to correct for respiratory hysteresis was performed with SPECT datasets, further tests would be needed determine the effects of its application in other areas such as lung tumors which exhibit a similar hysteretic phenomenon and in imaging modalities with higher spatial resolution such as PET, MRI, CT, etc. With the advent of hybrid systems such as simultaneous PET/MR and SPECT/MR one could perform motion-correction directly using the true motion of the heart without the need for external surrogates' correlation. However, the technique developed here could provide a valuable tool for respiratory motion correction in stand-alone cardiac emission studies (SPECT or PET) with increased quantitative accuracy, which is currently unavailable in Nuclear Medicine clinics.

Appendix

Journal Publications

Paul Dasari, Karen Johnson, Clifford Lindsay, Joyoni Dey, Joyeeta Mitra Mukherjee, Member, Shaokuan Zheng, and Michael A. King. MRI Investigation of the Linkage between Respiratory Motion of the Heart and Markers on Patient's Abdomen and Chest: Implications for Respiratory Amplitude Binning List-Mode PET and SPECT Studies. *Transactions on Nuclear Science,* 61, 192-201, 2014

Paul Dasari, Arda Konik, Mohammed S. Shazeeb, Clifford Lindsay , Joyeeta M. Mukherjee , Karen L. Johnson and Michael A. King. Adaptation of the Bouc-Wen Model to Compensate for Hysteresis in Respiratory Motion for the List-mode Binning of Cardiac SPECT and PET Acquisitions: Testing using MRI. *Medical Physics* (*In Review*)

Michael A. King, Joyoni Dey, Karen Johnson, **Paul Dasari**, Joyeeta M. Mukherjee, Joseph E. McNamara, P. Hendrik Pretorius, Arda Konik, Cliff Lindsay, Shaokuan Zheng, and Dennis Coughlin. Use of MRI to Assess the Prediction of Heart Motion in Myocardial Perfusion Imaging by Stereo-Tracking of Markers on the Body Surface. *Medical Physics*, 40, 112504, 2013

Conference Proceedings

King MA, Dey J, Johnson K, **Dasari P**, Mukherjee JM, McNamara J, Pretorius PH, Konik A, Zheng S, Miro S. Use of MRI to Assess the Prediction of Heart Motion by Stereo-Tracking of Markers on the Body Surface. Proceedings of 2010 IEEE Medical Imaging Conference, M18-324, 3320-3325, 2010

Connolly CM, Konik A, **Dasari P.K.R**, Segars P, Zheng S, Johnson KL, Dey J, King MA. Creation of 3D Digital Anthropomorphic Phantoms which Model Actual Patient Non-rigid Body Motion as Determined from MRI and Position Tracking Studies of Volunteers. Proceedings of SPIE Conference 7964, pp79642G1-8, 2011

Dasari P, Johnson K, Dey J, Mukherjee JM, Zheng S, Connolly C, King MA. MRI Investigation of the Linkage between Respiratory Motion of the Heart and Markers on Patient's Abdomen and Chest: Implications for Respiratory Amplitude Binning List-Mode PET and SPECT Studies. Proceedings of 2011 IEEE Medical Imaging Conference, MIC18-106, 2011

Konik A, Connolly CM, Johnson KL, **Dasari P**, Segars WP, Pretorius PH, King MA. Digital Anthropomorphic Phantoms of Non-Rigid Human Respiratory and Voluntary Body Motions: A Tool-Set for Investigating Motion Correction in 3D Reconstruction. Proceedings of 2011 IEEE Medical Imaging Conference, MIC17-2, 2011

Lindsay C, Gennert MA, Connolly CM, Konik A, **Dasari PK**, Segars WP, King MA. Interactive Generation of Digital Anthropomorphic Phantoms from XCAT Shape Priors. Proceedings of SPIE Conference 8317-21, pp 83170M1-M10, 2012

Dasari P, Konik A, Shazeeb MS, King MA. Accounting for the hysteresis of respiratory motion of the heart in cardiac SPECT and PET using the Bouc-Wen model of hysteresis. Proceedings of 2012 IEEE Medical Imaging Conference, MIC15-53, pp 3030-3032, 2012

Dasari P, Johnson KL, Lindsay C, King MA. The effect of arm position on respiratory motion of the heart: implications for emission imaging. Proceedings of 2012 IEEE Medical Imaging Conference, MIC15-54, pp 3033-3035, 2012

Konik A, **Dasari P**, Mukherjee JM, Johnson KL, Helfenbein E, Chien S, Babaeizadeh A, Shao L, Dey J, King MA. Respiratory tracking using EDR for list-mode binning in cardiac emission tomography: comparison with MRI heart motion measurements. Proceedings of 2012 IEEE Medical Imaging Conference, MIC03-4, pp 2131-2136, 2012.

Eric Helfenbein, Cheng-hao Simon Chien, Saeed Babaeizadeh, **Paul Dasari**, Arda Könik, Joyeeta Mitra Mukherjee, Michael King, Lingxiong Shao. ECG/EMG-Derived Respiration During Cardiac Magnetic Resonance Imaging. *ISCE* 2012

Cheng-hao Simon Chien, Eric Helfenbein, Saeed Babaeizadeh, **Paul Dasari**, Arda Könik, Joyeeta Mitra Mukherjee, Michael King, Lingxiong Shao. A Comparison of Three ECG-Derived Respiration Techniques During Cardiac Magnetic Resonance Image Acquisition. *ISCE* 2012

Dasari P, Konik A, Pretorius PH, Shazeeb MS, Segars WP, Johnson K, King MA. Evaluation of Bouc-Wen model corrected respiratory motion in cardiac SPECT. Proceedings of the 12th International Meeting on Fully Three-Dimensional Image Reconstruction in Radiology and Nuclear Medicine, pp 396-399, 2013

Paul Dasari, P. Hendrik Pretorius, Arda Konik, Mohammed S. Shazeeb and Michael A. King. Correction of Hysteretic Respiratory Motion in SPECT Myocardial Perfusion Imaging. *SNM* 2013

Lindsay C, Gennert MA, Konik A, **Dasari PK**, King MA. Automatic generation of digital anthropomorphic phantoms from simulated MRI acquisitions. Proceedings of SPIE Conference 8671-74, pp 8671221-8, 2013

Rhodri L. Smith, Kevin Wells, John Jones, **Paul Dasari**, Cliff Lindsay, Michael A. king. Toward a Framework for High Resolution Parametric Respiratory Motion Modeling. *IEEE-MIC* 2013

Paul Krupaker Reddy Dasari

501 Plantation St, Apt # 610• Worcester, MA 01605
(774)-274-5357 • paulkreddy@wpi.edu

EDUCATION

Ph.D. Biomedical Engineering, Worcester Polytechnic Institute, Worcester, MA April-2014 (expected)
Thesis Title: Characterization and Compensation of Hysteretic Cardiac Respiratory Motion in Myocardial Perfusion Studies through MRI Investigations.

B.E. Biomedical Engineering, Visvesvaraya Technological University, Belgaum, India June-2007
Group Project: Cardiac Vector Display using Programmable System on Chip (PSoC).

RESEARCH EXPERIENCE

Graduate Research Assistant, Nuclear Medicine Physics Lab, Department of Radiology
University of Massachusetts Medical School, Worcester, MA December 2010 – Present

- Designed and executed MR experiments to detect hysteretic respiratory motion of the heart.
- Investigated different strategies for correcting the hysteretic respiratory patterns.
- Performed mathematical modeling using MRI data and non-linear differential equations to correct for respiratory motion in cardiac SPECT images and minimizing residual blur for better image representation.
- Designed and implemented a novel algorithm to detect and compensate hysteresis in cardiac respiratory motion using the Bouc-Wen model of hysteresis for improved image quality of the list mode emission studies.
- Performed phantom simulations to evaluate the mathematical models developed for motion correction.

Graduate Research Assistant, Advanced MRI Lab, Department of Radiology
University of Massachusetts Medical School, Worcester, MA February 2008 – November 2010

- Designed and executed experiments in detecting early lung tumors in small animals with the contrast-combination of Hyperpolarized Helium and SPIO Nano particles in Hyperpolarized Gas MRI.
- Designed and built Dual-Tuned Radio-Frequency (RF) Coils for Hyperpolarized Helium and Xenon animal MRI experiments.
- Characterization of Iron-Oxide-Nano-Particles using NMR relaxometry.
- Conducted MR imaging and spectroscopy – data acquisition and pulse sequence optimization using PHILIPS Achieva 3T MRI scanner.
- Designed and developed RF coils for various small-animal MRI experiments.
- Wrote custom MATLAB software for MR image processing, data analysis, and evaluating mathematical models; used SAS and Excel for performing statistical calculations.
- Performed maintenance and upkeep of 3T PHILIPS Achieva system.

ADDITIONAL EXPERIENCE

Teaching assistant, Department of Biomedical Engineering, WPI August 2009- May 2012

- Supervised and taught undergraduate students, adapting to different scientific levels and backgrounds, prepared the experiment instrumentation, graded their assignments and exams.

In-plant Trainee, K.L.E.S Medical Hospital and Research Centre, Belgaum, India February 2005 - March 2005

SKILLS

Computing

- Programming Languages: MATLAB (Advanced), Linux Scripting in Bash shell, C (as a part of course work), IDL, assembly language programming, Statistical Analysis using R, SAS, STATA and SPSS, SolidWorks, LABVIEW
- Platforms: Windows, Linux and Unix
- Equipment: Capable of fully operating 3T PHILIPS MRI scanners, Building RF coils for small-animal MR studies, Design of lab equipment for small-animal experiments

AWARDS

Conference Trainee Grant, 2012 NSS-MIC, Anaheim, California

PROFESSIONAL MEMBERSHIP

Institute of Electrical and Electronics Engineers (IEEE) member 2010 - 2013

JOURNAL PUBLICATIONS

Paul Dasari, Karen Johnson, Clifford Lindsay, Joyoni Dey, Joyeeta Mitra Mukherjee, Member, Shaokuan Zheng, and Michael A. King. MRI Investigation of the Linkage between Respiratory Motion of the Heart and Markers on Patient's Abdomen and Chest: Implications for Respiratory Amplitude Binning List-Mode PET and SPECT Studies. *Transactions on Nuclear Science,* 61, 192-201, 2014

Paul Dasari, Arda Konik, Mohammed S. Shazeeb, Clifford Lindsay , Joyeeta M. Mukherjee , Karen L. Johnson and Michael A. King.. Adaptation of the Bouc-Wen Model to Compensate for Hysteresis in Respiratory Motion for the List-mode Binning of Cardiac SPECT and PET Acquisitions: Testing using MRI. *Medical Physics* (*In Review*)

Michael A. King, Joyoni Dey, Karen Johnson, **Paul Dasari**, Joyeeta M. Mukherjee, Joseph E. McNamara, P. Hendrik Pretorius, Arda Konik, Cliff Lindsay, Shaokuan Zheng, and Dennis Coughlin. Use of MRI to Assess the Prediction of Heart Motion in Myocardial Perfusion Imaging by Stereo-Tracking of Markers on the Body Surface. *Medical Physics*, 40, 112504, 2013

CONFERENCE PROCEEDINGS

King MA, Dey J, Johnson K, **Dasari P**, Mukherjee JM, McNamara J, Pretorius PH, Konik A, Zheng S, Miro S. Use of MRI to Assess the Prediction of Heart Motion by Stereo-Tracking of Markers on the Body Surface. Proceedings of 2010 IEEE Medical Imaging Conference, M18-324, 3320-3325, 2010

Connolly CM, Konik A, **Dasari P.K.R**, Segars P, Zheng S, Johnson KL, Dey J, King MA. Creation of 3D Digital Anthropomorphic Phantoms which Model Actual Patient Non-rigid Body Motion as Determined from MRI and Position Tracking Studies of Volunteers. Proceedings of SPIE Conference 7964, pp79642G1-8, 2011

Dasari P, Johnson K, Dey J, Mukherjee JM, Zheng S, Connolly C, King MA. MRI Investigation of the Linkage between Respiratory Motion of the Heart and Markers on Patient's Abdomen and Chest: Implications for Respiratory Amplitude Binning List-Mode PET and SPECT Studies. Proceedings of 2011 IEEE Medical Imaging Conference, MIC18-106, 2011

Konik A, Connolly CM, Johnson KL, **Dasari P**, Segars WP, Pretorius PH, King MA. Digital Anthropomorphic Phantoms of Non-Rigid Human Respiratory and Voluntary Body Motions: A Tool-Set for Investigating Motion Correction in 3D Reconstruction. Proceedings of 2011 IEEE Medical Imaging Conference, MIC17-2, 2011

Lindsay C, Gennert MA, Connolly CM, Konik A, **Dasari PK**, Segars WP, King MA. Interactive Generation of Digital Anthropomorphic Phantoms from XCAT Shape Priors. Proceedings of SPIE Conference 8317-21, pp 83170M1-M10, 2012

Dasari P, Konik A, Shazeeb MS, King MA. Accounting for the hysteresis of respiratory motion of the heart in cardiac SPECT and PET using the Bouc-Wen model of hysteresis. Proceedings of 2012 IEEE Medical Imaging Conference, MIC15-53, pp 3030-3032, 2012

Dasari P, Johnson KL, Lindsay C, King MA. The effect of arm position on respiratory motion of the heart: implications for emission imaging. Proceedings of 2012 IEEE Medical Imaging Conference, MIC15-54, pp 3033-3035, 2012

Konik A, **Dasari P**, Mukherjee JM, Johnson KL, Helfenbein E, Chien S, Babaeizadeh A, Shao L, Dey J, King MA. Respiratory tracking using EDR for list-mode binning in cardiac emission tomography: comparison with MRI heart motion measurements. Proceedings of 2012 IEEE Medical Imaging Conference, MIC03-4, pp 2131-2136, 2012.

Eric Helfenbein, Cheng-hao Simon Chien, Saeed Babaeizadeh, **Paul Dasari**, Arda Könik, Joyeeta Mitra Mukherjee, Michael King, Lingxiong Shao. ECG/EMG-Derived Respiration During Cardiac Magnetic Resonance Imaging. *ISCE* 2012

Cheng-hao Simon Chien, Eric Helfenbein, Saeed Babaeizadeh, **Paul Dasari**, Arda Könik, Joyeeta Mitra Mukherjee, Michael King, Lingxiong Shao. A Comparison of Three ECG-Derived Respiration Techniques During Cardiac Magnetic Resonance Image Acquisition. *ISCE* 2012

Dasari P, Konik A, Pretorius PH, Shazeeb MS, Segars WP, Johnson K, King MA. Evaluation of Bouc-Wen model corrected respiratory motion in cardiac SPECT. Proceedings of the 12th International Meeting on Fully Three-Dimensional Image Reconstruction in Radiology and Nuclear Medicine, pp 396-399, 2013

Paul Dasari, P. Hendrik Pretorius, Arda Konik, Mohammed S. Shazeeb and Michael A. King. Correction of Hysteretic Respiratory Motion in SPECT Myocardial Perfusion Imaging. *SNM* 2013

Lindsay C, Gennert MA, Konik A, **Dasari PK**, King MA. Automatic generation of digital anthropomorphic phantoms from simulated MRI acquisitions. Proceedings of SPIE Conference 8671-74, pp 8671221-8, 2013

Rhodri L. Smith, Kevin Wells, John Jones, **Paul Dasari**, Cliff Lindsay, Michael A. king. Toward a Framework for High Resolution Parametric Respiratory Motion Modeling. *IEEE-MIC* 2013